EXPLOITATION OF P-GLYCOPROTEIN AT THE BLOOD BRAIN BARRIER FOR TARGETED DRUG DELIVERY

A Dissertation

Presented to the Faculty of the Graduate School

of Cornell University

in Partial Fulfillment of the Requirements for the Degree of

Doctor of Philosophy

By

Lindsey Anne Crawford

August 2015

EXPLOITATION OF P-GLYCOPROTEIN AT THE BLOOD BRAIN BARRIER FOR TARGETED DRUG DELIVERY

Lindsey Anne Crawford, Ph.D.

Cornell University, 2015

Drug development for the central nervous system (CNS) has struggled to reach clinical approval. One reason many drugs do not advance into clinical applications is their low uptake in the CNS due to the blood brain barrier (BBB). Targeted drug delivery to the CNS has been well-studied for over 30 years, and recently has been focused on methods of BBB disruption (e.g., focused ultrasound), circumvention (e.g., convection enhanced delivery) or exploitation (e.g., receptor mediated targeting). Receptor mediated targeting is a method of active transport across the BBB by exploiting endogenous receptor-ligand interactions. The work outlined in this dissertation has studied a novel drug delivery method for receptor mediated targeting through the exploitation of P-glycoprotein (P-gp). P-gp is naturally overexpressed at the BBB and therefore makes an attractive target for CNS drug delivery. It was hypothesized that this new approach to CNS delivery could be accomplished by creating a polymeric nanoparticle delivery system with a P-gp substrate as a targeting moiety.

The work focused on the development of a polylactide (PLA) nanoparticle containing a surface-tethered polyethylene glycol (PEG) linker terminated with rhodamine as a P-gp targeting moiety. Rhodamine dyes are a well-known class of P-gp substrates and the two used in this study, rhodamine 6G (Rho6G) and rhodamine 123 (Rho123) show high and moderate affinity to P-gp, respectively. Due to the novelty of this system, the PEG-Rho linker was first assessed *in vitro* to determine if it was still capable of interacting with P-gp as a substrate. It was evident that the conjugates of PEG-Rho still remained P-gp substrates; therefore, the PLA-PEG nanoparticle was developed to assess targeting of the drug delivery system *in vivo*. Before targeting efficiency could be measured *in vivo* a nanoparticle detection method was needed. The autofluorescence of various tissues poses a problem when considering nanoparticle detection by fluorescence *in vivo*. Therefore, the time resolved fluorescent properties of europium

chelates were utilized to overcome autofluorescence challenges. Europium chelates continue to emit photons microseconds after excitation, whereas the autofluorescent molecules in tissues emit photons for only nanoseconds. By measuring photon emittance at microsecond timescales following excitation, the autofluorescent background was eliminated allowing sensitive detection of the nanoparticles *in vivo*. Once the Rho-PEG-PLA nanoparticle was synthesized and a detection method to track and quantify the particles *in vivo* was developed, the targeting efficiency of the systems was assessed. In a mouse model, Rho6G-PEG-PLA nanoparticles accumulated 2.6 times greater in the brain than untargeted control mPEG-PLA nanoparticles. Using a P-gp knockout mouse, the accumulation of Rho6G-PEG-PLA nanoparticles was shown to significantly decrease in the brain compared to the wild type mouse. Thus the conclusion was made that Rho6G-PEG-PLA nanoparticles can actively target P-gp at the BBB and can enhance the accumulation of drug delivery nanoparticles in the CNS.

BIOGRAPHICAL SKETCH

Lindsey A. Crawford was born on May 15, 1988 in Saint Albans, VT to parents, David and Cheryl Duplissa. From the age of four she was extremely interested in medicine, often posing as Dr. Quinn (medicine woman) with her cowgirl hat, rocking horse, and medical bag. In her sophomore year of High School she took chemistry and found a love that rivaled her interest in medicine. Since she excelled at both math and chemistry, her AP chemistry teacher suggested she look into Chemical Engineering as a college major. Lindsey decided it would be the perfect fit and attended Clarkson University in the fall of 2006 to pursue a degree in Chemical Engineering. While at Clarkson, she was introduced to scientific research by her advisor Dr. Ruth Baltus. Working for Dr. Baltus as an REU student for the summer, Lindsey fell in love with research. Wanting to step outside her comfort zone by experiencing research at an institute outside of Clarkson, she participated in a second REU at Duke University the following year under Dr. Claudia Gunsch. As vice president of Clarkson's Omega Chi Epsilon chapter, Lindsey was responsible for hosting a professor from Cornell University, Dr. David Putnam, who was giving a seminar to the group. During his visit, Lindsey learned about the opportunities at Cornell University for graduate school and in August of 2010 started toward her doctorate at Cornell.

Lindsey was happy with Chemical Engineering, however, she still had a passion for medicine. In the Putnam lab, Lindsey was able to combine all of her research interests by working on the development of novel drug delivery strategies. In the second summer of her PhD, Lindsey married her high school sweetheart, Matthew. They had to live apart while she finished her degree, but after completing her degree she will finally be living with her husband (and their adorable dog, Duncan) in St. Louis, MO. In St. Louis she will be a postdoctoral research associate at Washington University in Biomedical Engineering. While she is extremely excited for this next chapter in her life, Lindsey will dearly miss working with the Putnam lab members.

To my husband, Matthew

AKNOWLEDGEMENTS

I would like to first thank my advisor, Dr. David Putnam, for all of his support and guidance during my years at Cornell. Had I never met him 5 years ago when I was a senior at Clarkson University my career path may have looked very different than today. He always stayed positive about our overall research goal, even when presented with negative results. It was his positivity that gave me the perseverance and focus necessary to accomplish the goals we set for my PhD thesis work. Through his mentorship, I have also developed the ability to independently delve into complex research problems. This will be an invaluable skill for the remainder of my career in research. I also want to thank my committee members, Dr. Michael King and Dr. Claudia Fischbach-Teschl for their guidance and support throughout this process. I would also like to thank the National Science Foundation for providing me funding throughout my PhD.

I also want to give a big shout out to the Putnam lab. I have never belonged to such a special group of individuals as this group. We have had an exceptional group throughout my PhD and I could not have made it through the hills and valleys of research without all the laughter. I hope future years in the Putnam lab have as much joy working together as we have. Among the Putnam lab members, I want to give a particular thanks to my undergraduate students, Megan Musacchio, Jaclyn Higgins, and Jessica Zou. Thank you, not only for the hard work you put into each experiment, but for continually keeping me on my toes. Every question you asked me helped me think deeper about our research and I am in debt to you for your support during my PhD.

Support from friends and family has also been extremely important during the PhD process. Justin and Rambert, thank you for all of the support during the last few years. Sunday football and dinners were a time to unwind and clear our minds. They say laughter is the best medicine! I need to give a big thanks to my parents, Cheryl and David Duplissa. You have always believed in everything I have done and I will be forever grateful for the support you continue to give me. Thank you for always listening to my presentations through Skype. I would never want to practice first with anyone else. I

would also like to thank my other family members and friends for supporting me throughout this work, especially grandma Olive for “walking” with me around campus.

I need to give a special thanks to Duncan (the dog). He has sat by my side through every typed word and figure made. He provided me with emotional support on rough days and playful breaks when I needed them the most. Lastly, but certainly not least, I want to thank my husband, Matthew Crawford, for always being there for me and providing unending encouragement. Without his love I would be lost. Even miles apart he managed to stock my freezer with premade meals, proof-read all of my papers, and listen to my never ending research stories.

TABLE OF CONTENTS

*- publication

**- future publication

CHAPTER 1

INTRODUCTION

The population diagnosed with neurodegenerative diseases and aggressive brain cancers is continually growing. According to the 2013 CDC report, Mortality Multiple Cause Micro-data Files, Alzheimer's disease and stroke are among the top 10 leading causes of death in the United States [1]. The American Cancer Society reports brain cancer having only a 35% five-year survival rate[2]. As of June 2009 only 8.2% of drugs developed for activity in the central nervous system (CNS) have been approved for clinical use, making it the lowest percentage of all therapeutic classes. However, therapies for CNS diseases are among the top targets for drug development [3]. The challenge in the translation from drug development to clinical success has been greatly dampened by delivery challenges to the CNS, largely due to the blood brain barrier (BBB) [4].

The BBB serves a natural protective function to prevent the entry of toxic substances to the CNS. Tight cellular junctions strictly limit diffusion of polar molecules from the blood through the capillary endothelial cells. Passive transport through the BBB occurs for lipid soluble molecules that are less than 400 kDa in molecular weight. However, although lipophilic molecules may passively diffuse through the BBB, they can quickly be expelled by endogenous membrane transport proteins expressed by the BBB endothelial cells, most notably P-glycoprotein (P-gp), Multidrug Resistance-associated proteins (MRP) and Breast Cancer Resistant Protein (BCRP). Of the macromolecules that are capable of transporting across the BBB, most pass through via receptor mediated endocytosis or adsorptive mediated endocytosis; however, these routes are limited to specific molecules [5]. Due to these restrictions, there has been considerable research over the past 20 years to develop drug delivery systems capable of surmounting this recalcitrant barrier. Although a number of successful strategies have been brought to bear, there still exists a need for more precise and efficient drug delivery to the CNS. This review focuses on the most recent efforts made in the field of targeted drug delivery to the CNS. Strategies include methods to disrupt the BBB (e.g., focused ultrasound), circumvent the BBB (e.g., nanoparticle delivery or

direct injection methods), or to exploit endogenous receptors/interactions between certain molecules and the BBB (e.g., receptor mediated transport and cell-penetrating peptide strategies).

1.1 Circumvention

Ways to circumvent the BBB have been proposed as one strategy to enhance drug delivery to the CNS. Various delivery routes and carriers are used to bypass this restrictive barrier and increase the concentration of therapeutics in the brain. Circumvention methods reported here are nanoparticle systems, convection enhanced delivery (CED) methods and intranasal delivery.

1.1.1 Nanoparticles. Nanoparticles have been used in drug delivery applications for decades. They are favored for targeted drug delivery due to their large surface area, enhanced circulation times and reduction of systemic side effects[6]. In the field of CNS targeted drug delivery, nanoparticles have become increasingly important. Not only do they increase circulation and reduce systemic uptake of therapeutics, but they also evade efflux from transport proteins located at the BBB, such as P-glycoprotein[7]. Recent work has focused on the use of nanoparticles for efficient and effective drug delivery across the BBB. Surface modifications have been explored to further enhance the effects.

Lipid based nanoparticles have attracted attention as drug carriers for a range of applications due to their biocompatibility and efficient packaging of drugs [8]. In recent years there have been a number of successful examples using both liposomes and solid lipid nanoparticles. Where liposomes are a lipid bilayer with a hydrophilic core that exhibit burst release, solid lipid nanoparticles are densely packed lipids capable of encapsulating hydrophobic drugs with high efficiency [8]. Liposomes have been shown to significantly improve CNS drug delivery for the treatment of glioblastoma with liposomal formulations of irinotecan (Irinophore C™), doxorubicin (Caelyx®) and vincristine, which are all known P-gp stubstrates, demonstrating the ability of liposomal formulations to overcome BBB efflux [9]. Liposomes transporting FK506 increased neuroprotective effects in an ischemia-reperfusion injury model while decreasing

systemic effects [10]. Neuroprotection was also seen in liposomes carrying Asialo-erythropoietin [11]. Solid lipid nanoparticles have effectively transported clonazepam, delaying seizure response from 1.5 minutes (free drug) to 13.5 minutes [12]. They have also shown effective memory retention via quercetin delivery [13].

Like lipid based carriers, chitosan nanoparticles were originally inspired by nature. As a natural polysaccharide with antifungal and antibiotic properties, chitosan-based nanoparticles have aided in CNS targeted drug delivery [14]. One of the attractive applications of chitosan nanoparticles for CNS drug delivery is the oral administration of neuropeptides. Unencapsulated, orally delivered peptides would quickly degrade in the GI tract, however due to protection and adhesive properties of the chitosan nanoparticle, significant adsorption at the intestine walls and uptake in the brain is possible [15,16]. Chitosan nanoparticles encapsulating siRNA for P-gp knockdown have also shown success at delivering doxorubicin *in vitro* [17].

Beside the effect of the nanoparticle core, surface modifications are important to further enhance CNS drug delivery. In recent years, polysorbate 80 has been widely studied for its effects on nanoparticle uptake in the CNS. Its enhancement to CNS drug delivery systems has been attributed to attractive forces between polysorbate 80 and apolipoprotein, which actively targets the BBB, [18] and polysorbate 80's ability to inhibit P-gp [19]. Polysorbate 80-modified particles have more efficiently and effectively improved the treatment of depression using chitosan nanoparticles [20], slowed tumor progression using poly(methacrylic acid) nanoparticles [21], and increased the brain concentration of PLGA-PEG nanoparticles [22]. Polysorbate 80 in conjunction with poly(butyl cyanoacrylate) (PBCA) has become a popular combination in CNS drug delivery as it is relatively safe[23] and has shown increased brain uptake [24], enhanced transport of large molecules to brain injury site [25] and neuroprotection in an ischemic injury model [26]. Further improvements have been made by using polysorbate 80 in conjunction with poloxamer 188 to coat chitosan [27], PLGA [28], and PLGA-PEG-PLGA[29] nanoparticles. It is thought that, like polysorbate 80, poloxamer 188 also attracts apolipoproteins, but also has the added benefit of attracting transferrin, another BBB targeting molecule, [30]. The combination of polysorbate 80 and poloxamer 188 is an example of multiple targeting to the BBB. Additional surface modifications that have been explored to

increase CNS uptake include varying the particle charge. Cationized BSA-PEG-PLA nanoparticles and cationic trimethylated chitosan nanoparticles have shown improved efficacy, due to adsorptive mediated endocytosis from the cationic nature of the particles [31]. Although surface modification is a promising approach for targeted drug delivery to the brain, concerns remain about the systemic safety of the various particle systems, particularly in the epithelial lining of the lungs [32]. Therefore, uptake in the lung and other vital organs should be considered when designing surface modified nanoparticle systems.

Like nanoparticles, dendrimers have received considerable attention for CNS drug delivery. They possess multiple locations for drug and ligand conjugation, are uniform in size, are on the nanoscale, and have a globular shape that helps them to mimic biological macromolecules [33,34]. Two commonly used dendrimers in CNS drug delivery include polyamidoamine (PAMAM) and carbosilane. Due to their cationic nature, they are able to cross membranes[35] and can efficiently complex and transfer siRNA [36,37]. Carbosilane dendrimers carrying siRNA-NEF not only showed efficient delivery to the brain, but were able to transfect HIV infected astrocytes [37]. However, over population of dendimers with amino functional groups can increase toxicity[34]; therefore, a balance between transfection efficiency and toxicity should be considered.

Other particle types that have drawn recent attention for drug delivery to the CNS include magnetic nanoparticles [38–40], poly(trimethylene carbonate) nanoparticles (PTMC) [41] and gold nanoparticles [42]. In addition to drug delivery, magnetic nanoparticles can be used in imaging and magnetic targeting applications [43]. PTMC is a biodegradable polycarbonate-ester, and like PLA, can be manipulated to tune degradation kinetics by altering the copolymer composition[44,45]. Gold nanoparticles are also an attractive delivery platform as they are monodisperse and have tunable properties to change biodistribution and payload [46].

Many of the nanoparticles and dendrimers discussed in this section (and some not yet mentioned) are discussed throughout the remainder of this review as they pertain to many aspects of CNS targeted drug delivery. Table 1.1 provides a summary of the nanoparticle formulations used in conjunction with other techniques discussed throughout this work. In particular, while not discussed in detail in this

section, traditional biodegradable polymeric nanoparticles of PLA and PLGA, play a large role throughout the remainder of this review.

1.1.2 Convection enhanced delivery. Convection Enhanced Delivery (CED) circumvents the BBB by continually infusing drug intraparenchymally. It makes use of basic transport properties; convection will enhance diffusion [47], and differs from passive diffusion in that the transport distances are significantly enhanced. Perhaps the most successful example thus far of exploiting passive diffusion for local therapy in the CNS is the Gliadel® system. Gliadel® wafers contain BCNU that diffuses from the wafer as it degrades and slowly penetrates the surrounding tissue. The penetration depth is governed by the concentration gradient created by the Gliadel® drug reservoir. It is implanted following tumor resection with the goal to destroy remaining tumor cells surrounding the resection cavity. While a Gliadel® is clinically useful [48,49], further enhancement of therapy by CED could allow even further penetration of drug molecules into surrounding tissue. Thus, using the principles of convection and diffusion, CED looks to further enhance the accessibility of drugs to more remote regions of the brain.

Although CED for unencapsulated drug molecules is still being studied[50–54], there has been a shift in the field toward understanding and utilizing nanoparticles in combination with this technology. It was initially thought that particles above 64 nm could not diffuse within brain tissue [55], however densely PEG coated particles up to 114 nm were shown to efficiently diffuse throughout the brain [56]. The PEG coating enhanced the brain distribution by limiting specific interactions with tissues and receptors, a phenomenon that has also been seen with maghemite particles coated with human serum albumin [57]. In recent literature, treatment of gliomas by CED of unmodified PLGA nanoparticles has proved ineffective [58,59]; however, PEG modified[59] or trehalose modified [60] PLGA nanoparticles have shown efficacy. Efficacy to treat gliomas has also seen limited success with lipid based particles in recent years [61,62]. Together these studies provide evidence that carrier type and surface coating may play a role in efficient and effective delivery with CED

Table 1.1. Nanoparticle delivery systems used in drug delivery to the CNS

particle core	functionalization	targeting/active agent	use	reference
PLGA	PEG	N/A	CED	56,59
			FUS	151
		CPP	IN	118
		Glutathione	RM-peptide	217
		Lactoferrin	RM-other	234
	TPGS	N/A	IN	105
	Trehalose	N/A	CED	60
	N/A	N/A	CED	58
		Glycopeptide	RM-peptide	213–215
Polystyrene	PEG	N/A	CED	56
			FUS	151
		Fn14 antibody	RM-other	225
	N/A	gH625	CPP	244
PCL	PEG	CPP	IN	108
		Transferrin	RM-transferrin	180
		angiopep-2	RM-peptide	205,207
		Lactoferrin	RM-other	233
	N/A	N/A	CED	58
PLA-PCL	PEG		CED	67
Liposome	PEG	N/A	CED	54,62
		CPP	IN	109
		RM-peptide	FUS	152
		transferrin antibody	RM-transferrin	184–186
		Transferrin	RM-transferrin	174
		ApoE peptide	RM-peptide	201,202
		Glutathione	RM-peptide	220,221
		T7 and TAT	CPP	239
	N/A	N/A	CED	68,80
		Glucoside	RM-other	229
Other lipid based carriers	PEG	Transferrin	RM-transferrin	175,181
		5-HT-moduline	RM-peptide	219
	N/A	N/A	CED	61
		N/A	IN	103
		Borneol	CD	133
iron oxide	chitosan-PEG	N/A	CED	65
		CD20 antibody	RM-other	222
	N/A	N/A	FUS	167
		PECAM-1 antibody	RM-other	224

Table 1.1continued. Nanoparticle delivery systems used in drug delivery to the CNS

particle core	functionalization	targeting/active agent	use	reference
PLA-PCL	Chitosan	N/A	IN	112
	PEG	CPP	IN	117,118
		transferrin antibody	RM-transferrin	187
		Peptide	RM-peptide	196
		TGN and QSH	RM-peptide	197,198
		LDLR mediated peptide	RM-peptide	211
		Penetratin	CPP	242
		MT1-AF7p	CPP	241
	TPGS	Transferrin	RM-transferrin	179
Gold Nanoparticles	PEG	N/A	FUS	149,150
		TAT	CPP	240
	N/A	transferrin peptide	RM-transferrin	192
PE	PEG	angiopep-2	RM-peptide	204,206
PAMAM dendrimer		angiopep-2	RM-peptide	208
PAMAM-carbomethyl chitosan Dendrimer	N/A	CD11b antibody	RM-other	223
Albumin	N/A	Glutathione	RM-peptide	218
gelatin-siloxane	PEG	TAT	CPP	238
		SynB	CPP	243
magnetic PLGA /solid lipid NP	PEG	TAT	CPP	236
Chitosan	PEG	TAT	CPP	237
CPEGGM-PDSGM	N/A	des-octanoyl ghrelin	RM-other	232
PBCA	N/A	CRM197	RM-other	227

Abbreviations: PLGA (polylactide-co-glycolic acid), PEG (polyethylene glycol), TPGS (d-- tocopheryl polyethylene glycol 1000 succinate), PCL (polycaprolactone), PLA (polylactide), PE(1, 2-Distearoyl-sn-glycero-3-phosphoethanolamine), PAMAM (poly amido amine), CPEGGM-PDSGM (poly(carboxyl ethylene glycol-g-glutamate)-co-poly(distearin-g-glutamate), PBCA (polybutylcyanoacrylate), CED (convection enhanced delivery), FUS (focused ultrasound), IN (intranasal), RM (receptor mediated), CPP (cell penetrating peptide)

In an effort to better treat gliomas implanted in a rodent model with CED, there have been a number of studies using a combination of CED and either systemic chemotherapy or radiation. These strategies have seen a range of efficacies from no enhancement [50] to significant improvements upon co-delivery [52,63,64]. In some cases the combinations also improve safety compared to systemic chemotherapeutic administration alone [65]. Among the significant improvements, one was attributed to BBB opening by the CED infused chemotherapeutic (nimustine), which allowed greater penetration of the systemically administered liposomal doxorubicin [54]. Inconsistencies in efficacy could be attributed to specific carrier type or particular chemotherapy regimen used, but there have also been suggestions that there can be significant variability among animals with CED [66]. Part of this variability can be attributed to the non-uniform penetration geometries that are experienced upon CED administration [67]. Therefore, to further enhance treatment of gliomas with CED optimization with respect to penetration patterns should be considered.

Although the majority of CED *in vivo* models have focused on glioma, there are others worthy of discussion. Gene delivery with CED has been explored and has proven efficient [68,69] and moderately effective at delivering siHtt as a treatment for Huntington's disease; however, knockdown was mostly present at the injection site [70]. CED of BDNF was used in a spinal cord injury model and while there were significant restorative effects, in this study there was no comparison to systemically administered BDNF [71]. CED has also been used to treat brain stem tumors [72,73] and in a methamphetamine addiction model [74], showing improvements over controls in all cases.

Optimization thus far has been focused on understanding the distribution of macromolecules within the CNS using CED. Co-administration of either Gd-albumin or Gd-DTPA with Evans blue dye revealed site-specific distribution at the hippocampus [75,76], which was attributed to neuroanatomical structures that provided less fluid resistance[76]. The ability of Gd-DTPA to be used as a model macromolecule for imaging is possible, but may require calculations for standardization [77]. Alternatively, Gd-DTPA has been directly conjugated to various molecular weights of polylysine showing and inversely proportional relationship between distribution volume and molecular weight; however, there was also

tissue damage associated with this method [78]. Gd-DTPA has also been used to determine properties associated with CED in an ischemic stroke model [79].

In the last five years, of the areas of research mentioned in this review, CED has shown the most translation from small animal models to clinical trials. The transition into non-human primates has mainly focused around safety and feasibility of CED systems in more sophisticated models. Nanoparticle delivery via CED was feasible [80] and infusion of ACNU was found to be generally safe [81]. To enhance the effects of gene delivery for Parkinson's disease seen in Phase I clinical trials, a non-human primate MRI guided CED system was tested and provided a more predictable distribution [82]. There have been a number of Phase I, II and III clinical trials reported in the last few years, all for treatment of glioma. The description of a future Phase I clinical trial for carboplatin seems promising as carboplatin has been successful in animal models [83]. A CED Phase Ib study for topotecan showed a 6 month progression-free survival and 6 month overall survival of 44% and 75%, respectively, without evidence of systemic toxicity [84]. Topotecan was also used in a CED trial of 2 pediatric patients with brain stem tumors, and although it was unable to prolong survival, the study proved feasibility of using CED in children and for brain stem tumors [85]. A Phase IIb trial to treat high grade glioma with CED of trabedersen, saw no significant improvements at the 6 month endpoint; however, the low dose group showed promising results versus standard chemotherapy with less adverse effects [86]. In the well-known Phase III PRECISE trial, the largest trial to treat glioblastoma multiforme after resection, there were no significant improvements compared to Gliadel® wafers which was largely attributed to the specificity of the drug compared to the heterogeneous nature of glioblastomas [87]. In a review of recent CED clinical trials, Shahar et al. cover the drawbacks the catheter placement surgery can have on the success of the trial. They urge for optimization of catheter type and placement for development of a successful trial [88]. Catheter placement and type has been a highly studied attribute of CED and while it is beyond the scope of this review, the literature is replete with examples of current advancements [89–94].

1.1.3 Intranasal administration. Intranasal (IN) drug delivery has become an attractive approach to circumventing the BBB in the last decade. It provides a direct route to the brain and is able to decreases systemic exposure and limit degradation of therapeutics [95]. In recent years IN delivery has been explored for therapeutic proteins, small molecules, nanoparticle systems, and in conjunction with other targeting moieties.

Therapeutic proteins and small molecules can have high rates of degradation in the blood stream and can show limited uptake in the brain due to the BBB [96]. Therefore, IN has been explored to increase their concentration in the brain. While some IN molecule formulations have shown accumulation [97] and efficacy[98] in the brain, there have also been site specific accumulations in the olfactory bulb [99] and no significance in comparison with other administration methods [98,100]. However, faster peak accumulations[100] and response time [98] are reported along with overall different brain distributions using IN [100]. Therefore, in an effort to increase brain concentrations and efficacy, nanoparticle and bioadhesion technologies have been explored in combination with IN delivery.

The controlled release properties of nanoparticles can be beneficial to enhance retention of therapeutics at the nasal mucosa. In recent years most nanoparticle systems for IN delivery have been lipid based, as they can decrease clearance and incorporate into the mucous membrane [101]. Lipid formulations that have been administered IN have shown a 1.8 time greater analgesic effect [102] and enhanced performance in behavior analysis tests in a depression model [103]. Solid lipid microparticles were able to deliver a poorly water soluble drug and significantly increase its concentration in the brain through IN administration [104]. Polymeric nanoparticle systems have also been studied for IN administration. PLGA-TPGS based nanoparticles showed greater nasal retention [105] and polyethylene oxide-polypropylene oxide micelles were 5 times more efficient when administered IN vs. IV [106]. Cell penetrating peptides (discussed in section 4.2) have been used to increase the uptake of drugs in the nasal cavity[107], and when used in conjunction with nanoparticles have shown significant increases in brain uptake compared to IV administration [108] and retention in the hippocampus and cortex [109].

Due to the rapid clearance of molecules in the nasal cavity, retention at the nasal mucosa is limited. Bioadhesives have been proposed as a method of enhancing contact time [110]. In recent years, chitosan and lectin have been the two most widely studied bioadhesives. Chitosan is a biocompatible and biodegradable polysaccharide that, when protonated, adheres to negatively charged surfaces making it an attractive bioadhesive [111]. Chitosan particle formulations have shown enhanced efficiency[112–114] and efficacy[115] in recent years; however, lectin has been more widely studied for IN delivery. Lectin is a family of peptides that selectively bind to glycosylated proteins, such as those lining the nasal mucosa [110]. IN administered lectin conjugated PLA-PEG nanoparticles have increased brain to blood ratios by 2 fold compared to non-lectin particles [116], increased concentration of basic fibroblast growth factor while reducing side effects [117] and showed the best performance in a Parkinson's model [118]. Similarly, lectin PLGA-PEG particles increase brain concentration, initially in the olfactory bulb but in the cerebrum and cerebellum at longer times [119]. However, they failed to increase efficacy in a schizophrenia model (catalepsy test) [120]. These studies all show the benefits lectin can have on IN delivery and provide a nice alternative to chitosan, however more efficacy tests are needed.

1.2 Disruption of the blood brain barrier

To overcome limited drug passage through the tight endothelial cell junctions of the BBB, strategies have been developed to actively permeabilize the BBB to allow unrestricted passage of small molecules, macromolecules and therapeutic viruses. Initial studies on BBB disruption focused on chemical means, but more recently physical forces have been considered. Recent advances in both chemical and physical disruption are discussed.

1.2.1 Chemical disruption. Mannitol is the most widely studied chemical for disrupting the BBB. It hyperosmotically shrinks endothelial cells, providing space for large molecules to passively diffuse across the BBB [121]. In recent years it has been used in conjunction with gene delivery [122,123], nanoparticles [124], peptides[125], cellular delivery [126] and even as a component of a polyplex for siRNA delivery [127]. Mannitol

has also been studied in clinical treatment of recurrent malignant glioma with intra-arterial delivery of both mannitol and bevacizumab [128]. While the previously mentioned studies showed success, there have also been some challenges associated with mannitol delivery. When adapting mannitol usage from a rodent model into rabbits there was wide variation in the extent of BBB disruption amongst different animals [129]. Another potential concerns surrounding mannitol administration involve discrepancies regarding its injection method. Typically mannitol is injected arterially, but in a few of the studies mentioned above [123,127] showed BBB permeation after intravenous injection. Another study suggests that mannitol is ineffective at BBB disruption upon intravenous injection [130]. Therefore, there is a need for fundamental work regarding various injection methods and mannitol's effectiveness.

In the past few years a few other chemicals have shown promise in BBB disruption. Another carbohydrate, polydixylitol, functions similar to mannitol in that it disrupts based on osmotic pressure, but also provides osmotic shock to the cells which enables effective penetration of siRNA polyplex into astrocytes [131]. Borneol, a molecule used in traditional Chinese medicine, has also been explored as a BBB disrupting agent, via opening of tight junctions [132]. Recently, Borneol has been investigated to facilitate liposomal transport across the BBB [133], as well as its effect on the expression of MDR1 and Mrp1 transporters at the BBB while enhancing penetration of rhodamine 123 [134]. Other agents include lyophosphatic acid [135], a signaling molecule, and anti-endothelial barrier agent [136]. While there are still studies involving chemical disruption of the BBB, inconsistencies have shifted the field toward less invasive physical disruption.

1.2.2 Focused ultrasound. One of the emerging fields in CNS drug delivery is Focused Ultrasound (FUS), which presents a non-invasive physical approach to BBB disruption. Disruption of the BBB caused by ultrasound was first discovered in the 1950's [137], however, drug delivery applications involving FUS did not appear until the early 2000's. The current method for FUS combines the power of ultrasound with sonoporation enhancement of microbubbles [138]. Ultrasound is focused at the target site in

the brain and when circulating microbubbles reach the targeted area they enhance the sonoporation of the targeted vessels [139].

The main treatment objective with focused ultrasound has been to deliver molecules that cannot naturally penetrate the BBB. To gain an understanding of the efficiency of FUS systems, a variety of model drugs and therapeutics have been used. Although some small molecules have been studied for efficiency[140,141], the major focus has been on macromolecules. The hydrodynamic diameter of macromolecules is their main limitation for crossing the BBB[5]. Dextran has been used as model macromolecule due to its flexibility in molecular weight and ability for conjugation of fluorescent makers for detection. Dextran has been used in proof of concept studies involving the effects of various FUS parameters on BBB disruption [142], to assess the combined strategies of intranasal (IN) and FUS [143], alongside a PBCA super paramagnetic iron oxide nanoparticle [144] and as a model mAb [145]. Another important class of macromolecules that have been studied are neurotrophic factors, which are important for the treatment of neurodegenerative disease. Brain derived neurotrophic factor (BDNF) showed greater uptake and maintained activity with FUS [146] and glial-derived neurotrophic factor accumulated over 4 times greater in the brain than without FUS [147].

Although FUS with macromolecules has been efficient, the more interesting application of FUS is its enhancement on nanoparticle uptake. As mentioned above, nanoparticles have been a key component to the advancement of targeted drug delivery. Gold nanoparticles can be used as an independent therapy or as a carrier for other drugs [148]. PEG coated gold nanoparticles with FUS have shown a 336% increase in brain uptake [149] and accumulation of both 50 nm and 120 nm particles [150]. Other nanoparticle systems explored with FUS have been PEG-polystyrene[151], PEG-PLGA[151] and peptide conjugated liposomes[152].

The effect of FUS on efficient gene delivery has also been explored with viral vectors [153,154], DNA[155,156] and siRNA[157]. The combination of siRNA and FUS enabled 32% knockdown of Htt, the mutant protein associated with the neurodegeneration of Huntington's disease. This result shows promise for future efficacy models combining FUS and gene delivery.

In recent years, further development of FUS has involved testing for technique efficacy. A major area of FUS efficay has focused on treating brain tumors, particularly glioblastoma. FUS was able to aid drug infiltration into a glioblastoma in an animal model [158] and significantly decreased tumor size and increased survival[159]. A peptide-conjugated liposomal doxorubicin formulation increased median survival time to 15 days with FUS compared to 9 days for control [152]. In a glioma model BCNU was encapsulated into the microbubbles designed to release at the onset of microbubble burst. Incorporation of the drug into the microbubble further enhanced median survival from 29.5 days for drug alone to 32.5 days for microbubble encapsulated drug [160]. Tumor treatment with poly(analine-co-n-(1-one-butyric acid) coated iron oxide nanoparticles encapsulating epirubicin increased median survival by 66% over controls [161]. Beyond glioma, metastatic brain tumors have been treated with repeated IV doses of trastuzumab combined with FUS showing 38% longer survival with 4 out of 10 completely resolved tumors [162].

Preliminary efficiency models and tumor efficacy models provide evidence that FUS can be an effective tool for CNS drug delivery. However, there is still ongoing work to optimize these protocols. Using Definity© microbubbles, 1.1-3.3 μm lipid particles with octafluoropropane gas encapsulated, numerous studies have investigated the effects of various experimental parameters on FUS. Parameters such as sonication duration, microbubble concentration, pulse repetition frequency, pulse length, and influence of standing waves and pressure are all important [142,163–166] for both efficacy and safety. Since the BBB is a naturally protective function, the safety risks of temporarily permeabilization have to be assessed. To assess inflammation that may occur during various sonication parameters, Liu et. al. magnetically labeled macrophages with super paramagnetic iron oxide nanoparticles to track them in real time. They found there were an ideal set of parameters that did not induce an inflammatory response [167]. Safety of repeated FUS bursts in conjunction with repeated doses of liposomal doxorubicin has also been studied [168] as repeated low doses of liposomal doxorubicin has proven more effective [169]. It proved to be a more effective and safer approach than administration of one large dose [168]. Few studies have moved beyond rodent models, but the existing non-human primate models found challenges determining optimal parameters due to the thicker skull, but were able to eventually identify safe and optimal parameters

[170,171]. As a promising technology, a wider range of efficacy studies and extension to larger animal models can make FUS a valuable technique in CNS drug delivery.

1.3 Exploitation

Exploiting endogenous receptors and transport processes at the BBB has proven to be an effective tool for drug delivery of systemically toxic substances, proteins and peptides. The most common strategies leverage receptor-mediated transport, with either small molecules, antibodies or peptides as the ligand, as well as cell penetrating peptides.

1.3.1 Receptor mediated. Receptor mediated endocytosis exploits the natural receptor-ligand interactions that take place at the BBB and utilizes them for active transport of macromolecules that cannot passively diffuse past the BBB. In the past emphasis was placed on systems utilizing transferrin, insulin and low density lipoprotein receptor mediated systems, however new targets are continually explored. Recent advances in transferrin, peptide-receptor interactions, and various other antibody and ligand-receptor targeting systems will be explored here.

1.3.1.1 Transferrin. Transferrin transports iron through the BBB and in 1995 it was discovered that this occurs through a receptor mediated process, wherein there is a specific receptor for transferrin [172]. Since this discovery, its use in targeted drug delivery has been exploited as a means for transporting therapeutics across the BBB [173]. In recent years drug delivery systems conjugated to transferrin have mostly been studied *in vitro* [174–178], however efficiency [179] and efficacy in brain tumor models [180–182] have been explored *in vivo*. Although the mentioned efficacy models showed significant improvement in decreasing tumor volume and survival, endogenous transferrin has been shown to competitively inhibit receptor binding of transferrin conjugated systems *in vivo*; therefore, other forms of transferrin receptor targeting have been explored [183]. Monoclonal antibodies specific to transferrin have proven efficient for

transferrin receptor targeting [183] and recently have been used to evaluate *in vivo* efficiency [184,185] and *in vitro* efficacy studies for future neurodegenerative disease applications [186,187]. Although these immunotargeted systems are effective, there has been evidence of potential safety risks, including hemolytic anemia, associated with transferrin monoclonal antibodies [188,189]. Therefore, a peptide approach to targeting transferrin receptor has been developed by determining peptide sequences from phage display that are capable of binding to the transferrin receptor without competitive inhibition of transferrin [190]. Using these novel peptides, recent studies have created transferrin peptide conjugates with a cell penetrating peptide that enabled efficient transportation of siRNA [191] and a gold nanoparticle containing a β-sheet breaker peptide capable of interacting with $A\beta_{1-42}$ [192]. With the little interference between transferrin and transferrin receptor binding peptides, this approach has promise to be an effective strategy for BBB targeting in the future.

1.3.1.2 Peptides. Peptides have become an emerging strategy for receptor mediated endocytosis, due to their specificity and ability to trigger and undergo endocytosis. The RGD peptide for tumor targeting has been widely studied and serves as an example for peptides-receptor mediated endocytosis [193]. To discover cell and site specific peptides, a unique strategy has emerged; phage display.

Phage display is a method developed to screen for peptide sequences that bind specifically and selectively to a target site. The literature describes the details of phage display extensively[194] but a brief introduction is provided for context. Exogenous peptide sequences are displayed on the surface of a bacteriophage, which is then incubated with cells expressing the receptor of interest. Through a series of wash steps, only the bound phage remains and through an elution process, bound phage is recovered. The recovered phages are replicated in bacteria and this process is repeated 2-3 more times. The final phage particles are isolated and sequenced to obtain the peptide sequence(s) that bind selectively to the target [194]. The phage display technique has been used in recent literature to create novel targeted drug delivery systems. Novel peptides have been developed with phage technique by incubating phage with choroid plexus explants. The three peptides that were chosen from phage display were able to target choroid

plexus epithelium and ependymal [195]. Phage display was also used for *in vivo* screening of a brain targeting peptide by injecting page display library into mice, allowing distribution and recovering targeted sequences from brain homogenate. These peptides were conjugated to nanoparticles and increased the blood/brain accumulation ratio to 1.57 compared to 0.42 for controls [196]. Other systems have made use of peptides that had been previously discovered with phage display to target the BBB and Aβ42 in Alzheimer's models with TGN and QSH [197,198]. Tet-1, which has binding characteristics of tetanus toxin, was previously discovered with phage display and its specific interactions with neuronal cells was confirmed with a Tet-1 coated PLGA nanoparticle system *in vitro* [199].

Using phage display and other techniques, there has also been an effort to design peptide targeted drug delivery systems toward the low density lipoprotein receptor (LDLR) family of proteins. Traditionally the whole molecule of ApoE was used for targeting to LDLR; however, its binding capabilities can be reduced by interference of serum proteins [185] and it may have a potential role in Alzheimer's disease [200]. This has urged the development of targeting methods using peptides specific to LDLR. Peptides have been designed from ApoE, showing increased uptake *in vitro* [201,202] and increased brain uptake with a system capable of gene delivery [203]. Like ApoE and ApoE-derived peptides, Angiopep-2 has also been found to bind to low density lipoprotein receptor related protein (LRP) at the BBB and its binding has been exploited for targeted drug delivery. Not only have angiopep-2 targeted systems shown efficiency in brain uptake [204] and glioma uptake[205] but they have demonstrated efficacy against brain fungal infection with 30% still surviving at the end of the study [206] and in a glioblastoma model with 37 days median survival compared to 30 days for untargeted systems [207]. Although effective, the density of angiopep-2 on the targeted particle can be problematic and increase RES uptake[208] and angiopep-2 has the potential for degradation due to metabolic barriers[209]. To address potential degradation issues, a d-isomer peptide of angiopep-2 was created, shown to be significantly more stable in serum, and produced greater uptake into the brain. However, there was also visually greater uptake in the liver 1h post injection [209], which could lead to negative systemic effects. Due to the initial success of targeting the LDLR family, phage screening was used to develop a peptide that can not only target the

LDLR family, but had less competition with endogenous molecules [210] and capable of targeting treatment to glioma, showing 146% lifespan extension over drug alone [211].

Strategies separate from the LDLR family have also been developed. In an attempt to exploit neurotropic behavior found in nature, Fu et. al. developed a rabies virus glycoprotein-derived peptide that when fused to various therapeutic proteins significantly lowered neurological deficits in a stroke model [212]. Glycopeptides[213–216], glutathione [217,218] and 5-HT [219] have also shown success as peptide ligands for receptor mediated targeting. Although the glutathione system (glutathione conjugated to pegylated liposomal doxorubicin) showed 4.8 time increase in brain to plasma ratio, there was also a 1.3 times higher systemic exposure [220]. However, the glutathione ligand to GLUT receptor targeting system has proven effective in a neuroinflammation model of experimental autoimmune encephalomyelitis where delivery of glutathione conjugated pegylated liposomes encapsulating methylprednisolone showed 100% survival compared to 77.8% for untargeted pegylated liposomes and 16.7% for untreated subjects. [221]

1.3.1.3 Others. Beyond transferrin and peptide strategies, there have been various other receptor mediated targeted strategies in recent years. The success in antibody targeting efficacy with transferrin has translated to the design of other antibody-receptor targeting systems. Recently two systems were tested *in vitro* for cell specific uptake with CD-20 antibodies (for PCNSL cells) [222] and CD11b (for microglial cells) [223], which showed 4 times greater accumulation compared to controls and cell specific uptake, respectively. *In vivo,* antibody receptor mediated endocytosis was tested using Anti-PECAM-1, and although it gave a 2 fold increase in the brain it also produced at 4 fold increase in the lungs which could have negative side effects [224]. In attempts to overcome some toxicity and specificity challenges of antibody receptor mediated approaches, intracranial injections of an antibody against fibroblast growth factor inducible 14 (Fn14) have been studied [225] along with a novel approach to create monovalent and bivalent fusions of antibody FC5 with human Fc domain for neuroactive peptide delivery [226]. The antibody FC5 was engineered to eliminate its toxic effects while still remaining effective. In a

Hargreaves model of inflammatory pain it had a significant effect on analgesic properties; however, the systemic toxicity was not discussed in this study [226].

Due to the large number of processes that take place at the BBB there are a wide variety of molecules that have been assessed for receptor mediated targeting. In an *in vitro* study a ligand active to diphtheria toxin receptor showed increased permeability [227]. Efficient delivery was seen for targeted systems toward axon transport facilitator [228] and GLUT transporter [229,230]. However, there is potential for systemic effects with the GLUT systems, as GLUT receptor is located in various organs throughout the body [231]. Other studies showed enhanced efficacy using des-octanoyl ghrelin, a functional hormone, as a targeting moiety in an analgesic model [232] and lactoferrin to target the low density lipoprotein receptor in a glioma model [233] and a Parkinson's disease model [234]. Although effective, they all experienced changes in biodistribution of all organs (not just brain) when the targeting moiety was conjugated, which could have potential negative effects. Hu et. al. investigated the inflammation their targeted system had on spleen, kidney and liver and found there was an increase in inflammation after 24 but it disappeared within 48 hours [234]. These consequences of conjugation should be investigated for all systems to rule out potential side effects.

Many of the receptor mediated strategies reviewed here have shown promising efficiency and efficacy both *in vitro* and *in vivo*. One remaining challenge is the potential systemic effects these targeted systems could have. Often, the receptors studied are expressed elsewhere, leading to active targeting to non-target tissues. More studies involving multi-targeted systems could eliminate some of the increases in undesired organs and further enhance efficacy.

1.3.2 Cell penetrating peptides. As a complement to receptor mediated approaches, cell penetrating peptides (CPP's) have provided another means of exploiting endogenous processes at the BBB to enhance drug delivery. CPP's possess the ability to penetrate the BBB through mechanisms that are not yet fully realized [193]. One of the most widely studied CPPs, TAT, was derived from the HIV-1 tat protein. It has served as the model CPP for mechanistic studies of cellular entry and the potential for CPPs to carry

various cargo across the BBB [235]. In recent literature, TAT has been used for both *in vitro* and *in vivo* interactions with a range of success. While TAT enabled nanoparticle delivery *in vitro*[236,237], it was not significantly better at transfecting siRNA than untargeted particles [237]. TAT modified nanoparticles showed greater accumulation in the brain[238] and in a glioma model [239,240] with increased survival[240]; however, modification with a second peptide to target the glioma greatly enhanced tumor uptake [239]. The greater increase upon dual peptide conjugation suggests future work should focus on dual targeted systems. Also in these studies, the accumulation in the liver and spleen was decreased upon TAT conjugation in one instance [238], but increased in another [239]. Cell morphology studies were conducted and showed no significant differences between the nanoparticle treated livers and spleens compared to saline controls [239]. The variation in biodistribution changes between studies is most likely a factor of the nanoparticle composition, solidifying the importance of studying the accumulation in all major organs with each novel drug delivery system.

Although TAT has been the most widely studied CPP in recent years, others have also shown promise in CNS drug delivery. In a combination therapy strategy, a glioma targeted bind peptide (MT1-AF7p) was conjugated to a nanoparticle system and co-administered with a tumor penetrating peptide (iRGD). The combination therapy enhanced median survival from 12 days without iRGD to 39 days with its co-administration [241]. Penetratin increased brain accumulation by 1.89 times while having no change on the systemic biodistribution [242] while a SynB nanoparticle system showed an increase in brain accumulation with a decrease in the liver [243]. These alternative strategies are promising and could provide even greater enhancements when used in combination with receptor mediated peptides.

1.4 Future recommendations. Targeted drug delivery has seen important improvements in recent years; however, there still exist a need for more site specific delivery. This can be accomplished by finding new receptor mediated targets or combining various strategies reviewed above to enhance the targeting specifically to the CNS. There is also a need for more advanced and diverse efficacy models. The

majority of efficacy models focus on gliomas in rodents, however, there are many other CNS diseases that could be investigated.

1.5 P-glycoprotein

P-glycoprotein is a 170 kDa transport protein expressed among species of mammals, most notably in humans and rodents. The natural function of P-gp is to protect the body from toxic substances by actively transporting drugs at tissue-fluid barriers. During the oral route of administration of drugs, P-gp plays a role in transport of its substrates in and out of the intestines, liver and kidneys. P-gp is responsible for expelling its substrates from intestinal tissue back into the gastrointestinal lumen. During excretion of P-gp substrates in the kidney and liver, P-gp prevents re-adsorption by maintaining its substrates in the proximal tubule lumen and bile, respectively. P-gp is also located at the blood-brain barrier, blood-testis barrier and blood-placenta barrier. In these tissues, substrates are kept in the blood lumen and prevented from adsorption into the endothelial cells.[245,246] Although the natural function of P-gp is protective, it can also create major challenges in drug delivery of important therapeutic substances. Therefore, many studies have focused on identifying P-gp substrates and inhibitors.

Substrates of P-glycoprotein were first studied in the 1970's but the majority were discovered between the 1980's to present. To date the various classification of substrates have included dyes, chemotherapeutics, antibiotics, and steroids among many other hydrophobic and cationic molecules.[247] The process through which P-gp interacts with substrates was best described by Aller et al. in their study involving the x-ray structure of P-gp which revealed its polyspecific binding pockets. They were able to show that once a P-gp substrate enters into the inner leaflet of the cell membrane it is recognized by the protein and transported to one of two binding pockets through an inner membrane pore. Once the substrate is bound, ATP binds at the intracellular nucleotide binding domains of P-gp which causes a conformational change. The conformational change leads to expulsion of the substrate by P-gp.[248]

Understanding P-gp structure and function has been important when considering methods of drug delivery of P-gp substrates. Often, attempts to overcome the challenges associated with delivering P-gp

substrates has been focused on inhibition of P-gp function. First generation inhibitors, such as verapamil, showed promising inhibition *in vitro* but carried negative side effects when co-administered with P-gp substrates *in vivo*.[249] Attempts have continually been made to discover new inhibitors and have led to a promising class of inhibitors, pluronics.

Pluronics are block copolymers composed of ethylene oxide-propylene oxide-ethylene oxide and they vary in molecular weight of the different blocks. Their ampiphillic nature made them ideal candidates for micelle drug delivery systems and these studies led to the discovery by the group of Kabanov that Pluronics can act as P-gp inhibitors in drug resistant cells. Systems using pluronics as P-gp inhibitors have reached clinical trials[250,251], but efforts are in progress to elucidate the mechanism(s) of inhibition. In a recent review by Alakhov and Kabanov[252] the MDR inhibition mechanism is described as involving complex interactions at various layers within the cell. The first interaction takes place at the cell surface and involves the inhibition of P-gp. When the hydrophobic core of the pluronic inserts itself into the cell membrane it alters the lipid environment around P-gp, which is important for proper P-gp function.[252]

The effect Pluronics have on P-gp function has been the most widely studied polymeric interaction with P-gp; however, the effect of other polymers on P-gp or of P-gp on other polymers are still being discovered. Early attempts to evade P-gp expulsion of doxorubicin were made by conjugation of doxorubicin to HPMA-based copolymers. This conjugation took place at the primary amine on doxorubicin, which is necessary for recognition by P-gp, and thus allowed doxorubicin to accumulate intracellularly.[253,254] Sakai-Kato et al. have also studied the interactions of polymer conjugated doxorubicin, however they found that their doxorubicin conjugated polyethylene glycol-polyaspartate micelles still intereacted with P-gp.[255] In further studies they evaluated the same polymeric micelles with various dyes and drugs conjugated and concluded that the polymer itself was recognized by P-gp.[256]

1.6 Design Criteria and Rationale

In this work, a targeted drug delivery system toward P-gp is proposed. Figure 1.1 summarizes the

proposed mechanism through which P-gp can be targeted. First a nanoparticle containing a PEG linker and P-gp substrate approaches a P-gp expressing cell. The P-gp substrate crosses into the cell membrane where it is recognized and pulled through an intermembrane pore into one of two binding pockets. This effectively tethers the particle at the cell surface and allows local drug release.

A PLA-PEG particle platform was chosen for this work as each moiety of the copolymer provides an advantage in biological systems.[257] PEG provides greater biodistribution[257] and poly(lactide)s provide biological compatibility and biodegradability[258]. A 5000 M_n PEG was chosen as it is able to cross into the cell membrane without providing a significant amount of steric hindrance. The contour length (maxiumu chain length) and Flory radius (random coil radius) for PEG 5000 have been found to be 47.9 nm[259] and 6.7 nm[260] respectively. Given that a typical cell membrane is 4-5 nm thick[261] (3-4 nm for the hydrophobic core and 1 nm for the polar head groups), this PEG length should be sufficient to allow the P-gp substrate to cross into the cell membrane. PEG 5000 was also found to have the maximum effect on reducing protein adsorption to the surface of nanoparticles [262].

The rhodamine dye class of P-gp substrates was chosen for the targeting moiety of this system since they represent a well characterized class of P-gp substrates and possess conjugatable functional groups. Rhodamine123, is a good P-gp substrate and is particularly well represented in the literature as a probe to quantify the activity of the protein under different conditions.[263–265] Rhodamine123 (Rho123) has played a historic role in the detection of P-gp inhibitors and in the analysis of potential treatments for multidrug resistant (MDR) cancers.[266–269] Rhodamine 6G (Rho6G) is another rhodamine dye that has also been used for P-gp studies.[270–273] Although Rho6G is not as widely used as Rho123 it has been shown to have a greater affinity to P-gp.[263]

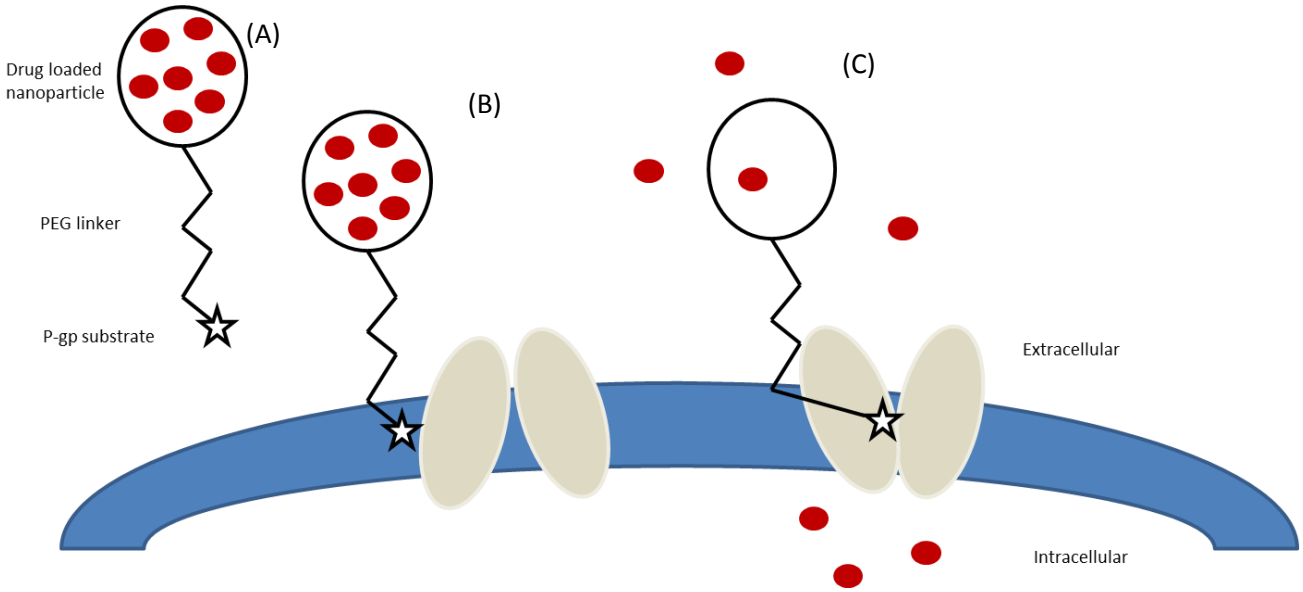

Figure 1.1. Tethering of drug delivery carriers to cells through interaction with P-gp. (A) Drug carrier/PEG linker/P-gp substrate (B) PEG linker spans membrane as P-gp substrate diffuses into cell membrane. (C) Export of P-gp substrate by P-gp tethers drug carrier to cell and drug is released locally.

REFERENCES

(1) Cdc. (2014) 2013 Mortality Multiple Cause Micro-data Files.

(2) American Cancer Society. (2015) Cancer Facts & Figures 2015.

(3) DiMasi, J. a, Feldman, L., Seckler, a, and Wilson, a. (2010) Trends in risks associated with new drug development: success rates for investigational drugs. *Clin. Pharmacol. Ther. 87*, 272–277.

(4) Abbott, N. J. (2013) Blood-brain barrier structure and function and the challenges for CNS drug delivery. *J. Inherit. Metab. Dis. 36*, 437–449.

(5) Abbott, N. J., Patabendige, A. a K., Dolman, D. E. M., Yusof, S. R., and Begley, D. J. (2010) Structure and function of the blood-brain barrier. *Neurobiol. Dis. 37*, 13–25.

(6) Allen, T. M., and Cullis, P. R. (2004) Drug delivery systems: entering the mainstream. *Science (80-.). 303*, 1818–22.

(7) Vail, D. M., Amantea, M. a., Colbern, G. T., Martin, F. J., Hilger, R. a., and Working, P. K. (2004) Pegylated liposomal doxorubicin: Proof of principle using preclinical animal models and pharmacokinetic studies. *Semin. Oncol. 31*, 16–35.

(8) Puri, A., Loomis, K., Smith, B., Lee, J.-H., Yavlovich, A., Heldman, E., and Blumenthal, R. (2009) Lipid-based nanoparticles as pharmaceutical drug carriers: from concepts to clinic. *Crit. Rev. Ther. Drug Carrier Syst. 26*, 523–580.

(9) Verreault, M., Strutt, D., Masin, D., Anantha, M., Yung, A., Kozlowski, P., Waterhouse, D., Bally, M. B., and Yapp, D. T. (2011) Vascular normalization in orthotopic glioblastoma following intravenous treatment with lipid-based nanoparticulate formulations of irinotecan (Irinophore C^{TM}), doxorubicin (Caelyx®) or vincristine. *BMC Cancer 11*, 124.

(10) Ishii, T., Asai, T., Oyama, D., Agato, Y., Yasuda, N., Fukuta, T., Shimizu, K., Minamino, T., and Oku, N. (2013) Treatment of cerebral ischemia-reperfusion injury with PEGylated liposomes encapsulating FK506. *FASEB J. 27*, 1362–1370.

(11) Ishii, T., Asai, T., Oyama, D., Fukuta, T., Yasuda, N., Shimizu, K., Minamino, T., and Oku, N. (2012) Amelioration of cerebral ischemia-reperfusion injury based on liposomal drug delivery system with asialo-erythropoietin. *J. Control. Release 160*, 81–87.

(12) Leyva-Gómez, G., González-Trujano, M. E., López-Ruiz, E., Couraud, P.-O., Wekslerg, B., Romero, I., Miller, F., Delie, F., Allémann, E., and Quintanar-Guerrero, D. (2014) Nanoparticle Formulation Improves the Anticonvulsant Effect of Clonazepam on the Pentylenetetrazole-Induced Seizures: Behavior and Electroencephalogram. *J. Pharm. Sci. 103*, 2509–2519.

(13) Dhawan, S., Kapil, R., and Singh, B. (2011) Formulation development and systematic optimization of solid lipid nanoparticles of quercetin for improved brain delivery. *J. Pharm. Pharmacol. 63*, 342–351.

(14) Gan, Q., and Wang, T. (2007) Chitosan nanoparticle as protein delivery carrier-Systematic examination of fabrication conditions for efficient loading and release. *Colloids Surfaces B Biointerfaces 59*, 24–34.

(15) Lalatsa, A., Garrett, N. L., Ferrarelli, T., Moger, J., Schätzlein, a. G., and Uchegbu, I. F. (2012) Delivery of peptides to the blood and brain after oral uptake of quaternary ammonium palmitoyl glycol chitosan nanoparticles. *Mol. Pharm. 9*, 1764–1774.

(16) Lalatsa, A., Lee, V., Malkinson, J. P., Zloh, M., Schätzlein, A. G., and Uchegbu, I. F. (2012) A prodrug nanoparticle approach for the oral delivery of a hydrophilic peptide, leucine5-enkephalin, to the brain. *Mol. Pharm. 9*, 1665–1680.

(17) Malmo, J., Sandvig, A., Vårum, K. M., and Strand, S. P. (2013) Nanoparticle Mediated P-Glycoprotein Silencing for Improved Drug Delivery across the Blood-Brain Barrier: A siRNA-Chitosan Approach. *PLoS One 8*.

(18) Kreuter, J., Shamenkov, D., Petrov, V., Ramge, P., Cychutek, K., Koch-Brandt, C., and Alyautdin, R. (2002) Apolipoprotein-mediated transport of nanoparticle-bound drugs across the blood-brain barrier. *J. Drug Target. 10*, 317–325.

(19) Wang, S. W., Monagle, J., McNulty, C., Putnam, D., and Chen, H. (2004) Determination of P-glycoprotein inhibition by excipients and their combinations using an integrated high-throughput process. *J. Pharm. Sci. 93*, 2755–2767.

(20) Nagpal, K., Singh, S. K., and Mishra, D. N. (2013) Nanoparticle mediated brain targeted delivery of gallic acid: in vivo behavioral and biochemical studies for protection against scopolamine-induced amnesia. *Drug Deliv. 20*, 112–9.

(21) Li, J., Cai, P., Shalviri, A., Henderson, J. T., He, C., Foltz, W. D., Prasad, P., Brodersen, P. M., Chen, Y., Dacosta, R., and Rauth, A. M. (2014) A Multifunctional Polymeric Nanotheranostic System Delivers Doxorubicin and Imaging Agents across the Blood À Brain Barrier Targeting Brain Metastases of Breast Cancer. *ACS Nano 8*, 9925–9940.

(22) Şimşek, S., Eroğlu, H., Kurum, B., and Ulubayram, K. (2012) Brain targeting of Atorvastatin loaded amphiphilic PLGA-b-PEG nanoparticles. *J. Microencapsul. 30*, 1–11.

(23) Kolter, M., Ott, M., Hauer, C., Reimold, I., and Fricker, G. (2015) Nanotoxicity of poly(n-butylcyano-acrylate) nanoparticles at the blood–brain barrier, in human whole blood and in vivo. *J. Control. Release 197*, 165–179.

(24) Sun, M., Gao, Y., Guo, C., Cao, F., Song, Z., Xi, Y., Yu, A., Li, A., and Zhai, G. (2010) Enhancement of transport of curcumin to brain in mice by poly(n-butylcyanoacrylate) nanoparticle. *J. Nanoparticle Res. 12*, 3111–3122.

(25) Lin, Y., Pan, Y., Shi, Y., Huang, X., Jia, N., and Jiang, J. (2012) Delivery of large molecules via poly(butyl cyanoacrylate) nanoparticles into the injured rat brain. *Nanotechnology 23*, 165101.

(26) Zhao, L., Liu, A., Yu, S., Wang, Z., Lin, X., Zhai, G., and Zhang, Q. (2013) The permeability of puerarin loaded poly(butylcyanoacrylate) nanoparticles coated with polysorbate 80 on the blood-brain

barrier and its protective effect against cerebral ischemia/reperfusion injury. *Biol. Pharm. Bull. 36*, 1263–70.

(27) Tahara, K., Miyazaki, Y., Kawashima, Y., Kreuter, J., and Yamamoto, H. (2011) Brain targeting with surface-modified poly(d,l-lactic-co-glycolic acid) nanoparticles delivered via carotid artery administration. *Eur. J. Pharm. Biopharm. 77*, 84–88.

(28) Gelperina, S., Maksimenko, O., Khalansky, A., Vanchugova, L., Shipulo, E., Abbasova, K., Berdiev, R., Wohlfart, S., Chepurnova, N., and Kreuter, J. (2010) Drug delivery to the brain using surfactant-coated poly(lactide-co-glycolide) nanoparticles: Influence of the formulation parameters. *Eur. J. Pharm. Biopharm. 74*, 157–163.

(29) Chen, Y.-C., Hsieh, W.-Y., Lee, W.-F., and Zeng, D.-T. (2011) Effects of surface modification of PLGA-PEG-PLGA nanoparticles on loperamide delivery efficiency across the blood-brain barrier. *J. Biomater. Appl. 27*, 909–922.

(30) Petri, B., Bootz, a., Khalansky, a., Hekmatara, T., Müller, R., Uhl, R., Kreuter, J., and Gelperina, S. (2007) Chemotherapy of brain tumour using doxorubicin bound to surfactant-coated poly(butyl cyanoacrylate) nanoparticles: Revisiting the role of surfactants. *J. Control. Release 117*, 51–58.

(31) Lu, W., Zhang, Y., Tan, Y. Z., Hu, K. L., Jiang, X. G., and Fu, S. K. (2005) Cationic albumin-conjugated pegylated nanoparticles as novel drug carrier for brain delivery. *J. Control. Release 107*, 428–448.

(32) Nel, A., Xia, T., Mädler, L., and Li, N. (2006) Toxic potential of materials at the nanolevel. *Science (80-.). 311*, 622–627.

(33) Gillies, E. R., and Fréchet, J. M. J. (2005) Dendrimers and dendritic polymers in drug delivery. *Drug Discov. Today 10*, 35–43.

(34) Kesharwani, P., Jain, K., and Jain, N. K. (2014) Dendrimer as nanocarrier for drug delivery. *Prog. Polym. Sci. 39*, 268–307.

(35) Albertazzi, L., Gherardini, L., Brondi, M., Sulis Sato, S., Bifone, A., Pizzorusso, T., Ratto, G. M., and Bardi, G. (2013) In vivo distribution and toxicity of PAMAM dendrimers in the central nervous system depend on their surface chemistry. *Mol. Pharm. 10*, 249–260.

(36) Jiménez, J. L., Clemente, M. I., Weber, N. D., Sanchez, J., Ortega, P., de la Mata, F. J., Gómez, R., García, D., López-Fernández, L. a, and Muñoz-Fernández, M. A. (2010) Carbosilane dendrimers to transfect human astrocytes with small interfering RNA targeting human immunodeficiency virus. *BioDrugs 24*, 331–343.

(37) Serramía, M. J., Álvarez, S., Fuentes-Paniagua, E., Clemente, M. I., Sánchez-Nieves, J., Gómez, R., de la Mata, J., and Muñoz-Fernández, M. Á. (2015) In vivo delivery of siRNA to the brain by carbosilane dendrimer. *J. Control. Release 200*, 60–70.

(38) Cintra E Silva, D. D. O., Estevanato, L. L. C., Simioni, A. R., De Andrade Rodrigues, M. M., Lacava, B. M., Lacava, Z. G. M., Tedesco, A. C., Morais, P. C., and Báo, S. N. (2012) Successful strategy for targeting the central nervous system using magnetic albumin nanospheres. *J. Biomed. Nanotechnol.*

(39) Harrison, J., Bartlett, C. a., Cowin, G., Nicholls, P. K., Evans, C. W., Clemons, T. D., Zdyrko, B., Luzinov, I. a., Harvey, A. R., Iyer, K. S., Dunlop, S. a., and Fitzgerald, M. (2012) In vivo imaging and biodistribution of multimodal polymeric nanoparticles delivered to the optic nerve. *Small 8*, 1579–1589.

(40) Pilakka-Kanthikeel, S., Atluri, V. S. R., Sagar, V., and Nair, M. (2013) Targeted Brain Derived Neurotropic Factors (BDNF) Delivery across the Blood-Brain Barrier for Neuro-Protection Using Magnetic Nano Carriers: An In-Vitro Study. *PLoS One 8*.

(41) Jiang, X., Xin, H., Sha, X., Gu, J., Jiang, Y., Law, K., Chen, Y., Chen, L., Wang, X., and Fang, X. (2011) PEGylated poly(trimethylene carbonate) nanoparticles loaded with paclitaxel for the treatment of advanced glioma: In vitro and in vivo evaluation. *Int. J. Pharm. 420*, 385–394.

(42) Jensen, S. a, Day, E. S., Ko, C. H., Hurley, L. a, Luciano, J. P., Kouri, F. M., Merkel, T. J., Luthi, A. J., Patel, P. C., Cutler, J. I., Daniel, W. L., Scott, A. W., Rotz, M. W., Meade, T. J., Giljohann, D. a, Mirkin, C. a, and Stegh, A. H. (2013) Spherical nucleic acid nanoparticle conjugates as an RNAi-based therapy for glioblastoma. *Sci. Transl. Med. 5*, 209ra152.

(43) Sun, C., Lee, J. S. H., and Zhang, M. (2008) Magnetic nanoparticles in MR imaging and drug delivery. *Adv. Drug Deliv. Rev. 60*, 1252–1265.

(44) Pêgo, A. P., Van Luyn, M. J. A., Brouwer, L. A., van Wachem, P. B., Poot, A., Grijpma, D. W., and Feijen, J. (2003) In vivo behavior of poly(1,3-trimethylene carbonate) and copolymers of 1,3-trimethylene carbonate with D,L-lactide or epsilon-caprolactone: Degradation and tissue response. *J. Biomed. Mater. Res. A 67*, 1044–1054.

(45) Pêgo, A. P., Poot, A. a., Grijpma, D. W., and Feijen, J. (2002) In vitro degradation of trimethylene carbonate based (Co)polymers. *Macromol. Biosci. 2*, 411–419.

(46) Ghosh, P., Han, G., De, M., Kim, C. K., and Rotello, V. M. (2008) Gold nanoparticles in delivery applications. *Adv. Drug Deliv. Rev. 60*, 1307–1315.

(47) Lonser, R. R., Sarntinoranont, M., Morrison, P. F., and Oldfield, E. H. (2015) Convection-enhanced delivery to the central nervous system. *J Neurosurg 122*, 697–706.

(48) Westphal, M., Hilt, D. C., Bortey, E., Delavault, P., Olivares, R., Warnke, P. C., Whittle, I. R., Jääskeläinen, J., and Ram, Z. (2003) A phase 3 trial of local chemotherapy with biodegradable carmustine (BCNU) wafers (Gliadel wafers) in patients with primary malignant glioma. *Neuro. Oncol. 5*, 79–88.

(49) Westphal, M., Ram, Z., Riddle, V., Hilt, D., and Bortey, E. (2006) Gliadel(R) wafer in initial surgery for malignant glioma: Long-term follow-up of a multicenter controlled trial. *Acta Neurochir. (Wien). 148*, 269–275.

(50) Hiramatsu, R., Kawabata, S., Tanaka, H., Sakurai, Y., Suzuki, M., Ono, K., Miyatake, S.-I., Kuroiwa, T., Hao, E., and Vicente, M. G. H. (2015) Tetrakis(p -Carboranylthio-Tetrafluorophenyl)Chlorin (TPFC): Application for Photodynamic Therapy and Boron Neutron Capture Therapy. *J. Pharm. Sci. 104*, 962–970.

(51) Suzuki, A., Leland, P., Kobayashi, H., Choyke, P. L., Jagoda, E. M., Inoue, T., Joshi, B. H., and Puri, R. K. (2014) Analysis of Biodistribution of Intracranially Infused Radiolabeled Interleukin-13 Receptor-

Targeted Immunotoxin IL-13PE by SPECT/CT in an Orthotopic Mouse Model of Human Glioma. *J. Nucl. Med. 55*, 1323–1329.

(52) Yin, D., Zhai, Y., Gruber, H. E., Ibanez, C. E., Robbins, J. M., Kells, a P., Kasahara, N., Forsayeth, J., Jolly, D. J., and Bankiewicz, K. S. (2013) Convection-enhanced delivery improves distribution and efficacy of tumor-selective retroviral replicating vectors in a rodent brain tumor model. *Cancer Gene Ther. 20*, 336–41.

(53) Kogias, E., Osterberg, N., Baumer, B., Psarras, N., Koentges, C., Papazoglou, A., Saavedra, J. E., Keefer, L. K., and Weyerbrock, A. (2012) Growth-inhibitory and chemosensitizing effects of the glutathione-S-transferase-π-activated nitric oxide donor PABA/NO in malignant gliomas. *Int. J. Cancer 130*, 1184–94.

(54) Nakamura, T., Saito, R., Sugiyama, S. I., Sonoda, Y., Kumabe, T., and Tominaga, T. (2011) Local convection-enhanced delivery of chemotherapeutic agent transiently opens blood-brain barrier and improves efficacy of systemic chemotherapy in intracranial xenograft tumor model. *Cancer Lett. 310*, 77–83.

(55) Thorne, R. G., and Nicholson, C. (2006) In vivo diffusion analysis with quantum dots and dextrans predicts the width of brain extracellular space. *Proc. Natl. Acad. Sci. U. S. A. 103*, 5567–5572.

(56) Nance, E. a., Woodworth, G. F., Sailor, K. a., Shih, T.-Y., Xu, Q., Swaminathan, G., Xiang, D., Eberhart, C., and Hanes, J. (2012) A Dense Poly(Ethylene Glycol) Coating Improves Penetration of Large Polymeric Nanoparticles Within Brain Tissue. *Sci. Transl. Med. 4*, 149ra119–149ra119.

(57) Corem-Salkmon, E., Ram, Z., Daniels, D., Perlstein, B., Last, D., Salomon, S., Tamar, G., Shneor, R., Guez, D., Margel, S., and Mardor, Y. (2011) Convection-enhanced delivery of methotrexate-loaded maghemite nanoparticles. *Int. J. Nanomedicine 6*, 1595–1602.

(58) Çirpanli, Y., Allard, E., Passirani, C., Bilensoy, E., Lemaire, L., Çaliş, S., and Benoit, J. P. (2011) Antitumoral activity of camptothecin-loaded nanoparticles in 9L rat glioma model. *Int. J. Pharm. 403*, 201–206.

(59) Nance, E., Zhang, C., Shih, T. Y., Xu, Q., Schuster, B. S., and Hanes, J. (2014) Brain-penetrating nanoparticles improve paclitaxel efficacy in malignant glioma following local administration. *ACS Nano 8*, 10655–10664.

(60) Zhou, J., Patel, T. R., Sirianni, R. W., Strohbehn, G., Zheng, M.-Q., Duong, N., Schafbauer, T., Huttner, A. J., Huang, Y., Carson, R. E., Zhang, Y., Sullivan, D. J., Piepmeier, J. M., and Saltzman, W. M. (2013) Highly penetrative, drug-loaded nanocarriers improve treatment of glioblastoma. *Proc. Natl. Acad. Sci. U. S. A. 110*, 11751–6.

(61) Vinchon-Petit, S., Jarnet, D., Paillard, A., Benoit, J. P., Garcion, E., and Menei, P. (2010) In vivo evaluation of intracellular drug-nanocarriers infused into intracranial tumours by convection-enhanced delivery: Distribution and radiosensitisation efficacy. *J. Neurooncol. 97*, 195–205.

(62) Huo, T., Barth, R. F., Yang, W., Nakkula, R. J., Koynova, R., Tenchov, B., Chaudhury, A. R., Agius, L., Boulikas, T., Elleaume, H., and Lee, R. J. (2012) Preparation, Biodistribution and Neurotoxicity of Liposomal Cisplatin following Convection Enhanced Delivery in Normal and F98 Glioma Bearing Rats. *PLoS One 7*.

(63) Yokosawa, M., Sonoda, Y., Sugiyama, S., Saito, R., Yamashita, Y., Nishihara, M., Satoh, T., Kumabe, T., Yokoyama, M., and Tominaga, T. (2010) Convection-enhanced delivery of a synthetic retinoid Am80, loaded into polymeric micelles, prolongs the survival of rats bearing intracranial glioblastoma xenografts. *Tohoku J. Exp. Med. 221*, 257–264.

(64) Allard, E., Jarnet, D., Vessières, A., Vinchon-Petit, S., Jaouen, G., Benoit, J. P., and Passirani, C. (2010) Local delivery of ferrociphenol lipid nanocapsules followed by external radiotherapy as a synergistic treatment against intracranial 9L glioma xenograft. *Pharm. Res. 27*, 56–64.

(65) Stephen, Z. R., Kievit, F. M., Veiseh, O., Chiarelli, P. A., Fang, C., Wang, K., Hatzinger, S. J., Ellenbogen, R. G., Silber, J. R., Zhang, M., and Al, S. E. T. (2014) Redox-Responsive Magnetic Nanoparticle for Targeted Convection-Enhanced Delivery of O 6 - Benzylguanine to Brain Tumors. *ACS Nano* 10383–10395.

(66) Yang, W., Barth, R. F., Huo, T., Nakkula, R. J., Weldon, M., Gupta, N., Agius, L., and Grecula, J. C. (2014) Radiation therapy combined with intracerebral administration of carboplatin for the treatment of brain tumors. *Radiat. Oncol. 9*, 25.

(67) Lueshen, E., LaRiviere, M., Yamini, B., and Linninger, A. (2014) Computer simulations and in vivo convection-enhanced delivery of fluorescent nanoparticles demonstrate variable distribution geometry. *Comput. Chem. Eng. 71*, 672–676.

(68) Kenny, G. D., Bienemann, A. S., Tagalakis, A. D., Pugh, J. a., Welser, K., Campbell, F., Tabor, A. B., Hailes, H. C., Gill, S. S., Lythgoe, M. F., McLeod, C. W., White, E. a., and Hart, S. L. (2013) Multifunctional receptor-targeted nanocomplexes for the delivery of therapeutic nucleic acids to the Brain. *Biomaterials 34*, 9190–9200.

(69) Writer, M. J., Kyrtatos, P. G., Bienemann, A. S., Pugh, J. a., Lowe, A. S., Villegas-Llerena, C., Kenny, G. D., White, E. a., Gill, S. S., McLeod, C. W., Lythgoe, M. F., and Hart, S. L. (2012) Lipid peptide nanocomplexes for gene delivery and magnetic resonance imaging in the brain. *J. Control. Release 162*, 340–348.

(70) Stiles, D. K., Zhang, Z., Ge, P., Nelson, B., Grondin, R., Ai, Y., Hardy, P., Nelson, P. T., Guzaev, A. P., Butt, M. T., Charisse, K., Kosovrasti, V., Tchangov, L., Meys, M., Maier, M., Nechev, L., Manoharan, M., Kaemmerer, W. F., Gwost, D., Stewart, G. R., Gash, D. M., and Sah, D. W. Y. (2012) Widespread suppression of huntingtin with convection-enhanced delivery of siRNA. *Exp. Neurol. 233*, 463–471.

(71) Martin Bauknight, W., Chakrabarty, S., Hwang, B. Y., Malone, H. R., Joshi, S., Bruce, J. N., Sander Connolly, E., Winfree, C. J., Cunningham, M. G., Martin, J. H., and Haque, R. (2012) Convection enhanced drug delivery of BDNF through a microcannula in a rodent model to strengthen connectivity of a peripheral motor nerve bridge model to bypass spinal cord injury. *J. Clin. Neurosci. 19*, 563–569.

(72) Sewing, A. C. P., Caretti, V., Lagerweij, T., Schellen, P., Jansen, M. H. a., van Vuurden, D. G., Idema, S., Molthoff, C. F. M., Vandertop, W. P., Kaspers, G. J. L., Noske, D. P., and Hulleman, E. (2014) Convection enhanced delivery of carmustine to the murine brainstem: A feasibility study. *J. Neurosci. Methods 238*, 88–94.

(73) Xi, G., Rajaram, V., Mania-Farnell, B., Mayanil, C. S., Soares, M. B., Tomita, T., and Goldman, S. (2012) Efficacy of vincristine administered via convection-enhanced delivery in a rodent brainstem tumor model documented by bioluminescence imaging. *Child's Nerv. Syst. 28*, 565–574.

(74) Yan, Y., Miyamoto, Y., Nitta, A., Muramatsu, S.-I., Ozawa, K., Yamada, K., and Nabeshima, T. (2013) Intrastriatal gene delivery of GDNF persistently attenuates methamphetamine self-administration and relapse in mice. *Int. J. Neuropsychopharmacol. 16*, 1559–67.

(75) Astary, G. W., Kantorovich, S., Carney, P. R., Mareci, T. H., and Sarntinoranont, M. (2010) Regional convection-enhanced delivery of gadolinium-labeled albumin in the rat hippocampus in vivo. *J. Neurosci. Methods 187*, 129–137.

(76) Kim, J. H., Astary, G. W., Nobrega, T. L., Kantorovich, S., Carney, P. R., Mareci, T. H., and Sarntinoranont, M. (2012) Dynamic contrast-enhanced MRI of Gd-albumin delivery to the rat hippocampus in vivo by convection-enhanced delivery. *J. Neurosci. Methods 209*, 62–73.

(77) Ding, D., Kanaly, C. W., Bigner, D. D., Cummings, T. J., Herndon, J. E., Pastan, I., Raghavan, R., and Sampson, J. H. (2010) Convection-enhanced delivery of free gadolinium with the recombinant immunotoxin MR1-1. *J. Neurooncol. 98*, 1–7.

(78) Hardy, P. a., Keeley, D., Schorn, G., Forman, E., Ai, Y., Venugopalan, R., Zhang, Z., and Bradley, L. H. (2013) Convection enhanced delivery of different molecular weight tracers of gadolinium-tagged polylysine. *J. Neurosci. Methods 219*, 169–175.

(79) Haar, P. J., Broaddus, W. C., Chen, Z.-J., Fatouros, P. P., Gillies, G. T., and Corwin, F. D. (2010) Quantification of convection-enhanced delivery to the ischemic brain. *Physiol. Meas. 31*, 1075–1089.

(80) Salegio, E. a, Streeter, H., Dube, N., Hadaczek, P., Samaranch, L., Kells, A. P., San Sebastian, W., Zhai, Y., Bringas, J., Xu, T., Forsayeth, J., and Bankiewicz, K. S. (2014) Distribution of nanoparticles throughout the cerebral cortex of rodents and non-human primates: Implications for gene and drug therapy. *Front. Neuroanat. 8*, 9.

(81) Sugiyama, S., Saito, R., Nakamura, T., Yamashita, Y., Yokosawa, M., Sonoda, Y., Kumabe, T., Watanabe, M., and Tominaga, T. (2012) Safety and feasibility of convection-enhanced delivery of nimustine hydrochloride co-infused with free gadolinium for real-time monitoring in the primate brain. *Neurol. Res. 34*, 581–587.

(82) San Sebastian, W., Richardson, R. M., Kells, A. P., Lamarre, C., Bringas, J., Pivirotto, P., Salegio, E. a., DeArmond, S. J., Forsayeth, J., and Bankiewicz, K. S. (2012) Safety and Tolerability of Magnetic Resonance Imaging-Guided Convection-Enhanced Delivery of AAV2-hAADC with a Novel Delivery Platform in Nonhuman Primate Striatum. *Hum. Gene Ther. 23*, 210–217.

(83) White, E., Bienemann, A., Taylor, H., Hopkins, K., Cameron, A., and Gill, S. (2012) A phase I trial of carboplatin administered by convection-enhanced delivery to patients with recurrent/progressive glioblastoma multiforme. *Contemp. Clin. Trials 33*, 320–331.

(84) Bruce, J. N., Fine, R. L., Canoll, P., Yun, J., Kennedy, B. C., Rosenfeld, S. S., Sands, S. a., Surapaneni, K., Lai, R., Yanes, C. L., Bagiella, E., and Delapaz, R. L. (2011) Regression of recurrent malignant gliomas with convection-enhanced delivery of topotecan. *Neurosurgery 69*, 1272–1279.

(85) Anderson, R. C. E., Kennedy, B., Yanes, C. L., Garvin, J., Needle, M., Canoll, P., Feldstein, N. a, and Bruce, J. N. (2013) Convection-enhanced delivery of topotecan into diffuse intrinsic brainstem tumors in children. *J. Neurosurg. Pediatr. 11*, 289–95.

(86) Bogdahn, U., Hau, P., Stockhammer, G., Venkataramana, N. K., Mahapatra, a K., Suri, A., Balasubramaniam, A., Nair, S., Oliushine, V., Parfenov, V., Poverennova, I., Zaaroor, M., Jachimczak, P., Ludwig, S., Schmaus, S., Heinrichs, H., Schlingensiepen, K. H., and Trabedersen Glioma Study, G. (2011) Targeted therapy for high-grade glioma with the TGF-beta2 inhibitor trabedersen: results of a randomized and controlled phase IIb study. *Neuro. Oncol. 13*, 42–132.

(87) Kunwar, S., Chang, S., Westphal, M., Vogelbaum, M., Sampson, J., Barnett, G., Shaffrey, M., Ram, Z., Piepmeier, J., Prados, M., Croteau, D., Pedain, C., Leland, P., Husain, S. R., Joshi, B. H., and Puri, R. K. (2010) Phase III randomized trial of CED of IL13-PE38QQR vs Gliadel wafers for recurrent glioblastoma. *Neuro. Oncol. 12*, 871–881.

(88) Shahar, T., Ram, Z., and Kanner, A. a. (2012) Convection-enhanced delivery catheter placements for high-grade gliomas: Complications and pitfalls. *J. Neurooncol. 107*, 373–378.

(89) Vazquez, L. C., Hagel, E., Willenberg, B. J., Dai, W., Casanova, F., Batich, C. D., and Sarntinoranont, M. (2012) Polymer-coated cannulas for the reduction of backflow during intraparenchymal infusions. *J. Mater. Sci. Mater. Med. 23*, 2037–2046.

(90) Casanova, F., Carney, P. R., and Sarntinoranont, M. (2014) In vivo evaluation of needle force and friction stress during insertion at varying insertion speed into the brain. *J. Neurosci. Methods 237*, 79–89.

(91) Casanova, F., Carney, P. R., and Sarntinoranont, M. (2012) Influence of Needle Insertion Speed on Backflow for Convection-Enhanced Delivery. *J. Biomech. Eng. 134*, 041006.

(92) Hood, R. L., Andriani, R. T., Emch, S., Robertson, J. L., Rylander, C. G., and Rossmeisl, J. H. (2013) Fiberoptic microneedle device facilitates volumetric infusate dispersion during convection-enhanced delivery in the brain. *Lasers Surg. Med. 45*, 418–426.

(93) Barua, N. U., Woolley, M., Bienemann, a. S., Johnson, D. E., Lewis, O., Wyatt, M. J., Irving, C., O'Sullivan, S., Murray, G., Fennelly, C., Skinner, P., and Gill, S. S. (2013) Intermittent convection-enhanced delivery to the brain through a novel transcutaneous bone-anchored port. *J. Neurosci. Methods 214*, 223–232.

(94) Gill, T., Barua, N. U., Woolley, M., Bienemann, a. S., Johnson, D. E., S.O'Sullivan, Murray, G., Fennelly, C., Lewis, O., Irving, C., Wyatt, M. J., Moore, P., and Gill, S. S. (2013) In vitro and in vivo testing of a novel recessed-step catheter for reflux-free convection-enhanced drug delivery to the brain. *J. Neurosci. Methods 219*, 1–9.

(95) Meredith, M. E., Salameh, T. S., and Banks, W. a. (2015) Intranasal Delivery of Proteins and Peptides in the Treatment of Neurodegenerative Diseases. *AAPS J.*

(96) Pardridge, W. M. (2002) Drug and gene delivery to the brain: The vascular route. *Neuron 36*, 555–558.

(97) Alcalá-Barraza, S. R., Lee, M. S., Hanson, L. R., McDonald, A. a, Frey, W. H., and McLoon, L. K. (2010) Intranasal delivery of neurotrophic factors BDNF, CNTF, EPO, and NT-4 to the CNS. *J. Drug Target. 18*, 179–190.

(98) Lu, T., Jiang, Y., Zhou, Z., Yue, X., Wei, N., Chen, Z., Ma, M., Xu, G., and Liu, X. (2011) Intranasal ginsenoside Rb1 targets the brain and ameliorates cerebral ischemia/reperfusion injury in rats. *Biol. Pharm. Bull. 34*, 1319–1324.

(99) Colombo, G., Lorenzini, L., Zironi, E., Galligioni, V., Sonvico, F., Balducci, A. G., Pagliuca, G., Giuliani, A., Calzà, L., and Scagliarini, A. (2011) Brain distribution of ribavirin after intranasal administration. *Antiviral Res. 92*, 408–414.

(100) Wong, Y. C., and Zuo, Z. (2013) Brain disposition and catalepsy after intranasal delivery of loxapine: Role of metabolism in PK/PD of intranasal CNS drugs. *Pharm. Res. 30*, 2368–2384.

(101) Mainardes, R. M., Urban, M. C. C., Cinto, P. O., Chaud, M. V., Evangelista, R. C., and Gremião, M. P. D. (2006) Liposomes and micro/nanoparticles as colloidal carriers for nasal drug delivery. *Curr. Drug Deliv. 3*, 275–285.

(102) Hoekman, J. D., Srivastava, P., and Ho, R. J. Y. (2014) Aerosol-stable peptide-coated liposome nanoparticles: A proof-of-concept study with opioid fentanyl in enhancing analgesic effects and reducing plasma drug exposure. *J. Pharm. Sci. 103*, 2231–2239.

(103) Alam, M. I., Baboota, S., Ahuja, A., Ali, M., Ali, J., and Sahni, J. K. (2012) Intranasal administration of nanostructured lipid carriers containing CNS acting drug: Pharmacodynamic studies and estimation in blood and brain. *J. Psychiatr. Res. 46*, 1133–1138.

(104) Dalpiaz, A., Ferraro, L., Perrone, D., Leo, E., Iannuccelli, V., Pavan, B., Paganetto, G., Beggiato, S., and Scalia, S. (2014) Brain uptake of a zidovudine prodrug after nasal administration of solid lipid microparticles. *Mol. Pharm. 11*, 1550–1561.

(105) Patil, G. B., and Surana, S. J. (2013) Fabrication and statistical optimization of surface engineered PLGA nanoparticles for naso-brain delivery of ropinirole hydrochloride: in-vitro–ex-vivo studies. *J. Biomater. Sci. Polym. Ed. 24*, 1740–1756.

(106) Chiappetta, D. A., Hocht, C., Opezzo, J. A., and Sosnik, A. (2013) Intranasal administration of antiretroviral-loaded micelles for anatomical targeting to the brain in HIV. *Nanomedicine 8*, 223–237.

(107) Kamei, N., and Takeda-morishita, M. (2015) Brain delivery of insulin boosted by intranasal coadministration with cell-penetrating peptides. *J. Control. Release 197*, 105–110.

(108) Kanazawa, T., Akiyama, F., Kakizaki, S., Takashima, Y., and Seta, Y. (2013) Delivery of siRNA to the brain using a combination of nose-to-brain delivery and cell-penetrating peptide-modified nano-micelles. *Biomaterials 34*, 9220–9226.

(109) Yang, Z. Z., Zhang, Y. Q., Wang, Z. Z., Wu, K., Lou, J. N., and Qi, X. R. (2013) Enhanced brain distribution and pharmacodynamics of rivastigmine by liposomes following intranasal administration. *Int. J. Pharm. 452*, 344–354.

(110) Bies, C., Lehr, C. M., and Woodley, J. F. (2004) Lectin-mediated drug targeting: History and applications. *Adv. Drug Deliv. Rev. 56*, 425–435.

(111) Issa, M. M., Köping-Höggård, M., and Artursson, P. (2005) Chitosan and the mucosal delivery of biotechnology drugs. *Drug Discov. Today Technol. 2*, 1–6.

(112) Zhang, X., Liu, L., Chai, G., Zhang, X., and Li, F. (2013) Brain pharmacokinetics of neurotoxin-loaded PLA nanoparticles modified with chitosan after intranasal administration in awake rats. *Drug Dev. Ind. Pharm. 39*, 1618–24.

(113) Gavini, E., Rassu, G., Ferraro, L., Generosi, A., Rau, J. V., Brunetti, A., Giunchedi, P., and Dalpiaz, A. (2011) Influence of Chitosan Glutamate on the In Vivo Intranasal Absorption of Rokitamycin from Microspheres. *J. Pharm. Sci. 100*, 1488–1502.

(114) Rassu, G., Soddu, E., Cossu, M., Brundu, A., Cerri, G., Marchetti, N., Ferraro, L., Regan, R. F., Giunchedi, P., Gavini, E., and Dalpiaz, A. (2015) Solid microparticles based on chitosan or methyl-β-cyclodextrin: A first formulative approach to increase the nose-to-brain transport of deferoxamine mesylate. *J. Control. Release 201*, 68–77.

(115) Uchida, M., Katoh, T., Mori, M., Maeno, T., Ohtake, K., Kobayashi, J., Morimoto, Y., and Natsume, H. (2011) Intranasal administration of milnacipran in rats: evaluation of the transport of drugs to the systemic circulation and central nervous system and the pharmacological effect. *Biol. Pharm. Bull. 34*, 740–747.

(116) Wen, Z., Yan, Z., He, R., Pang, Z., Guo, L., Qian, Y., Jiang, X., and Fang, L. (2011) Brain targeting and toxicity study of odorranalectin-conjugated nanoparticles following intranasal administration. *Drug Deliv. 18*, 1–7.

(117) Zhang, C., Chen, J., Feng, C., Shao, X., Liu, Q., Zhang, Q., Pang, Z., and Jiang, X. (2014) Intranasal nanoparticles of basic fibroblast growth factor for brain delivery to treat Alzheimer's disease. *Int. J. Pharm. 461*, 192–202.

(118) Wen, Z., Yan, Z., Hu, K., Pang, Z., Cheng, X., Guo, L., Zhang, Q., Jiang, X., Fang, L., and Lai, R. (2011) Odorranalectin-conjugated nanoparticles: Preparation, brain delivery and pharmacodynamic study on Parkinson's disease following intranasal administration. *J. Control. Release 151*, 131–138.

(119) Chen, J., Zhang, C., Liu, Q., Shao, X., Feng, C., Shen, Y., Zhang, Q., and Jiang, X. (2012) Solanum tuberosum lectin-conjugated nanoparticles for nose to brain delivery: in vivo and in vitro evaluations. *J. Drug Target. 20*, 174–184.

(120) Piazza, J., Hoare, T., Molinaro, L., Terpstra, K., Bhandari, J., Selvaganapathy, P. R., Gupta, B., and Mishra, R. K. (2014) Haloperidol-loaded intranasally administered lectin functionalized poly(ethylene glycol)-block-poly(D,L)-lactic-co-glycolic acid (PEG-PLGA) nanoparticles for the treatment of schizophrenia. *Eur. J. Pharm. Biopharm. 87*, 30–39.

(121) V. Borlongan, C., E. Glover, L., R. Sanberg, P., and C. Hess, D. (2012) Permeating the Blood Brain Barrier and Abrogating the Inflammation in Stroke: Implications for Stroke Therapy. *Curr. Pharm. Des. 18*, 3670–3676.

(122) Foley, C. P., Rubin, D. G., Santillan, A., Sondhi, D., Dyke, J. P., Pierre Gobin, Y., Crystal, R. G., and Ballon, D. J. (2014) Intra-arterial delivery of AAV vectors to the mouse brain after mannitol mediated blood brain barrier disruption. *J. Control. Release 196*, 71–78.

(123) Hwang, D. W., Son, S., Jang, J., Youn, H., Lee, S., Lee, D., Lee, Y. S., Jeong, J. M., Kim, W. J., and Lee, D. S. (2011) A brain-targeted rabies virus glycoprotein-disulfide linked PEI nanocarrier for delivery of neurogenic microRNA. *Biomaterials 32*, 4968–4975.

(124) Sun, Z., Worden, M., Wroczynskyj, Y., Yathindranath, V., van Lierop, J., Hegmann, T., and Miller, D. W. (2014) Magnetic field enhanced convective diffusion of iron oxide nanoparticles in an osmotically disrupted cell culture model of the blood-brain barrier. *Int. J. Nanomedicine 9*, 3013–3026.

(125) Yao, S. T., and May, C. N. (2013) Intra-carotid angiotensin II activates tyrosine hydroxylase-expressing rostral ventrolateral medulla neurons following blood-brain barrier disruption in rats. *Neuroscience 245*, 148–156.

(126) Okuma, Y., Wang, F., Toyoshima, A., Kameda, M., Hishikawa, T., Tokunaga, K., Sugiu, K., Liu, K., Haruma, J., Nishibori, M., Yasuhara, T., and Date, I. (2013) Mannitol enhances therapeutic effects of intra-arterial transplantation of mesenchymal stem cells into the brain after traumatic brain injury. *Neurosci. Lett. 554*, 156–161.

(127) Park, T.-E., Singh, B., Li, H., Lee, J.-Y., Kang, S.-K., Choi, Y.-J., and Cho, C.-S. (2015) Enhanced BBB permeability of osmotically active poly(mannitol-co-PEI) modified with rabies virus glycoprotein via selective stimulation of caveolar endocytosis for RNAi therapeutics in Alzheimer's disease. *Biomaterials 38*, 61–71.

(128) Boockvar, J. a, Tsiouris, A. J., Hofstetter, C. P., Kovanlikaya, I., Fralin, S., Kesavabhotla, K., Seedial, S. M., Pannullo, S. C., Schwartz, T. H., Stieg, P., Zimmerman, R. D., Knopman, J., Scheff, R. J., Christos, P., Vallabhajosula, S., and Riina, H. a. (2011) Safety and maximum tolerated dose of superselective intraarterial cerebral infusion of bevacizumab after osmotic blood-brain barrier disruption for recurrent malignant glioma. Clinical article. *J. Neurosurg. 114*, 624–632.

(129) Joshi, S., Ergin, A., Wang, M., Reif, R., Zhang, J., Bruce, J. N., and Bigio, I. J. (2011) Inconsistent blood brain barrier disruption by intraarterial mannitol in rabbits: Implications for chemotherapy. *J. Neurooncol. 104*, 11–19.

(130) Chen, K.-B., Wei, V. C., Yen, L. F., Poon, K.-S., Liu, Y.-C., Cheng, K.-S., Chang, C.-S., and Lai, T. W. (2013) Intravenous mannitol does not increase blood-brain barrier permeability to inert dyes in the adult rat forebrain. *Neuroreport 24*, 303–7.

(131) Garg, P., Pandey, S., Seonwoo, H., Yeom, S., Choung, Y.-H., Cho, C.-S., Choung, P.-H., and Hoon Chung, J. (2015) Hyperosmotic polydixylitol for crossing the blood brain barrier and efficient nucleic acid delivery. *Chem. Commun. 51*, 3645–3648.

(132) Yan-Yu, X., Qi-Neng, P., and Zhi-Peng, C. (2007) The enhancing effect of synthetical borneol on the absorption of tetramethylpyrazine phosphate in mouse. *Int. J. Pharm. 337*, 74–79.

(133) Ren, J., Zou, M., Gao, P., Wang, Y., and Cheng, G. (2013) Tissue distribution of borneol-modified ganciclovir-loaded solid lipid nanoparticles in mice after intravenous administration. *Eur. J. Pharm. Biopharm. 83*, 141–148.

(134) Yu, B., Ruan, M., Cui, X. B., Guo, J. M., Xu, L., and Dong, X. P. (2013) Effects of borneol on the pharmacokinetics of geniposide in cortex, hippocampus, hypothalamus and striatum of conscious rat by simultaneous brain microdialysis coupled with UPLC-MS. *J. Pharm. Biomed. Anal. 77*, 128–132.

(135) On, N. H., Savant, S., Toews, M., and Miller, D. W. (2013) Rapid and reversible enhancement of blood-brain barrier permeability using lysophosphatidic acid. *J. Cereb. Blood Flow Metab. 33*, 1–11.

(136) Lu, H., Demny, S., Zuo, Y., Rea, W., Wang, L., Chefer, S. I., Vaupel, D. B., Yang, Y., and Stein, E. a. (2010) Temporary disruption of the rat blood-brain barrier with a monoclonal antibody: A novel method for dynamic manganese-enhanced MRI. *Neuroimage 50*, 7–14.

(137) Bakay, L., Hueter, T. F., Ballantine, H., and Sosa, D. (1956) Ultrasonically Produced Changes in the Blood-Brain Barrier. *AMA Arch. Neurol. Psychiatry 76*, 457–467.

(138) Hynynen, K., McDannold, N., Vykhodtseva, N., and Jolesz, F. a. (2001) Noninvasive MR imaging-guided focal opening of the blood-brain barrier in rabbits. *Radiology 220*, 640–646.

(139) Aryal, M., Arvanitis, C. D., Alexander, P. M., and McDannold, N. (2014) Ultrasound-mediated blood-brain barrier disruption for targeted drug delivery in the central nervous system. *Adv. Drug Deliv. Rev. 72*, 94–109.

(140) Yang, F. Y., Lin, Y. L., Chou, F. I., Lin, Y. C., Liu, Y. W. H., Chang, L. W., and Hsieh, Y. L. (2014) Pharmacokinetics of BPA in gliomas with ultrasound induced blood-brain barrier disruption as measured by microdialysis. *PLoS One 9*, 1–6.

(141) Park, J., Zhang, Y., Vykhodtseva, N., Jolesz, F. a., and McDannold, N. J. (2012) The kinetics of blood brain barrier permeability and targeted doxorubicin delivery into brain induced by focused ultrasound. *J. Control. Release 162*, 134–142.

(142) Choi, J. J., Selert, K., Gao, Z., Samiotaki, G., Baseri, B., and Konofagou, E. E. (2011) Noninvasive and localized blood-brain barrier disruption using focused ultrasound can be achieved at short pulse lengths and low pulse repetition frequencies. *J. Cereb. Blood Flow Metab. 31*, 725–737.

(143) Chen, H., Chen, C. C., Acosta, C., Wu, S.-Y., Sun, T., and Konofagou, E. E. (2014) A New Brain Drug Delivery Strategy: Focused Ultrasound-Enhanced Intranasal Drug Delivery. *PLoS One 9*, e108880.

(144) Lammers, T., Koczera, P., Fokong, S., Gremse, F., Ehling, J., Vogt, M., Pich, A., Storm, G., van Zandvoort, M., and Kiessling, F. (2015) Theranostic USPIO-Loaded Microbubbles for Mediating and Monitoring Blood-Brain Barrier Permeation. *Adv. Funct. Mater. 25*, 36–43.

(145) Shi, L., Palacio-mancheno, P., Badami, J., Zeng, M., Cardoso, L., Tu, R., and Fu, B. M. (2014) Quantification of transient increase of the blood – brain barrier permeability to macromolecules by optimized focused ultrasound combined with microbubbles 4437–4448.

(146) Baseri, B., Choi, J. J., Deffieux, T., Samiotaki, G., Tung, Y.-S., Olumolade, O., Small, S. a, Morrison, B., and Konofagou, E. E. (2012) Activation of signaling pathways following localized delivery of systemically administered neurotrophic factors across the blood–brain barrier using focused ultrasound and microbubbles. *Phys. Med. Biol. 57*, N65–N81.

(147) Wang, F., Shi, Y., Lu, L., Liu, L., Cai, Y., Zheng, H., Liu, X., Yan, F., Zou, C., Sun, C., Shi, J., Lu, S., and Chen, Y. (2012) Targeted Delivery of GDNF through the Blood-Brain Barrier by MRI-Guided Focused Ultrasound. *PLoS One 7*, 1–8.

(148) Kumar, A., Zhang, X., and Liang, X.-J. (2012) Gold Nanoparticles: Emerging Paradigm for Targeted Drug Delivery System. *Biotechnol. Adv. 31*, 593–606.

(149) Etame, A. B., Diaz, R. J., O'Reilly, M. a., Smith, C. a., Mainprize, T. G., Hynynen, K., and Rutka, J. T. (2012) Enhanced delivery of gold nanoparticles with therapeutic potential into the brain using MRI-guided focused ultrasound. *Nanomedicine Nanotechnology, Biol. Med. 8*, 1133–1142.

(150) Diaz, R. J., McVeigh, P. Z., O'Reilly, M. a., Burrell, K., Bebenek, M., Smith, C., Etame, A. B., Zadeh, G., Hynynen, K., Wilson, B. C., and Rutka, J. T. (2014) Focused ultrasound delivery of Raman nanoparticles across the blood-brain barrier: Potential for targeting experimental brain tumors. *Nanomedicine Nanotechnology, Biol. Med. 10*, 1075–1087.

(151) Nance, E., Timbie, K., Miller, G. W., Song, J., Louttit, C., Klibanov, A. L., Shih, T. Y., Swaminathan, G., Tamargo, R. J., Woodworth, G. F., Hanes, J., and Price, R. J. (2014) Non-invasive delivery of stealth, brain-penetrating nanoparticles across the blood - Brain barrier using MRI-guided focused ultrasound. *J. Control. Release 189*, 123–132.

(152) Yang, F. Y., Wong, T. T., Teng, M. C., Liu, R. S., Lu, M., Liang, H. F., and Wei, M. C. (2012) Focused ultrasound and interleukin-4 receptor-targeted liposomal doxorubicin for enhanced targeted drug delivery and antitumor effect in glioblastoma multiforme. *J. Control. Release 160*, 652–658.

(153) Alonso, A., Reinz, E., Leuchs, B., Kleinschmidt, J., Fatar, M., Geers, B., Lentacker, I., Hennerici, M. G., de Smedt, S. C., Meairs, S., and Tyagi, A. (2013) Focal delivery of AAV2/1-transgenes into the rat brain by localized ultrasound-induced BBB Opening. *Mol. Ther. acids 73*, 1–6.

(154) Hsu, P.-H., Wei, K.-C., Huang, C.-Y., Wen, C.-J., Yen, T.-C., Liu, C.-L., Lin, Y.-T., Chen, J.-C., Shen, C.-R., and Liu, H.-L. (2013) Noninvasive and targeted gene delivery into the brain using microbubble-facilitated focused ultrasound. *PLoS One 8*, e57682.

(155) Huang, Q., Deng, J., Wang, F., Chen, S., Liu, Y., Wang, Z., Wang, Z., and Cheng, Y. (2012) Targeted gene delivery to the mouse brain by MRI-guided focused ultrasound-induced blood-brain barrier disruption. *Exp. Neurol. 233*, 350–356.

(156) Huang, Q., Deng, J., Xie, Z., Wang, F., Chen, S., Lei, B., Liao, P., Huang, N., Wang, Z., Wang, Z., and Cheng, Y. (2012) Effective Gene Transfer into Central Nervous System Following Ultrasound-Microbubbles-Induced Opening of the Blood-Brain Barrier. *Ultrasound Med. Biol. 38*, 1234–1243.

(157) Burgess, A., Huang, Y., Querbes, W., Sah, D. W., and Hynynen, K. (2012) Focused ultrasound for targeted delivery of siRNA and efficient knockdown of Htt expression. *J. Control. Release 163*, 125–129.

(158) Alkins, R. D., Brodersen, P. M., Sodhi, R. N., and Hynynen, K. (2013) Enhancing drug delivery for boron neutron capture therapy of brain tumors with focused ultrasound. *Neuro Oncol 15*, 1225–1235.

(159) Liu, H.-L., Hua, M.-Y., Chen, P.-Y., Chu, P.-C., Pan, C.-H., Yang, H.-W., Huang, C.-Y., Wang, J.-J., Yen, T.-C., and Wei, K.-C. (2010) Blood-brain barrier disruption with focused ultrasound enhances delivery of chemotherapeutic drugs for glioblastoma treatment. *Radiology 255*, 415–425.

(160) Ting, C. Y., Fan, C. H., Liu, H. L., Huang, C. Y., Hsieh, H. Y., Yen, T. C., Wei, K. C., and Yeh, C. K. (2012) Concurrent blood-brain barrier opening and local drug delivery using drug-carrying microbubbles and focused ultrasound for brain glioma treatment. *Biomaterials 33*, 704–712.

(161) Liu, H.-L., Hua, M.-Y., Yang, H.-W., Huang, C.-Y., Chu, P.-C., Wu, J.-S., Tseng, I.-C., Wang, J.-J., Yen, T.-C., Chen, P.-Y., and Wei, K.-C. (2010) Magnetic resonance monitoring of focused ultrasound/magnetic nanoparticle targeting delivery of therapeutic agents to the brain. *Proc. Natl. Acad. Sci. U. S. A. 107*, 15205–15210.

(162) Park, E. J., Zhang, Y. Z., Vykhodtseva, N., and McDannold, N. (2012) Ultrasound-mediated blood-brain/blood-tumor barrier disruption improves outcomes with trastuzumab in a breast cancer brain metastasis model. *J. Control. Release 163*, 277–284.

(163) O'Reilly, M. a., Waspe, A. C., Ganguly, M., and Hynynen, K. (2011) Focused-Ultrasound Disruption of the Blood-Brain Barrier Using Closely-Timed Short Pulses: Influence of Sonication Parameters and Injection Rate. *Ultrasound Med. Biol. 37*, 587–594.

(164) O'Reilly, M. a, Huang, Y., and Hynynen, K. (2010) The impact of standing wave effects on transcranial focused ultrasound disruption of the blood-brain barrier in a rat model. *Phys. Med. Biol. 55*, 5251–5267.

(165) Samiotaki, G., and Konofagou, E. E. (2013) Dependence of the reversibility of focused-ultrasound-induced blood-brain barrier opening on pressure and pulse length in vivo. *IEEE Trans. Ultrason. Ferroelectr. Freq. Control 60*, 2257–2265.

(166) Yang, F.-Y., Lin, G.-L., Horng, S., Chang, T.-K., Wu, S.-Y., Wong, T.-T., and Wang, H.-E. (2011) Pulsed high-intensity focused ultrasound enhances the relative permeability of the blood–tumor barrier in a glioma-bearing rat model. *IEEE Trans. Ultrason. Ferroelectr. Freq. Control 58*, 964–970.

(167) Liu, H.-L., Wai, Y.-Y., Hsu, P.-H., Lyu, L.-A., Wu, J.-S., Shen, C.-R., Chen, J.-C., Yen, T.-C., and Wang, J.-J. (2010) In vivo assessment of macrophage CNS infiltration during disruption of the blood-brain barrier with focused ultrasound: a magnetic resonance imaging study. *J. Cereb. Blood Flow Metab. 30*, 177–186.

(168) Aryal, M., Vykhodtseva, N., Zhang, Y.-Z., and McDannold, N. (2015) Multiple sessions of liposomal doxorubicin delivery via focused ultrasound mediated blood–brain barrier disruption: A safety study. *J. Control. Release 204*, 60–69.

(169) Riganti, C., Gazzano, E., Gulino, G. R., Volante, M., Ghigo, D., and Kopecka, J. (2015) Two repeated low doses of doxorubicin are more effective than a single high dose against tumors overexpressing P-glycoprotein. *Cancer Lett. 360*, 219–226.

(170) Marquet, F., Tung, Y. S., Teichert, T., Ferrera, V. P., and Konofagou, E. E. (2011) Noninvasive, transient and selective Blood-Brain barrier opening in Non-Human primates in vivo. *PLoS One 6*, 1–7.

(171) McDannold, N., Arvanitis, C. D., Vykhodtseva, N., and Livingstone, M. S. (2012) Temporary disruption of the blood-brain barrier by use of ultrasound and microbubbles: Safety and efficacy evaluation in rhesus macaques. *Cancer Res. 72*, 3652–3663.

(172) Skarlatos, S., Yoshikawa, T., and Pardridge, W. M. (1995) Transport of [125I]transferrin through the rat blood-brain barrier. *Brain Res. 683*, 164–171.

(173) Qian, Z. M., Li, H., Sun, H., and Ho, K. (2002) Targeted drug delivery via the transferrin receptor-mediated endocytosis pathway. *Pharmacol. Rev. 54*, 561–587.

(174) Kuo, Y.-C., and Chou, P.-R. (2014) Neuroprotection Against Degeneration of SK-N-MC Cells Using Neuron Growth Factor-Encapsulated Liposomes with Surface Cereport and Transferrin. *J. Pharm. Sci. 103*, 2484–2497.

(175) Kuo, Y. C., and Wang, L. J. (2014) Transferrin-grafted catanionic solid lipid nanoparticles for targeting delivery of saquinavir to the brain. *J. Taiwan Inst. Chem. Eng. 45*, 755–763.

(176) Mahajan, S. D., Law, W. C., Aalinkeel, R., Reynolds, J., Nair, B. B., Yong, K. T., Roy, I., Prasad, P. N., and Schwartz, S. a. (2012) Nanoparticle-mediated targeted delivery of antiretrovirals to the brain. *Methods Enzymol.* 1st ed. Elsevier Inc.

(177) Mahajan, S. D., Roy, I., Xu, G., Yong, K.-T., Ding, H., Aalinkeel, R., Reynolds, J., Sykes, D., Nair, B. B., Lin, E. Y., Prasad, P. N., and Schwartz, S. a. (2010) Enhancing the delivery of anti retroviral drug "Saquinavir" across the blood brain barrier using nanoparticles. *Curr. HIV Res. 8*, 396–404.

(178) Laakkonen, J. P., Engler, T., Romero, I. a., Weksler, B., Couraud, P. O., Kreppel, F., and Kochanek, S. (2012) Transcellular Targeting of Fiber- and Hexon-Modified Adenovirus Vectors across the Brain Microvascular Endothelial Cells In Vitro. *PLoS One 7*, 3–11.

(179) Gan, C. W., and Feng, S. S. (2010) Transferrin-conjugated nanoparticles of Poly(lactide)-d- aplha-Tocopheryl polyethylene glycol succinate diblock copolymer for targeted drug delivery across the blood-brain barrier. *Biomaterials 31*, 7748–7757.

(180) Pang, Z., Gao, H., Yu, Y., Guo, L., Chen, J., Pan, S., Ren, J., Wen, Z., and Jiang, X. (2011) Enhanced intracellular delivery and chemotherapy for glioma rats by transferrin-conjugated biodegradable polymersomes loaded with doxorubicin. *Bioconjug. Chem. 22*, 1171–1180.

(181) Porru, M., Zappavigna, S., Salzano, G., Luce, A., Balestrieri, M. L., Artuso, S., Lusa, S., De, G., Leonetti, C., and Caraglia, M. (2014) Medical treatment of orthotopic glioblastoma with transferrin-conjugated nanoparticles encapsulating zoledronic acid *5*.

(182) Zhang, P., Hu, L., Yin, Q., Zhang, Z., Feng, L., and Li, Y. (2012) Transferrin-conjugated polyphosphoester hybrid micelle loading paclitaxel for brain-targeting delivery: Synthesis, preparation and in vivo evaluation. *J. Control. Release 159*, 429–434.

(183) Pardridge, W. M., Buciak, J. L., and Friden, P. M. (1991) Selective transport of an anti-transferrin receptor antibody through the blood-brain barrier in vivo. *J. Pharmacol. Exp. Ther. 259*, 66–70.

(184) Bommana, M. M., Kirthivasan, B., and Squillante, E. (2012) brain microdialysis to evaluate FITC-dextran encapsulated immunopegylated nanoparticles. *Drug Deliv. 19*, 298–306.

(185) Markoutsa, E., Papadia, K., Giannou, a. D., Spella, M., Cagnotto, a., Salmona, M., Stathopoulos, G. T., and Antimisiaris, S. G. (2014) Mono and dually decorated nanoliposomes for brain targeting, in vitro and in vivo studies. *Pharm. Res. 31*, 1275–1289.

(186) Mourtas, S., Lazar, A. N., Markoutsa, E., Duyckaerts, C., and Antimisiaris, S. G. (2014) Multifunctional nanoliposomes with curcumin-lipid derivative and brain targeting functionality with potential applications for Alzheimer disease. *Eur. J. Med. Chem. 80*, 175–183.

(187) Carroll, R. T., Bhatia, D., Geldenhuys, W., Bhatia, R., Miladore, N., Bishayee, A., and Sutariya, V. (2010) Brain-targeted delivery of Tempol-loaded nanoparticles for neurological disorders. *J. Drug Target. 18*, 665–674.

(188) Couch, J. a, Yu, Y. J., Zhang, Y., Tarrant, J. M., Fuji, R. N., Meilandt, W. J., Solanoy, H., Tong, R. K., Hoyte, K., Luk, W., Lu, Y., Gadkar, K., Prabhu, S., Ordonia, B. a, Nguyen, Q., Lin, Y., Lin, Z., Balazs, M., Scearce-Levie, K., Ernst, J. a, Dennis, M. S., and Watts, R. J. (2013) Addressing safety liabilities of TfR bispecific antibodies that cross the blood-brain barrier. *Sci. Transl. Med. 5*, 183ra57, 1–12.

(189) Pardridge, W. M. (2015) Blood–brain barrier drug delivery of IgG fusion proteins with a transferrin receptor monoclonal antibody. *Expert Opin. Drug Deliv. 12*, 207–222.

(190) Lee, J. H., Engler, J. a., Collawn, J. F., and Moore, B. a. (2001) Receptor mediated uptake of peptides that bind the human transferrin receptor. *Eur. J. Biochem. 268*, 2004–2012.

(191) Youn, P., Chen, Y., and Furgeson, D. Y. (2014) A myristoylated cell-penetrating peptide bearing a transferrin receptor-targeting sequence for neuro-targeted siRNA delivery. *Mol. Pharm. 11*, 486–495.

(192) Prades, R., Guerrero, S., Araya, E., Molina, C., Salas, E., Zurita, E., Selva, J., Egea, G., López-Iglesias, C., Teixidó, M., Kogan, M. J., and Giralt, E. (2012) Delivery of gold nanoparticles to the brain by conjugation with a peptide that recognizes the transferrin receptor. *Biomaterials 33*, 7194–7205.

(193) Vivès, E., Schmidt, J., and Pèlegrin, A. (2008) Cell-penetrating and cell-targeting peptides in drug delivery. *Biochim. Biophys. Acta - Rev. Ca 1786*, 126–138.

(194) Koivunen, E., Arap, W., Rajotte, D., Lahdenranta, J., and Pasqualini, R. (1999) Identification of receptor ligands with phage display peptide libraries. *J. Nucl. Med. 40*, 883–888.

(195) Gonzalez, A. M., Leadbeater, W. E., Burg, M., Sims, K., Terasaki, T., Johanson, C. E., Stopa, E. G., Eliceiri, B. P., and Baird, A. (2011) Targeting choroid plexus epithelia and ventricular ependyma for drug delivery to the central nervous system. *BMC Neurosci. 12*, 4.

(196) Li, J., Feng, L., Fan, L., Zha, Y., Guo, L., Zhang, Q., Chen, J., Pang, Z., Wang, Y., Jiang, X., Yang, V. C., and Wen, L. (2011) Targeting the brain with PEG-PLGA nanoparticles modified with phage-displayed peptides. *Biomaterials 32*, 4943–4950.

(197) Zhang, C., Zheng, X., Wan, X., Shao, X., Liu, Q., Zhang, Z., and Zhang, Q. (2014) The potential use of H102 peptide-loaded dual-functional nanoparticles in the treatment of Alzheimer's disease. *J. Control. Release 192*, 317–324.

(198) Zhang, C., Wan, X., Zheng, X., Shao, X., Liu, Q., Zhang, Q., and Qian, Y. (2014) Dual-functional nanoparticles targeting amyloid plaques in the brains of Alzheimer's disease mice. *Biomaterials 35*, 456–465.

(199) Mathew, A., Fukuda, T., Nagaoka, Y., Hasumura, T., Morimoto, H., Yoshida, Y., Maekawa, T., Venugopal, K., and Kumar, D. S. (2012) Curcumin loaded-PLGA nanoparticles conjugated with Tet-1 peptide for potential use in Alzheimer's disease. *PLoS One 7*.

(200) Bu, G. (2009) Apolipoprotein E and its receptors in Alzheimer's disease: pathways, pathogenesis and therapy. *Nat. Rev. Neurosci. 10*, 333–344.

(201) Re, F., Cambianica, I., Zona, C., Sesana, S., Gregori, M., Rigolio, R., La Ferla, B., Nicotra, F., Forloni, G., Cagnotto, A., Salmona, M., Masserini, M., and Sancini, G. (2011) Functionalization of liposomes with ApoE-derived peptides at different density affects cellular uptake and drug transport across a blood-brain barrier model. *Nanomedicine Nanotechnology, Biol. Med. 7*, 551–559.

(202) Re, F., Cambianica, I., Sesana, S., Salvati, E., Cagnotto, A., Salmona, M., Couraud, P. O., Moghimi, S. M., Masserini, M., and Sancini, G. (2010) Functionalization with ApoE-derived peptides enhances the interaction with brain capillary endothelial cells of nanoliposomes binding amyloid-beta peptide. *J. Biotechnol. 156*, 341–346.

(203) Wang, D., El-Amouri, S. S., Dai, M., Kuan, C.-Y., Hui, D. Y., Brady, R. O., and Pan, D. (2013) Engineering a lysosomal enzyme with a derivative of receptor-binding domain of apoE enables delivery across the blood-brain barrier. *Proc. Natl. Acad. Sci. U. S. A. 110*, 2999–3004.

(204) Shao, K., Huang, R., Li, J., Han, L., Ye, L., Lou, J., and Jiang, C. (2010) Angiopep-2 modified PE-PEG based polymeric micelles for amphotericin B delivery targeted to the brain. *J. Control. Release 147*, 118–126.

(205) Xin, H., Jiang, X., Gu, J., Sha, X., Chen, L., Law, K., Chen, Y., Wang, X., Jiang, Y., and Fang, X. (2011) Angiopep-conjugated poly(ethylene glycol)-co-poly(e-caprolactone) nanoparticles as dual-targeting drug delivery system for brain glioma. *Biomaterials 32*, 4293–4305.

(206) Shao, K., Wu, J., Chen, Z., Huang, S., Li, J., Ye, L., Lou, J., Zhu, L., and Jiang, C. (2012) A brain-vectored angiopep-2 based polymeric micelles for the treatment of intracranial fungal infection. *Biomaterials 33*, 6898–6907.

(207) Xin, H., Sha, X., Jiang, X., Zhang, W., Chen, L., and Fang, X. (2012) Anti-glioblastoma efficacy and safety of paclitaxel-loading Angiopep-conjugated dual targeting PEG-PCL nanoparticles. *Biomaterials 33*, 8167–8176.

(208) Gao, X., Qian, J., Zheng, S., Xiong, Y., Man, J., Cao, B., Wang, L., Ju, S., and Li, C. (2013) Up-regulating blood brain barrier permeability of nanoparticles via multivalent effect. *Pharm. Res. 30*, 2538–2548.

(209) Wei, X., Zhan, C., Chen, X., Hou, J., Xie, C., and Lu, W. (2014) Retro-Inverso Isomer of Angiopep-2: A Stable d-Peptide Ligand Inspires Brain-Targeted Drug Delivery. *Mol. Pharm.*

(210) Malcor, J. D., Payrot, N., David, M., Faucon, A., Abouzid, K., Jacquot, G., Floquet, N., Debarbieux, F., Rougon, G., Martinez, J., Khrestchatisky, M., Vlieghe, P., and Lisowski, V. (2012) Chemical optimization of new ligands of the low-density lipoprotein receptor as potential vectors for central nervous system targeting. *J. Med. Chem. 55*, 2227–2241.

(211) Zhang, B., Sun, X., Mei, H., Wang, Y., Liao, Z., Chen, J., Zhang, Q., Hu, Y., Pang, Z., and Jiang, X. (2013) LDLR-mediated peptide-22-conjugated nanoparticles for dual-targeting therapy of brain glioma. *Biomaterials 34*, 9171–9182.

(212) Fu, A., Wang, Y., Zhan, L., and Zhou, R. (2012) Targeted delivery of proteins into the central nervous system mediated by rabies virus glycoprotein-derived peptide. *Pharm. Res. 29*, 1562–1569.

(213) Tosi, G., Vergoni, a. V., Ruozi, B., Bondioli, L., Badiali, L., Rivasi, F., Costantino, L., Forni, F., and Vandelli, M. a. (2010) Sialic acid and glycopeptides conjugated PLGA nanoparticles for central nervous system targeting: In vivo pharmacological evidence and biodistribution. *J. Control. Release 145*, 49–57.

(214) Tosi, G., Vilella, A., Chhabra, R., Schmeisser, M. J., Boeckers, T. M., Ruozi, B., Vandelli, M. A., Forni, F., Zoli, M., and Grabrucker, A. M. (2014) Insight on the fate of CNS-targeted nanoparticles. Part II: Intercellular neuronal cell-to-cell transport. *J. Control. Release 177*, 96–107.

(215) Vilella, A., Tosi, G., Grabrucker, A. M., Ruozi, B., Belletti, D., Vandelli, M. A., Boeckers, T. M., Forni, F., and Zoli, M. (2014) Insight on the fate of CNS-targeted nanoparticles. Part I: Rab5-dependent cell-specific uptake and distribution. *J. Control. Release 174*, 195–201.

(216) Grabrucker, A. M., Garner, C. C., Boeckers, T. M., Bondioli, L., Ruozi, B., Forni, F., Vandelli, M. A., and Tosi, G. (2011) Development of novel Zn2+ loaded Nanoparticles designed for cell-type targeted drug release in CNS neurons: In vitro evidences. *PLoS One 6*.

(217) Grover, A., Hirani, A., Pathak, Y., and Sutariya, V. (2014) Brain-Targeted Delivery of Docetaxel by Glutathione-Coated Nanoparticles for Brain Cancer. *AAPS PharmSciTech 15*, 1562–1568.

(218) Patel, P. J., Acharya, N. S., and Acharya, S. R. (2013) Development and characterization of glutathione-conjugated albumin nanoparticles for improved brain delivery of hydrophilic fluorescent marker. *Drug Deliv. 7544*, 1–13.

(219) Kuo, Y. C., and Hong, T. Y. (2014) Delivering etoposide to the brain using catanionic solid lipid nanoparticles with surface 5-HT-moduline. *Int. J. Pharm. 465*, 132–142.

(220) Birngruber, T., Raml, R., Gladdines, W., Gatschelhofer, C., Gander, E., Ghosh, A., Kroath, T., Gaillard, P. J., Pieber, T. R., and Sinner, F. (2014) Enhanced doxorubicin delivery to the brain administered through glutathione PEGylated liposomal doxorubicin (2B3-101) as compared with generic Caelyx,??/Doxil?? - A Cerebral open flow microperfusion pilot study. *J. Pharm. Sci. 103*, 1945–1948.

(221) Gaillard, P. J., Appeldoorn, C. C. M., Rip, J., Dorland, R., Van Der Pol, S. M. a, Kooij, G., De Vries, H. E., and Reijerkerk, A. (2012) Enhanced brain delivery of liposomal methylprednisolone improved therapeutic efficacy in a model of neuroinflammation. *J. Control. Release 164*, 364–369.

(222) Wang, T., Kievit, F. M., Veiseh, O., Arami, H., Stephen, Z. R., Fang, C., Liu, Y., Ellenbogen, R. G., and Zhang, M. (2013) Targeted cell uptake of a noninternalizing antibody through conjugation to iron oxide nanoparticles in primary central nervous system lymphoma. *World Neurosurg. 80*, 134–141.

(223) Cerqueira, S. R., Silva, B. L., Oliveira, J. M., Mano, J. F., Sousa, N., Salgado, A. J., and Reis, R. L. (2012) Multifunctionalized CMCht/PAMAM Dendrimer Nanoparticles Modulate the Cellular Uptake by Astrocytes and Oligodendrocytes in Primary Cultures of Glial Cells. *Macromol. Biosci. 12*, 591–597.

(224) Dan, M., Cochran, D. B., Yokel, R. a., and Dziubla, T. D. (2013) Binding, transcytosis and biodistribution of anti-PECAM-1 iron oxide nanoparticles for brain-targeted delivery. *PLoS One 8*, 2–9.

(225) Schneider, C. S., Perez, J. G., Cheng, E., Zhang, C., Mastorakos, P., Hanes, J., Winkles, J. a., Woodworth, G. F., and Kim, A. J. (2015) Minimizing the non-specific binding of nanoparticles to the brain enables active targeting of Fn14-positive glioblastoma cells. *Biomaterials 42*, 42–51.

(226) Farrington, G. K., Caram-Salas, N., Haqqani, A. S., Brunette, E., Eldredge, J., Pepinsky, B., Antognetti, G., Baumann, E., Ding, W., Garber, E., Jiang, S., Delaney, C., Boileau, E., Sisk, W. P., and Stanimirovic, D. B. (2014) A novel platform for engineering blood-brain barrier-crossing bispecific biologics. *FASEB J.*

(227) Kuo, Y. C., and Chung, C. Y. (2012) Transcytosis of CRM197-grafted polybutylcyanoacrylate nanoparticles for delivering zidovudine across human brain-microvascular endothelial cells. *Colloids Surfaces B Biointerfaces 91*, 242–249.

(228) Filler, A. G., Whiteside, G. T., Bacon, M., Frederickson, M., Howe, F. a, Rabinowitz, M. D., Sokoloff, A. J., Deacon, T. W., Abell, C., Munglani, R., Griffiths, J. R., Bell, B. A., and Lever, A. M. L. (2010) Tri-partite complex for axonal transport drug delivery achieves pharmacological effect. *BMC Neurosci. 11*, 8.

(229) Qu, B., Li, X., Guan, M., Li, X., Hai, L., and Wu, Y. (2014) Design, synthesis and biological evaluation of multivalent glucosides with high affinity as ligands for brain targeting liposomes. *Eur. J. Med. Chem. 72*, 110–118.

(230) Zhao, Y., Qu, B., Wu, X., Li, X., Liu, Q., Jin, X., Guo, L., Hai, L., and Wu, Y. (2014) Design, synthesis and biological evaluation of brain targeting L-ascorbic acid prodrugs of ibuprofen with "lock-in" function. *Eur. J. Med. Chem. 82*, 314 – 323.

(231) Pyla, R., Poulose, N., Jun, J. Y., and Segar, L. (2013) Expression of conventional and novel glucose transporters, GLUT1, -9, -10, and -12, in vascular smooth muscle cells. *Am. J. Physiol. Cell Physiol. 304*, C574–C589.

(232) Chen, Y. C., Chiang, C. F., Chen, L. F., Liao, S. C., Hsieh, W. Y., and Lin, W. L. (2014) Polymersomes conjugated with des-octanoyl ghrelin for the delivery of therapeutic and imaging agents into brain tissues. *Biomaterials 35*, 2051–2065.

(233) Pang, Z., Feng, L., Hua, R., Chen, J., and Gao, H. (1995) Lactoferrin-Conjgated Biodegradable Polymersome Holding Doxorubicin and Tetrandrine for Chemotherapy of Glioma Rats. *Mol. Pharm. 7*, 1995–2005.

(234) Hu, K., Shi, Y., Jiang, W., Han, J., Huang, S., and Jiang, X. (2011) Lactoferrin conjugated PEG-PLGA nanoparticles for brain delivery: Preparation, characterization and efficacy in Parkinsons disease. *Int. J. Pharm. 415*, 273–283.

(235) Brooks, H., Lebleu, B., and Vivès, E. (2005) Tat peptide-mediated cellular delivery: Back to basics. *Adv. Drug Deliv. Rev. 57*, 559–577.

(236) Wen, X., Wang, K., Zhao, Z., Zhang, Y., Sun, T., Zhang, F., Wu, J., Fu, Y., Du, Y., Zhang, L., Sun, Y., Liu, Y., Ma, K., Liu, H., and Song, Y. (2014) Brain-Targeted Delivery of Trans-Activating Transcriptor-Conjugated Magnetic PLGA/Lipid Nanoparticles. *PLoS One 9*, e106652.

(237) Malhotra, M., Tomaro-Duchesneau, C., Saha, S., Kahouli, I., and Prakash, S. (2013) Development and characterization of chitosan-PEG-TAT nanoparticles for the intracellular delivery of siRNA. *Int. J. Nanomedicine 8*, 2041–2052.

(238) Tian, X. H., Wei, F., Wang, T. X., Wang, D., Wang, J., Lin, X. N., Wang, P., and Ren, L. (2012) Blood-brain barrier transport of Tat peptide and polyethylene glycol decorated gelatin-siloxane nanoparticle. *Mater. Lett. 68*, 94–96.

(239) Zong, T., Mei, L., Gao, H., Shi, K., Chen, J., Wang, Y., Zhang, Q., Yang, Y., and He, Q. (2014) Enhanced Glioma Targeting and Penetration by Dual-Targeting Liposome Co-modified with T7 and TAT. *J. Pharm. Sci. 103*, 3891–3901.

(240) Cheng, Y., Dai, Q., Morshed, R. a., Fan, X., Wegscheid, M. L., Wainwright, D. a., Han, Y., Zhang, L., Auffinger, B., Tobias, A. L., Rincón, E., Thaci, B., Ahmed, A. U., Warnke, P. C., He, C., and Lesniak, M. S. (2014) Blood-Brain Barrier Permeable Gold Nanoparticles: An Efficient Delivery Platform for Enhanced Malignant Glioma Therapy and Imaging. *Small* n/a–n/a.

(241) Gu, G., Gao, X., Hu, Q., Kang, T., Liu, Z., Jiang, M., Miao, D., Song, Q., Yao, L., Tu, Y., Pang, Z., Chen, H., Jiang, X., and Chen, J. (2013) The influence of the penetrating peptide iRGD on the effect of paclitaxel-loaded MT1-AF7p-conjugated nanoparticles on glioma cells. *Biomaterials 34*, 5138–5148.

(242) Xia, H., Gao, X., Gu, G., Liu, Z., Hu, Q., Tu, Y., Song, Q., Yao, L., Pang, Z., Jiang, X., Chen, J., and Chen, H. (2012) Penetratin-functionalized PEG–PLA nanoparticles for brain drug delivery. *Int. J. Pharm. 436*, 840–850.

(243) Tian, X. H., Wei, F., Wang, T. X., Wang, P., Lin, X. N., Wang, J., Wang, D., and Ren, L. (2012) In vitro and in vivo studies on gelatin-siloxane nanoparticles conjugated with SynB peptide to increase drug delivery to the brain. *Int. J. Nanomedicine 7*, 1031–1041.

(244) Guarnieri, D., Falanga, A., Muscetti, O., Tarallo, R., Fusco, S., Galdiero, M., Galdiero, S., and Netti, P. a. (2013) Shuttle-mediated nanoparticle delivery to the blood-brain barrier. *Small 9*, 853–862.

(245) Borst, P., and Schinkel, A. H. (2013) P-glycoprotein ABCB1: a major player in drug handling by mammals. *J. Clin. Invest. 123*, 4131–4133.

(246) Sugawaraay, I., Akiyama, S., Scheper, R. J., and Itoyamaa, S. (1997) Lung resistance protein (LRP) expression in human normal tissues in comparison with that of MDRl and MRP. *Cancer Lett. 112*, 23–31.

(247) Kim, R. B. (2002) Drugs as P-glycoprotein substrates, inhibitors, and inducers. *Drug Metab. Rev. 34*, 47–54.

(248) Aller, S. G., Yu, J., Ward, A., Weng, Y., Chittaboina, S., Zhuo, R., Harrell, P. M., Trinh, Y. T., Zhang, Q., Urbatsch, I. L., and Chang, G. (2009) Structure of P-glycoprotein reveals a molecular basis for poly-specific drug binding. *Science (80-.). 323*, 1718–1722.

(249) Thomas, H., and Coley, H. M. (2003) Overcoming multidrug resistance in cancer: an update on the clinical strategy of inhibiting p-glycoprotein. *Cancer Control 10*, 159–165.

(250) Danson, S., Ferry, D., Alakhov, V., Margison, J., Kerr, D., Jowle, D., Brampton, M., Halbert, G., and Ranson, M. (2004) Phase I dose escalation and pharmacokinetic study of pluronic polymer-bound doxorubicin (SP1049C) in patients with advanced cancer. *Br. J. Cancer 90*, 2085–2091.

(251) Valle, J. W., Armstrong, A., Newman, C., Alakhov, V., Pietrzynski, G., Brewer, J., Campbell, S., Corrie, P., Rowinsky, E. K., and Ranson, M. (2011) A phase 2 study of SP1049C, doxorubicin in P-glycoprotein-targeting pluronics, in patients with advanced adenocarcinoma of the esophagus and gastroesophageal junction. *Invest. New Drugs 29*, 1029–1037.

(252) Alakhova, D. Y., and Kabanov, A. V. (2014) Pluronics and MDR reversal: An update. *Mol. Pharm. 11*, 2566–2578.

(253) Kopecek, J., Kopecková, P., Minko, T., and Lu, Z. (2000) HPMA copolymer-anticancer drug conjugates: design, activity, and mechanism of action. *Eur. J. Pharm. Biopharm. 50*, 61–81.

(254) Minko, T., Kopecková, P., and Kopecek, J. (1999) Comparision of the Anticancer Effect of Free and HPMA Copolymer-Bound Adriamycin in Human Ovarian Carcinoma Cells. *Pharm. Res. 16*, 986–996.

(255) Sakai-Kato, K., Ishikura, K., Oshima, Y., Tada, M., Suzuki, T., Ishii-Watabe, A., Yamaguchi, T., Nishiyama, N., Kataoka, K., Kawanishi, T., and Okuda, H. (2012) Evaluation of intracellular trafficking and clearance from HeLa cells of doxorubicin-bound block copolymers. *Int. J. Pharm. 423*, 401–409.

(256) Sakai-Kato, K., Un, K., Nanjo, K., Nishiyama, N., Kusuhara, H., Kataoka, K., Kawanishi, T., Goda, Y., and Okuda, H. (2014) Elucidating the molecular mechanism for the intracellular trafficking and fate of block copolymer micelles and their components. *Biomaterials 35*, 1347–1358.

(257) Avgoustakis, K. (2004) Pegylated poly(lactide) and poly(lactide-co-glycolide) nanoparticles: preparation, properties and possible applications in drug delivery. *Curr. Drug Deliv. 1*, 321–33.

(258) Panyam, J., and Labhasetwar, V. (2003) Biodegradable nanoparticles for drug and gene delivery to cells and tissue. *Adv. Drug Deliv. Rev. 55*, 329–347.

(259) Stan, G., Delrio, F. W., MacCuspie, R. I., and Cook, R. F. (2012) Nanomechanical properties of polyethylene glycol brushes on gold substrates. *J. Phys. Chem. B 116*, 3138–3147.

(260) Marsh, D., Bartucci, R., and Sportelli, L. (2003) Lipid membranes with grafted polymers: Physicochemical aspects. *Biochim. Biophys. Acta - Biomembr. 1615*, 33–59.

(261) Lodish, H., Berk, A., Zipursky, L., Matsudaira, P., Baltimore, D., and Darnell, J. (1999) Molecular Cell Biology 4th ed. Freeman, W.H., New York.

(262) Gref, R., Lu, M., Sud, P., and Pharmaceutiques, E. (2000) " Stealth " corona-core nanoparticles surface modified by polyethylene glycol (PEG): influences of the corona (PEG chain length and surface density) and of the core composition on phagocytic uptake and plasma protein adsorption. *Colloids Surfaces B Biointerfaces 18*, 301–313.

(263) Eytan, G. D., Regev, R., Oren, G., Hurwitz, C. D., and Assaraf, Y. (1997) Efficiency of P-glycoprotein-mediated exclusion of rhodamine dyes from multidrug-resistant cells is determined by their passive transmembrane movement rate. *Eur. J. Biochem. 248*, 104–112.

(264) Loetchutinat, C., Saengkhae, C., Marbeuf-Gueye, C., and Garnier-Suillerot, A. (2003) New insights into the P-glycoprotein-mediated effluxes of rhodamines. *Eur. J. Biochem. 270*, 476–485.

(265) Nare, B., Prichard, R. K., and Georges, E. (1994) Characterization of rhodamine 123 binding to P-glycoprotein in human multidrug-resistant cells. *Mol. Pharmacol. 45*, 1145–1152.

(266) Störmer, E., von Moltke, L. L., Perloff, M. D., and Greenblatt, D. J. (2002) Differential modulation of P-glycoprotein expression and activity by non-nucleoside HIV-1 reverse transcriptase inhibitors in cell culture. *Pharm. Res. 19*, 1038–1045.

(267) Tian, R., Koyabu, N., Takanaga, H., Matsuo, H., Ohtani, H., and Sawada, Y. (2002) Effects of grapefruit juice and orange juice on the intestinal efflux of P-glycoprotein substrates. *Pharm. Res. 19*, 802–809.

(268) Fröhlich, M., Albermann, N., Sauer, A., Walter-Sack, I., Haefeli, W. E., and Weiss, J. (2004) In vitro and ex vivo evidence for modulation of P-glycoprotein activity by progestins. *Biochem. Pharmacol. 68*, 2409–2416.

(269) Lee, J. S., Paull, K., Alvarez, M., Hose, C., Monks, A., Grever, M., Fojo, a T., and Bates, S. E. (1994) Rhodamine efflux patterns predict P-glycoprotein substrates in the National Cancer Institute drug screen. *Mol. Pharmacol. 46*, 627–638.

(270) Lampidis, T. J., Castello, C., Del Giglio, A., Pressman, B. C., Viallet, P., Trevorrow, K. W., Valet, G. K., Tapiero, H., and Savaraj, N. (1989) Relevance of the chemical charge of rhodamine dyes to multiple drug resistance. *Biochem. Pharmacol. 38*, 4267–4271.

(271) Roerig, D. L., Audi, S. H., and Ahlf, S. B. (2004) KINETIC CHARACTERIZATION OF P-GLYCOPROTEIN-MEDIATED EFFLUX OF RHODAMINE 6G IN THE INTACT RABBIT LUNG. *Drug Metab. Dispos. 32*, 953–958.

(272) Ichikawa, M., Yoshimura, A., Sumizawa, T., Shudo, N., Kuwazuru, Y., Furukawa, T., and Akiyama, S. (1991) Interaction of Organic Chemicals with P-glycoprotein in the Adrenal Gland, Kidney, and a Multidrug-resistant KB Cell. *J. Biol. Chem. 266*, 903–8.

(273) Sarver, J. G., Klis, W. a., Byers, J. P., and Erhardt, P. W. (2002) Microplate Screening of the Differential Effects of Test Agents on Hoechst 33342, Rhodamine 123, and Rhodamine 6G Accumulation in Breast Cancer Cells that Overexpress P-Glycoprotein. *J. Biomol. Screen. 7*, 29–34.

CHAPTER 2

SYNTHESIS AND CHARACTERIZATION OF MACROMOLECULAR RHODAMINE TETHERS AND THEIR INTERACTIONS WITH P-GLYCOPROTEIN*

2.1 Introduction

P-glycoprotein (P-gp) is an ATP-binding cassette membrane efflux protein that actively transports small molecules across the cell membrane. It is expressed in both healthy (e.g., gastrointestinal endothelium) and diseased (e.g., multidrug resistant cancers) tissues.[1–3] Although general characteristics of P-gp substrates are known, such as high lipophilicity, the protein is fairly promiscuous and transports a surprisingly wide range of structures.[4,5] The clinical ramifications of P-gp expression in cancers are well documented and the literature is replete with examples of drug targeting with antibodies against P-gp expressing cell types [6,7] or of attempts to inhibit P-gp mediated efflux of substrates.[8] However, to date the clinical impacts of these approaches have been yet to be fully realized. For these reasons, probes to evaluate the functionality of P-gp are increasingly important to help better understand the mechanism and specificity of its activity.[9,10] In particular, polymeric probes could prove useful for *in vivo* applications since the majority of probes are small molecules that often have limited circulation time.[11,12]

Polymeric materials have been extensively studied for their ability to inhibit P-gp.[13] Poloxamers are a particularly well known class of polymeric P-gp inhibitors.[14] Poloxamers inhibit P-gp by either decreasing membrane fluidity or depleting ATP.[15] The polymers do not directly interact with P-gp and are not considered substrates of the protein. Little is known about polymers acting as substrates of P-gp and our aim is to describe such interactions through the conjugation of polymers the established P-gp low molecular weight substrates.

Rhodamine dyes are one popular class of P-gp substrates. The rhodamine variant, rhodamine123, is a strong P-gp substrate and is particularly well represented in the literature as a probe to quantify the

activity of the protein under different conditions.[16–18] Rhodamine123 (Rho123) has played a historic role in the detection of P-gp inhibitors and in the analysis of potential treatments for multidrug resistant (MDR) cancers.[19–22] Although Rho123 is more widely used as a P-gp substrate, other rhodamine variants have been explored for affinity to P-gp. Rhodamine 6G (Rho6G) and Rhodamine B (RhoB) have also been used as P-gp substrates and have higher and lower, respectively, affinity to P-gp than Rho123.[16] An expansion of the potential use of rhodamines could lead to opportunities for further investigation into P-gp function. One useful expansion would be conjugation of a macromolecule to rhodamine variants. Early conjugates of rhodamine derivatives were synthesized by activation of the 4' or 5' sites[23,24], but more recently a one-step substitution of small compounds through the 2' position of Rho6G and Rho123 was reported.[25]

Herein we report the synthesis and characterization of a methoxypolyethylene glycol (mPEG) conjugate of Rho6G and Rho123 through the 2' position and characterize their interactions with P-gp (Figures 1a and 1b). PEG is a well-established tether of small molecules, peptides and proteins [11,26] and mPEG-Rho6G and mPEG-Rho123 conjugates could be useful to investigators in the P-gp field. We also compare the P-gp interaction of the 2' substituted mPEG-Rho6G and mPEG-Rho123 to the more common and commercially available 4' substituted mPEG-RhoB (Figure 1c). Recognizing that perturbations of the molecular architecture of a P-gp substrate can influence the interaction with P-gp[27], we sought to establish the retained activity of the macromolecular rhodamine conjugates using the P-gp expressing breast adenocarcinoma cell line, MDA-435/LCC6 MDR. Our results show that PEG was effectively linked to Rho6G and Rho123 in a single step as determined by both ^{1}H NMR and diffusion ordered NMR. Additionally, retention of the P-gp interaction with the PEG-Rho6G, PEG-Rho123 and PEG-RhoB conjugates were confirmed by both FACS analysis and confocal microscopy. Both techniques showed that the P-gp interaction with the conjugates directly correlated to that of free Rho6G, Rho123 and RhoB thereby establishing the potential use of these macromolecular tethers of rhodamine derivatives as P-gp interactive conjugates.

2.2 Materials and Methods

2.2.1 Materials. Dialysis tubing of 2000 g/mol molecular weight cutoff (MWCO) was purchased from Spectrum Laboratories (Rancho Dominguez, CA). Deuterated dimethyl-sulfoxide was purchased from Cambridge Isotope Laboratories (Andover, MA). Methoxy polyethyleneglycol amine (mPEG-NH_2), rhodamine 123 (Rho123), rhodamine 6G (Rho6G), rhodamine B (RhoB), anhydrous dimethylformamide (DMF), triethylamine (TEA), RIPA buffer, phosphate buffered saline (PBS) with calcium and magnesium, protease inhibitor cocktail, monoclonal anti-P-glycoprotein antibody produced in mouse, monoclonal anti-β-actin antibody produced in mouse, anti-mouse antibody produced in goat, and BCIP-blue liquid substrate were purchased from Sigma Aldrich (Saint Louis, MO). Methoxy polyethyleneglycol rhodamine B (mPEG-RhoB) was purchased from Nanocs (New York, NY). PD-10 columns were purchased from GE Healthcare Bio-sciences (Piscataway, NJ). Accutase, penicillin/streptomycin, NOVEX Bis-Tris 10% gels and MOPS running buffer were purchased from Life Technologies (Grand Island, NY). PVDF membrane was purchased from Pall Corporation (Port Washington, NY). Non-fat dry milk blotting grade blocker was purchased from Bio-Rad (Hercules, CA). Sterile cell culture phosphate buffered saline (PBS) and fetal bovine serum (FBS) were purchased from Cellgro (Manassas, VA). HyClone MEM Richter's modification with L-glutamine and phenol red was purchased from Thermo Scientific (Rockford, IL). T-flasks were purchased from Corning (Corning, NY). MDA-435/LCC6 WT and MDA-435/LCC6 MDR cells were graciously donated by Dr. Robert Clarke (MD Anderson Cancer Center, Houston, TX).

2.2.2 Synthesis of mPEG-Rho6G and mPEG-Rho123. For production of mPEG-Rho6G, the mPEG-NH_2 (M_n 5000, 241.6 mg, 4.8×10^{-5} mol) was dissolved in anhydrous DMF (2 mL) with excess TEA at room temperature. Excess TEA was added to Rho6G powder (77.2 mg, 1.6×10^{-4}mol) which was then dissolved in anhydrous DMF (12 mL) with slight heating. For production of mPEG-Rho123, mPEG-NH_2

(M_n 5000, 71.6 mg, $1.4x10^{-5}$ mol) was dissolved in anhydrous DMF (1 mL) with excess TEA at room temperature. Excess TEA was added to Rho123 powder (10.8 mg, $2.8x10^{-5}$ mol) which was then dissolved in anhydrous DMF (1 mL) at room temperature. For both mPEG-Rho6G and mPEG-Rho123 production, the two DMF solutions were combined and stirred at 30 °C for 1 week while protected from light with an aluminum foil cover. The solution was then diluted with Milli-Q water (38 mL) and dialyzed (MWCO 2000g/mol) in the dark against deionized water with 14 water exchanges over 1 week at room temperature. After dialysis the solution was dried to a light pink powder by lyophilization in the dark for 3 days. Product yields for mPEG-Rho6G and mPEG-Rho123 were 54.7% and 83%, respectively. ^{1}H NMR and diffusion ordered NMR were conducted on an Inova 600 MHz spectrometer at 25 °C. mPEG-Rho6G conjugate ^{1}H NMR (600 MHz, DMSO-d_6) δ(ppm): 3.24 (s, 3H, C**H$_3$**O mPEG), 3.5 (s, 4H, C**H$_2$**C**H$_2$**O mPEG), 6.06 (s, 2H, ArH Rho6G), 6.26 (s, 2H, ArH Rho6G), 6.97 (d, 1H, ArH Rho6G), 7.50 (m, 2H, Ar**H** Rho6G), 7.77 (d, 1H, Ar**H** Rho6G), 1.86 (s, 6H, ArC**H$_3$**), 1.21 (t, 6H,NCH$_2$C**H$_3$**). mPEG-Rho123 conjugate ^{1}H NMR (600 MHz, DMSO-d_6) δ (ppm): 3.17 (s, 3H,C**H$_3$**O mPEG), 3.44 (s, 4H, C**H$_2$**C**H$_2$**O mPEG), 6.09 (s, 1H, Ar**H** Rho123), 6.10 (s, 1H, Ar**H** Rho123), 6.14 (d, 1H, Ar**H** Rho123), 6.16 (d, 1H, Ar**H** Rho123), 6.26 (d, 1H, Ar**H** Rho123), 7.43 (m, 4H, Ar**H** Rho123), 7.68 (d, 1H, Ar**H** Rho123). For diffusion ordered NMR of the mPEG-Rho6G conjugate and mPEG-NH_2 with free Rho6G, the gradient pulse was incremented in 12 steps and 16 steps, respectively. For the diffusion ordered NMR of the mPEG-Rho123 conjugate and mPEG-NH_2 with free Rho123, the gradient pulse was incremented in 16 steps and 12 steps, respectively. Stejskals-Tanner plots were made to represent the intensity decrease with increasing gradient. Points were included on the plots until the peaks had disappeared. The proposed structures of the resulting conjugates are shown in Figure 2.1 along with the structure of purchased mPEG-RhoB.

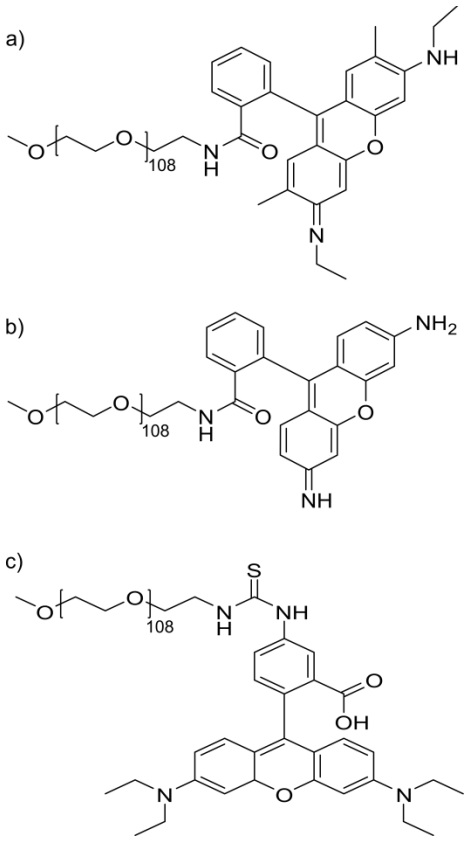

Figure 2.1 The proposed structure of a) mPEG-Rho6G conjugate, b) mPEG-Rho123 conjugate, and c) commercially available mPEG-RhoB

2.2.3 Purification of mPEG-RhoB. Purchased mPEG-RhoB was further purified by dissolving the purchased powder in MilliQ water and passing the sample through a series of PD-10 columns. In brief, the column was equilibrated with 25 mL of MilliQ water. After equilibration, 2.5 mL of a 6 mg/mL mPEG-RhoB solution was passed through the column followed by elution with 3.5 mL of MilliQ water. Eluent (3.5 mL) was collected and run through a second column that was also equilibrated with 25 mL of MilliQ water and eluted with 4.5 mL of MilliQ water. A clear separation of the high and low molecular weight components was observed in the second column and only the high molecular weight fraction was collected and lyophilized to dryness.

2.2.4 Cell culture. MDA-435/LCC6 MDR and MDA-435/LCC6 WT cells were maintained at 37 °C with 5% CO_2 in Richter's modified MEM (IMEM) containing L-glutamine, phenol red, 10% fetal bovine serum and 1% penicillin/streptomycin in 25 cm^2 canted T-flasks.

2.2.5 P-glycoprotein detection by Western blot. Total protein was extracted from $4x10^6$ of both MDA-435/LCC6 WT and MDA-435/LCC6 MDR cells by incubating in RIPA buffer (0.5 mL) with 1% protease inhibitor cocktail for 1 hour on ice. Cell lysate and any remaining debris were separated by centrifugation at 16,000xg for 2 min. Protein was quantified using the BCA protein assay. Cellular protein (50 µg) was separated on a 10% Bis-Tris NOVEX® gel with MOPS running buffer at a constant current of 80 mA. Proteins were transferred to a PVDF membrane at 300 mA for 45 minutes and then 350 mA for an additional 45 minutes. After blocking in non-fat milk, the membrane was incubated with a 1:5000 dilution of primary anti-P-glycoprotein antibody and 1:8000 dilution of primary anti-β-actin antibody for 1 hour followed by incubation for 30 minutes with a 1:3600 dilution of secondary anti-mouse antibody with alkaline phosphatase. The membrane was developed with BCIP blue liquid substrate.

2.2.6 P-glycoprotein interactions. MDA-435/LCC6 WT or MDA-435/LCC6 MDR cells ($1x10^6$ each) were detached from the culture flask surface with Accutase then incubated in suspension (in Accutase)

with 27 μM of either mPEG-Rho6G conjugate, mPEG-Rho123 or mPEG-RhoB or 0.27 μM of free Rho6G, free Rho123 or free RhoB for 1 hour at either 37 °C or 4 °C. For inhibition studies the cells were first incubated at 37 °C with 0, 5, 25, 50, 75, or 100 μM verapamil for 20 min then incubated with mPEG-Rho6G conjugate, mPEG-Rho123 conjugate, mPEG-RhoB conjugate, free Rho6G, free Rho123, or free RhoB for an additional hour at 37 °C. Inhibition studies evaluated with confocal imaging were conducted with 25 μM of verapamil since this was determined to be the lowest effective concentration from the FACS experiments. All studies were conducted with the cells gently suspended by rotation during the incubation time. After incubation the cells were centrifuged at 300xg for 10 min. The supernatant was removed and the cells were washed once with PBS. They were centrifuged again and resuspended in PBS with calcium and magnesium and placed on ice until FACS or confocal imaging analysis. The two centrifugation steps were included to allow time for efflux. FACS assays were performed on a BD LSR II FACS (San Jose, CA) machine equipped with a 488 nm laser and 100,000 cells were counted for each trial. Each experimental condition was conducted in triplicate. Data for mPEG-Rho6G conjugate, mPEG-Rho123, free Rho6G, and free Rho123 were collected under a FITC filter at a voltage of 300V. Data for mPEG-RhoB and free RhoB were collected under a PE filter at a voltage of 300V. FACS data were analyzed by gating all cell populations based on untreated cells. Imaging was performed on a Leica (Buffalo Grove, IL) SP2 confocal microscope with a 40x objective at 488 nm wavelength for fluorescent measurements of mPEG-Rho6G, mPEG-Rho123, free Rho6G and free Rho123. A 543nm wavelength was used for fluorescent measurements of mPEG-RhoB and free RhoB. For visual clarification images of cells incubated with RhoB and mPEG-Rho123 were adjusted for brightness by an equal amount for all images. Statistical significance was determined by Student's t-test with a *p*-value of <0.01 for all dyes and conjugates.

2.3 Results

2.3.1 Synthesis and characterization of mPEG-Rho123and mPEG-Rho6G. The conjugates of mPEG-Rho6G and mPEG-Rho123 were characterized by ^{1}H NMR (Figure 2.2 and Figure 2.3 respectively) and diffusion ordered NMR (Figure 2.4 and Figure 2.5 respectively). The single proton NMRs (Figure 2.2 and 2.3) show the respective Rho6G and Rho123 peaks visible from a chemical shift between 5 and 8 ppm (aromatic region). Percent conjugation yields were ~90% (of polymer chains that were initially NH_2 terminated), calculated from peaks at 3.17 (from mPEG), 1.25 ppm (from Rho6G), and 6.14 and 6.16 (from Rho123) ppm. To confirm that the ^{1}H NMR results were not from an unconjugated mixture of mPEG-NH_2 and free Rho6G or free Rho123 and that covalent conjugates were made, diffusion ordered NMR (which calculates relative diffusion of each peak in the spectra) was also performed (Figure 2.4 and 2.5). Small molecules, like free Rho6G or free Rho123, diffuse fast relative to macromolecules, like mPEG-NH_2. NMR signals with equal diffusion rates are indicative of covalently linked compounds. Diffusion ordered spectras of Rho6G with mPEG-NH_2 (Figure 2.4A), of conjugated mPEG-Rho6G (Figure 2.4B), of Rho123 with mPEG-NH_2 (Figure 2.5A) and of conjugated mPEG-Rho123 (Figure 2.5B) were obtained and represented by Stejskals-Tanner plots. The results show that Rho6G and Rho123 are covalently conjugated to the mPEG-NH_2 tether.

2.3.2 P-glycoprotein interactions. The interaction between the mPEG-Rho6G, mPEG-Rho123 and mPEG-RhoB conjugates and P-gp was investigated using two MDA-435/LCC6 cell lines; MDA-435/LCC6 MDR which expresses P-gp and MDA-435/LCC6 WT which does not.[28] Before tests were initiated, P-gp expression in both MDR and WT cells was confirmed by Western blot (Figure 2.6). The Western blot confirms the expression of P-gp in the MDR cells and the lack of expression in WT cells. The protein band in the MDR cells is visible around the molecular weight of P-gp, 170 kDa, which correlates to the reported molecular weight of the protein.[29]

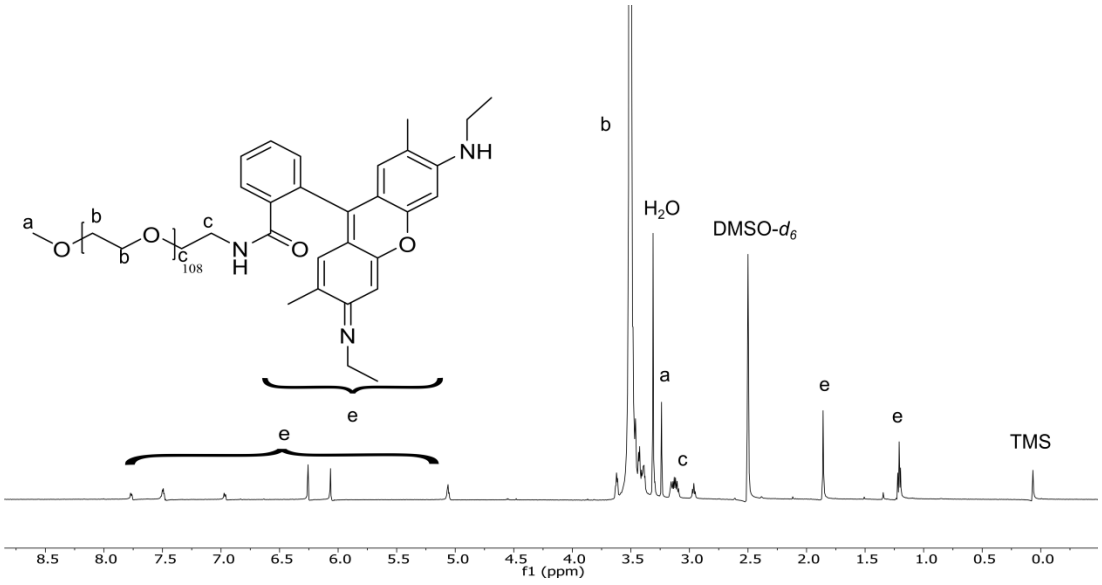

Figure 2.2 ^{1}H NMR of the mPEG-Rho6G conjugate in DMSO-*d6* at 600 MHz. Peaks in group e represent Rho6G while peaks at a and b are the peaks from mPEG.

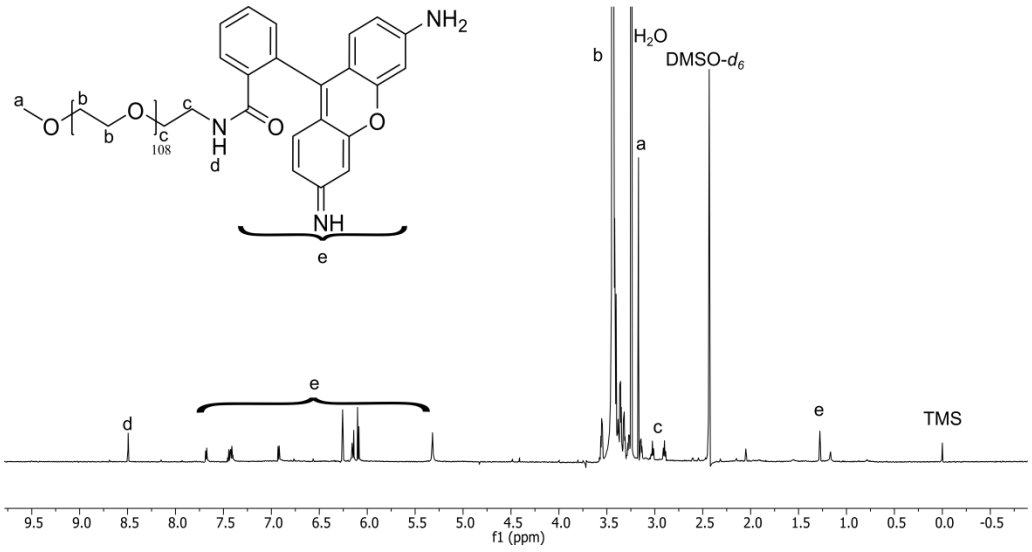

Figure 2.3 ^{1}H NMR of the mPEG-Rho123 conjugate in DMSO-*d6* at 600 MHz. Peaks in group e represent Rho123 while peaks at a and b are the peaks from mPEG. The peak at d represents the formed amide bond.

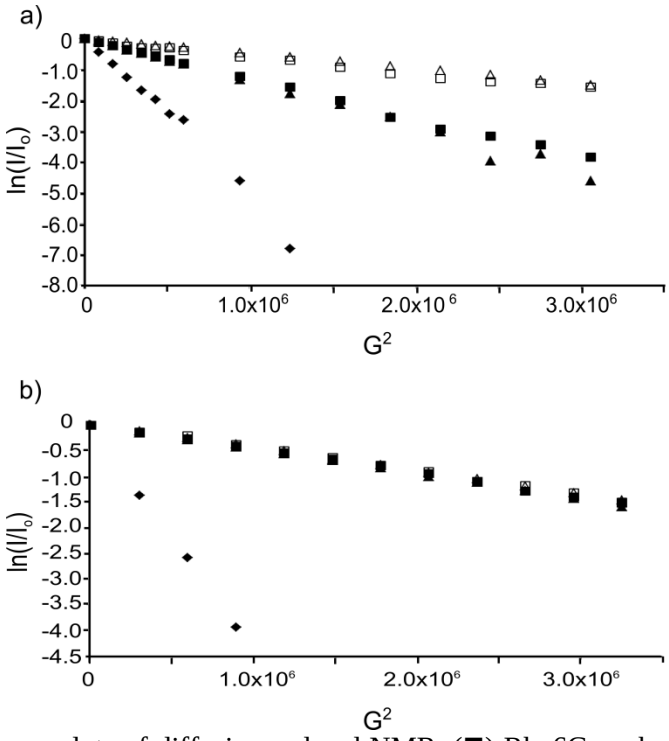

Figure 2.4 Stejskals-Tanner plots of diffusion ordered NMR. (■) Rho6G peak at 6.95 ppm, (▲) Rho6G peak 1.25 ppm, (□) mPEG peak at 3.17 ppm, (△) mPEG peak at 3.44 ppm, (◆) DMSO-d6 a) free Rho6G and unconjugated mPEG-NH2. Free Rho6G diffuses faster than mPEG-NH2. b) conjugated mPEG-Rho6G. Covalent attachment is evident from the equal diffusion of Rho6G peaks and mPEG peaks.

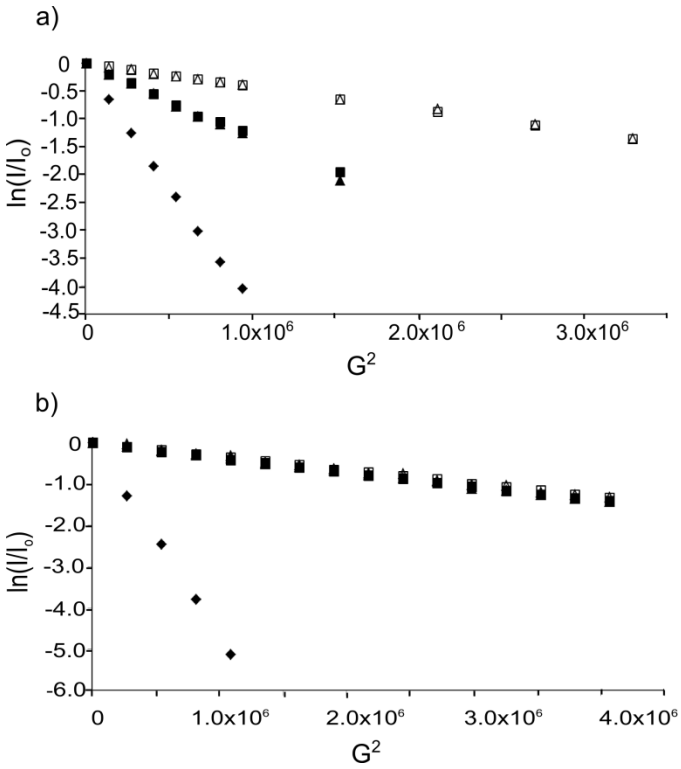

Figure 2.5 Stejskals-Tanner plots of diffusion ordered NMR. (■) Rho123 peaks at 6.14 and 6.16 ppm, (▲) Rho123 peaks at 6.09 and 6.10 ppm, (□) mPEG peak at 3.17 ppm, (△) mPEG peak at 3.44 ppm, (◆) DMSO-d6 a) free Rho123 and unconjugated mPEG-NH2. Free Rho123 diffuses faster than mPEG-NH2. b) conjugated mPEG-Rho123. Covalent attachment is evident from the equal diffusion of Rho123 peaks and mPEG peaks.

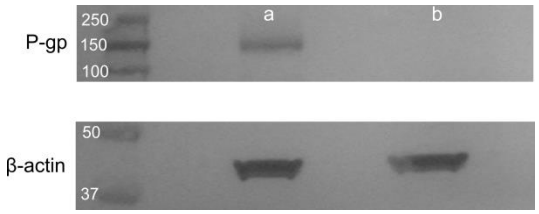

Figure 2.6 Western blot analysis to show P-gp expression in MDA-435/LCC6 MDR cells (a) and absence in MDA-435/LCC6 WT cells (b). First lane is a protein ladder for reference

Representative quantification of mPEG-Rho6G, mPEG-Rho123 and mPEG-RhoB accumulation in MDR and WT cells was obtained via FACS experiments and represented as a quantitated ratio between mean fluorescence of MDR cells compared to WT cells (Figure 2.7). Initial FACS experiments were conducted at 37 °C with 0 μM verapamil to investigate the efflux of both mPEG-dye conjugates and free dyes from MDR cells compared with WT cells. It was determined that 5.2 ± 0.3%, 26.2 ± 4 %, and 64.2 ± 6% of mPEG-Rho6G, mPEG-Rho123 and mPEG-RhoB, respectively, accumulated in MDR cells in comparison to WT cells. Native dyes showed that 3.3 ± 0.4%, 9.7 ± 0.6%, and 59.2 ± 4% of Rho6G, Rho123 and RhoB, respectively, accumulated in MDR cells in comparison to WT cells. To show that the mechanism of efflux was mediated by P-gp a series of verapamil (a well-established P-gp inhibitor[30]) concentrations (5, 25, 50, 75 and 100 μM) were added to the incubations. It was expected that an increase in inhibitor concentration would lead to an increase in accumulation in MDR cells. A concentration of 25 μM of verapamil increased MDR cell accumulation to 13.0 ± 1%, 59.8 ± 4%, and 93.6 ± 9% for mPEG-Rho6G, mPEG-Rho123, and mPEG-RhoB, respectively, and 28.5 ± 3%, 35.3 ± 2%, and 59.5 ± 9% for Rho6G, Rho123, and RhoB, respectively, compared to WT cells. FACS analysis was also performed with incubation at 4 °C to investigate endocytosis as mechanism of entry for mPEG-dye conjugates (Figure 2.8). Internalization of Rho6G, Rho123, and RhoB was decreased by 1.2 ± 0.06, 3.8 ± 0.3, and 1.2 ± 0.09 times in WT cells. Note that the y-axis for the RhoB experiment (Figure 2.8e) is smaller than the others in Figure 6. While these data appear to show that RhoB has lower overall cellular accumulation, the lower y-axis values of Figure 6e are due to the lower quantum efficiency of RhoB compared to Rho6G and Rho123.[31] Internalization of mPEG-Rho6G, mPEG-Rho123, and mPEG-RhoB was decreased by 2.9 ± 0.2, 6.4 ± 0.09, and 2.7 ± 0.3 times in WT cells. The greater decrease in mPEG-rhodamine conjugates signals endocytosis as an internalization mechanism. Statistics represent the significant differences in MDR/WT accumulation ratio at a *p*-value of <0.01. This implies that even though the conjugates undergo endocytosis, they can interact with P-gp which is important for future applications with targeted nanoparticles.

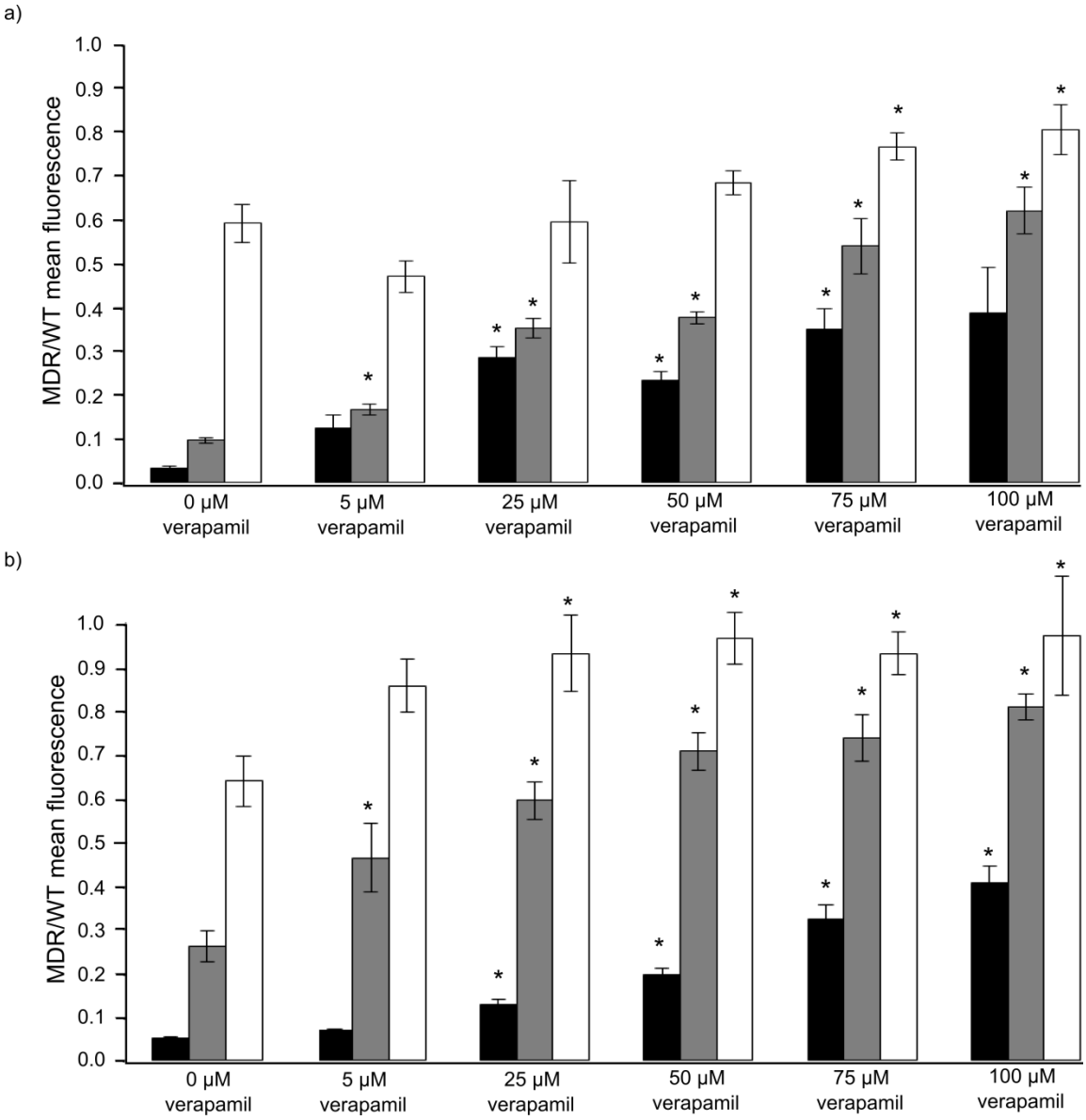

Figure 2.7 Representative accumulation ratio of MDR to WT cells of a) rhodamine alone and b) mPEG-rhodamine conjugates. Black bars represent Rho6G and mPEG-Rho6G, gray bars represent Rho123 and mPEG-Rho123, and white bars represent RhoB and mPEG-RhoB. Conjugates follow the same trends as the dyes alone with increasing verapamil concentrations. Also the pattern of high (Rho6G), medium (Rho123) and low (RhoB) P-gp affinity of the free dyes is maintained with conjugation of mPEG. All bars are an average of 3 replicates.

* Represents statistical significance of $p<0.01$ over 0 μM verapamil condition

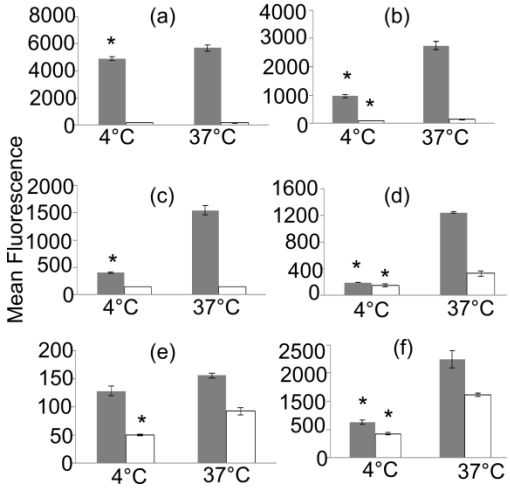

Figure 2.8 FACS analysis comparing accumulation of a) Rho6G, b) mPEG-Rho6G, c) Rho123, d) mPEG-Rho123, e) RhoB, f) mPEG-RhoB at 4°C to accumulation at 37°C. Gray bars represent accumulation in WT cells and white bars represent accumulation in MDR cells. Conjugates have a greater change in accumulation than native dyes with the temperature change signifying endocytosis as an internalization mechanism.

* Represents statistical significance of $p<0.01$

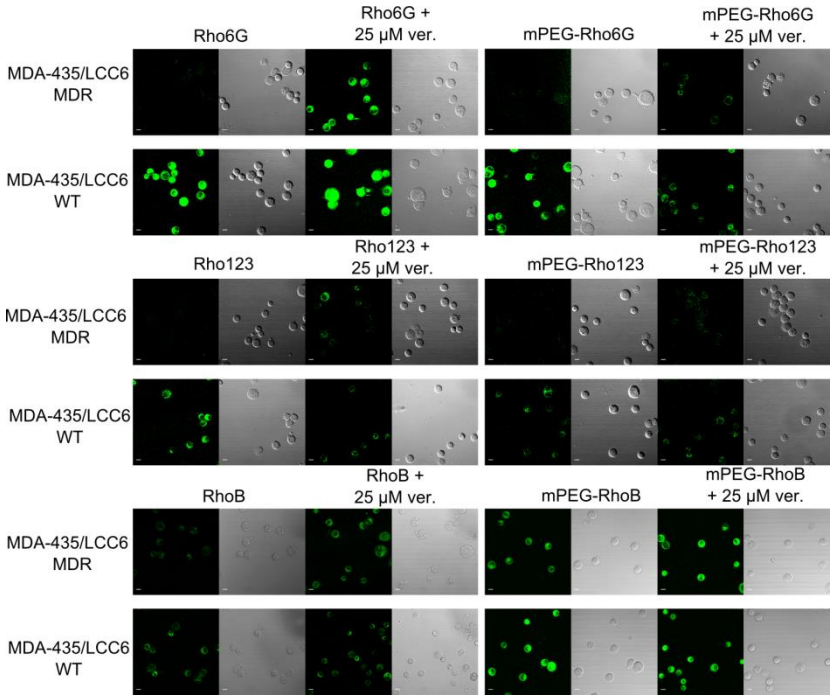

Figure 2.9 Confocal images of MDR and WT cells incubated with either mPEG-Rho123, mPEG-Rho6G, mPEG-RhoB, Rho123, Rho6G or RhoB. Cells were incubated with 0 μM or 25 μM verapamil both at 37 °C. Fluorescent accumulation is greater in WT cells for all conditions at 0 μM verapamil. At 25 μM verapamil fluorescent accumulation is similar for both MDR and WT cells for all conditions. These results are consistent with FACS analysis.

Visual verification of the FACS results was obtained by confocal microscopy of cells incubated with both mPEG-dye conjugates and free dyes (Figure 2.9). Images were taken of mPEG-dye conjugates and free dyes incubated with MDR and WT cells at 37 °C with 0 μM of verapamil P-gp inhibitor. Images were also obtained from identical incubations conducted in the presence of 25 μM of verapamil to observe the increase in accumulation of mPEG-dye conjugates and free dyes. All images visually verify the FACS results.

2.4 Discussion

Rhodamine dyes are a class of well characterized P-gp substrates and have been utilized for numerous P-gp analysis studies. This study investigated the synthesis and P-gp mediated efflux patterns of a macromolecular conjugates composed of mPEG linked through the 2' position of Rho6G and Rho123 in comparison to the patterns of free Rho6G and free Rho123. This study also compared P-gp mediated efflux patterns of commercially available mPEG-RhoB in comparison to patterns of free RhoB. Conjugate synthesis was confirmed by ^{1}H NMR and diffusion ordered ^{1}H NMR. Both the mPEG and Rho6G or Rho123 peaks are present and identifiable on the ^{1}H spectra and the diffusion ordered NMR confirmed covalent conjugation. When free Rho6G or Rho123 is physically mixed with unconjugated mPEG-NH_2 the decrease in peak intensity in the diffusion ordered NMR is much faster for Rho6G or Rho123 peaks than for mPEG-NH_2 peaks, which translates into very different diffusion rates and depicts a lack of covalent attachment. However, once Rho6G or Rho123 is conjugated to the mPEG, the decrease in intensity is the same for both the Rho6G or Rho123 and mPEG peaks, which depicts covalent attachment of the compounds. The behavior of faster decay for smaller molecules seen on the Stejskals-Tanner plots is a consistent result given the size of the molecules involved; the smaller the molecule, the faster the signal decays with increasing gradient.[32–34]

FACS experiments were performed to analyze efflux patterns of mPEG-Rho6G, mPEG-Rho123, and mPEG-RhoB and compare them with patterns of Rho6G, Rho123 and RhoB. The two wash steps allowed for measurements of efflux separate from any variances in influx. Results with 0 μM

verapamil exhibit the pattern of Rho6G, Rho123 and RhoB acting as "high", "medium" and "low" P-gp substrates respectively with correspondence to efflux patterns. This same pattern is followed by the mPEG conjugates where mPEG-RhoB has the highest accumulation in MDR cells compared to WT cells, mPEG-Rho123 has moderate accumulation and mPEG-Rho6G has low accumulation. Studies in the literature involving Rho6G, Rho123 and RhoB report the same trend reported here.[16,17] Confirmation of P-gp mediated efflux of the mPEG-rhodamine conjugates was accomplished by serial increases in the concentration of verapamil. Verapamil is a well-established inhibitor of P-gp that increases intracellular accumulation of free Rho6G, free Rho123 and free RhoB in a concentration dependent manner. Higher concentrations of verapamil lead to higher accumulation of Rho6G[35,36], Rho123[37,38], and RhoB[39] in MDR cell lines. Our results show that higher concentrations of verapamil increase accumulation of all dyes and conjugates in MDR cells. Rho6G has significant increases in MDR/WT accumulation ratio above 25 μM of verapamil. At 100 μM of verapamil there is a large variance in accumulation ratio leading to an insignificant result compared to 0 μM. This is likely due to variability in P-gp expression between cells in the MDR cell line and the strength of Rho6G as a P-gp substrate. The mPEG-Rho6G conjugate has a significant increase in accumulation ratio at all verapamil concentrations and still remains a strong P-gp substrate. Both Rho123 and mPEG-Rho123 have significant increases in MDR/WT accumulation ratio with as little as 5 μM of verapamil and are moderately effluxed by P-gp. RhoB does not show significant increases until 75 μM of verapamil and mPEG-RhoB shows an accumulation ratio close to 1 after 25 μM of verapamil, signaling both are less effective P-gp substrates. Polymer conjugates of P-gp substrates have previously been reported for doxorubicin.[40] These conjugates were designed to and allowed escape from P-gp mediated efflux by covalently attaching polymers at the amine site on doxorubicin which is essential for P-gp binding.[41] However, for the mPEG-substrates reported in this study, the amine groups on the substrates are preserved allowing for the conjugates to remain P-gp substrates.

FACS analysis was also performed following 4 °C incubation. mPEG-Rho6G, mPEG-Rho123 and mPEG-RhoB all show significant decreases in accumulation in both MDR and WT cells suggesting endocytosis as mechanism of cell entry, a well-characterized internalization mechanism for

macromolecules[13,42–44]. The conjugates are still able to interact with P-gp during endocytosis as P-gp has been shown to retain activity.[45] Rho6G and Rho123 show significant decreases in accumulation for WT cells but not for MDR cells due to efficient efflux at 37 °C. The decrease in Rho6G is much less than in mPEG-Rho6G due to the difference in passive diffusion versus endocytosis. Rho123 and mPEG-Rho123 have similar decreases in WT accumulation due to the fact that Rho123 shows little accumulation in non-MDR cell lines.[46] RhoB has a significant decrease in both WT and MDR cell lines since P-gp mediated efflux for this substrate at 37 °C is poor.

Confocal images were taken to visualize the FACS results at 0 μM and 25 μM verapamil. Fluorescence is visible in all WT cell lines for all conditions. In all cases when 25 μM verapamil is introduced fluorescence is similar in MDR cells lines as in WT cell lines.

2.5 Conclusion

Strategies to investigate MDR-expressing cancerous tumors can greatly benefit from macromolecuar P-gp substrates. This study demonstrates that conjugation of Rho6G and Rho123 through the 2' position to mPEG produces conjugates that can still be classified as P-gp substrates. FACS analysis was used to determine the efflux patterns of mPEG-Rho6G, mPEG-Rho123 and commercially available mPEG-RhoB conjugates in MDA-435/LCC6 MDR and MDA-435/LCC6 WT cells. Confocal imaging provided visual verification of FACS data. The knowledge that Rho conjugates still act as a P-gp substrates makes rhodamine dyes a reasonable choice as a tethered system for further analysis of P-gp interactions *in vitro* and *in vivo*.

REFERENCES

(1) Eckford, P. D. W., and Sharom, F. J. (2009) ABC efflux pump-based resistance to chemotherapy drugs. *Chem. Rev. 109*, 2989–3011.

(2) Szakács, G., Paterson, J. K., Ludwig, J. a, Booth-Genthe, C., and Gottesman, M. M. (2006) Targeting multidrug resistance in cancer. *Nat. Rev. 5*, 219–234.

(3) Borst, P., Evers, R., Kool, M., and Wijnholds, J. (2000) A Family of Drug Transporters: the Multidrug Resistance-Associated Proteins. *J. Natl. Cancer Inst. 92*, 1295–1302.

(4) Aller, S. G., Yu, J., Ward, A., Weng, Y., Chittaboina, S., Zhuo, R., Harrell, P. M., Trinh, Y. T., Zhang, Q., Urbatsch, I. L., and Chang, G. (2009) Structure of P-glycoprotein reveals a molecular basis for poly-specific drug binding. *Science 323*, 1718–1722.

(5) Kim, R. B. (2002) Drugs as P-glycoprotein substrates, inhibitors, and inducers. *Drug Metab. Rev. 34*, 47–54.

(6) Matsuo, H., Wakasugi, M., Takanaga, H., Ohtani, H., Naito, M., Tsuruo, T., and Sawada, Y. (2001) Possibility of the reversal of multidrug resistance and the avoidance of side effects by liposomes modified with MRK-16, a monoclonal antibody to P-glycoprotein. *J. Control. Release 77*, 77–86.

(7) Iwahashi, T., Okochi, E., Ariyoshi, K., Watabe, H., and Aã-na, E. (1993) Specific Targeting and Killing Activities of Anti-P-Glycoprotein Monoclonal Antibody MRK16 Directed against Intrinsically Multidrug-resistant Human Colorectal Carcinoma Cell Lines in the Nude Mouse Model Specific Targeting and Killing Activities of Anti-P. *Cancer Res. 53*, 5475–5482.

(8) Thomas, H., and Coley, H. M. (2003) Overcoming multidrug resistance in cancer: an update on the clinical strategy of inhibiting p-glycoprotein. *Cancer Control 10*, 159–165.

(9) Pires, M. M., Hrycyna, C. a, and Chmielewski, J. (2006) Bivalent probes of the human multidrug transporter P-glycoprotein. *Biochemistry 45*, 11695–11702.

(10) Pires, M. M., Emmert, D., Hrycyna, C. A., and Chmielewski, J. (2009) Inhibition of P-Glycoprotein-Mediated Paclitaxel Resistance by Reversibly Linked Quinine Homodimers. *Mol. Pharmacol. 75*, 92–100.

(11) Kang, J. S., Deluca, P. P., and Lee, K. C. (2009) Emerging PEGylated drugs. *Expert Opin. Emerg. Drugs 14*, 363–380.

(12) Greenwald, R. B. (2001) PEG drugs: an overview. *J. Control. Release 74*, 159–171.

(13) Werle, M. (2008) Natural and synthetic polymers as inhibitors of drug efflux pumps. *Pharm. Res. 25*, 500–511.

(14) Kabanov, A. V, Batrakova, E. V, and Alakhov, V. Y. (2002) Pluronic block copolymers as novel polymer therapeutics for drug and gene delivery. *J. Control. Release 82*, 189–212.

(15) Batrakova, E. V, Li, S., Vinogradov, S. V, Alakhov, V. Y., Miller, D. W., and Kabanov, a V. (2001) Mechanism of pluronic effect on P-glycoprotein efflux system in blood-brain barrier: contributions of energy depletion and membrane fluidization. *J. Pharmacol. Exp. Ther. 299*, 483–93.

(16) Eytan, G. D., Regev, R., Oren, G., Hurwitz, C. D., and Assaraf, Y. (1997) Efficiency of P-glycoprotein-mediated exclusion of rhodamine dyes from multidrug-resistant cells is determined by their passive transmembrane movement rate. *Eur. J. Biochem. 248*, 104–112.

(17) Loetchutinat, C., Saengkhae, C., Marbeuf-Gueye, C., and Garnier-Suillerot, A. (2003) New insights into the P-glycoprotein-mediated effluxes of rhodamines. *Eur. J. Biochem. 270*, 476–485.

(18) Nare, B., Prichard, R. K., and Georges, E. (1994) Characterization of rhodamine 123 binding to P-glycoprotein in human multidrug-resistant cells. *Mol. Pharmacol. 45*, 1145–1152.

(19) Störmer, E., von Moltke, L. L., Perloff, M. D., and Greenblatt, D. J. (2002) Differential modulation of P-glycoprotein expression and activity by non-nucleoside HIV-1 reverse transcriptase inhibitors in cell culture. *Pharm. Res. 19*, 1038–1045.

(20) Tian, R., Koyabu, N., Takanaga, H., Matsuo, H., Ohtani, H., and Sawada, Y. (2002) Effects of grapefruit juice and orange juice on the intestinal efflux of P-glycoprotein substrates. *Pharm. Res. 19*, 802–809.

(21) Fröhlich, M., Albermann, N., Sauer, A., Walter-Sack, I., Haefeli, W. E., and Weiss, J. (2004) In vitro and ex vivo evidence for modulation of P-glycoprotein activity by progestins. *Biochem. Pharmacol. 68*, 2409–2416.

(22) Lee, J. S., Paull, K., Alvarez, M., Hose, C., Monks, A., Grever, M., Fojo, a T., and Bates, S. E. (1994) Rhodamine efflux patterns predict P-glycoprotein substrates in the National Cancer Institute drug screen. *Mol. Pharmacol. 46*, 627–638.

(23) Dujols, V., Ford, F., and Czarnik, A. W. (1997) A Long-Wavelength Fluorescent Chemodosimeter Selective for Cu(II) Ion in Water. *J. Am. Chem. Soc. 119*, 7386–7387.

(24) Knauer, K.-H., and Gleiter, R. (1977) Photochromism of Rhodamine Derivatives. *Angew. Chem. Int. 16*, 113.

(25) Adamczyk, M., and Grote, J. (2000) Efficient synthesis of rhodamine conjugates through the 2'-position. *Bioorg. Med. Chem. Lett. 10*, 1539–1541.

(26) Veronese, F. M., and Pasut, G. (2005) PEGylation , successful approach to drug delivery. *Drug Discov. Today 10*, 1451–1458.

(27) Gombar, V. K., Polli, J. W., Humphreys, J. E., Wring, S. a, and Serabjit-Singh, C. S. (2004) Predicting P-glycoprotein substrates by a quantitative structure-activity relationship model. *J. Pharm. Sci. 93*, 957–968.

(28) Leonessal, F., Green, D., Licht, T., Wright, A., Lippman, J., and Clarke, R. (1996) MDR : ascites models of human breast cancer. *Br. J. Cancer 161*, 154–161.

(29) Riordan, J. R., and Ling, V. (1979) Purification of P-glycoprotein from plasma membrane vesicles of Chinese hamster ovary cell mutants with reduced colchicine permeability. *J. Biol. Chem. 254*, 12701–12705.

(30) Tsuruo, T., Iida, H., Yamashiro, M., Tsukagoshi, S., and Sakurai, Y. (1982) Enhancement of vincristine- and adriamycin-induced cytotoxicity by verapamil in P388 leukemia and its sublines resistant to vincristine and adriamycin. *Biochem. Pharmacol. 31*, 3138–3140.

(31) Kubin, R. F., and Fletcher, A. N. (1982) Fluorescence Quantum Yields of Some Rhodamine Dyes. *J. Lumin. 27*, 455–462.

(32) Johnson Jr., C. (1999) Diffusion ordered nuclear magnetic resonance spectroscopy: principles and applications. *Prog. Nucl. Magn. Reson. Spectrosc. 34*, 203–256.

(33) Momot, K. I., and Kuchel, P. W. (2003) Pulsed field gradient nuclear magnetic resonance as a tool for studying drug delivery systems. *Concepts Magn. Reson. 19A*, 51–64.

(34) Kaucher, M. S., Lam, Y.-F., Pieraccini, S., Gottarelli, G., and Davis, J. T. (2004) Using diffusion NMR to characterize guanosine self-association: insights into structure and mechanism. *Chemistry 11*, 164–173.

(35) Matsumoto, Y., Sasaoka, N., Tsuchida, T., Fujiwara, T., Nagao, S., and Ohmoto, T. (1992) Fluorescent dye rhodamine 6G as a molecular probe to study drug resistance of C6 rat glioma cells. *J. Neurooncol. 13*, 217–222.

(36) Mihályi, A., Gáspár, R., Zalán, Z., Lázár, L., Fülöp, F., and de Witte, P. a M. (2004) Synthesis and multidrug resistance reversal activity of 1,2-disubstituted tetrahydroisoquinoline derivatives. *Anticancer Res. 24*, 1631–1636.

(37) Aguero, B., Saxton, R. E., and Castro, D. J. (1994) Verapamil Increases Rhodamine 123 Laser Phototherapy of Drug-Resistant Human Sarcoma Cells. *J. Clin. Laser Med. Surg. 12*, 193–198.

(38) Yumoto, R., Murakami, T., Nakamoto, Y., Hasegawa, R., Nagai, J., and Takano, M. (1999) Transport of rhodamine 123, a P-glycoprotein substrate, across rat intestine and Caco-2 cell monolayers in the presence of cytochrome P-450 3A-related compounds. *J. Pharmacol. Exp. Ther. 289*, 149–155.

(39) Tutundjian, R., Minier, C., Le Foll, F., and Leboulenger, F. (2002) Rhodamine exclusion activity in primary cultured turbot (*Scophthalmus maximus*) hepatocytes. *Mar. Environ. Res. 54*, 443–447.

(40) Minko, T., Kopecková, P., and Kopecek, J. (1999) Comparision of the Anticancer Effect of Free and HPMA Copolymer-Bound Adriamycin in Human Ovarian Carcinoma Cells. *Pharm. Res. 16*, 986–996.

(41) Priebe, W., and Perez-Soler, R. (1993) Design and tumor targeting of anthracyclines able to overcome multidrug resistance: a double-advantage approach. *Pharmacol. Ther. 60*, 215–234.

(42) Kopecek, J., Kopecková, P., Minko, T., Lu, Z. R., and Peterson, C. M. (2001) Water soluble polymers in tumor targeted delivery. *J. Control. Release 74*, 147–58.

(43) Kopecek, J., Kopecková, P., Minko, T., and Lu, Z. (2000) HPMA copolymer-anticancer drug conjugates: design, activity, and mechanism of action. *Eur. J. Pharm. Biopharm. 50*, 61–81.

(44) Duve, C. De, Barsy, T. De, Poole, B., Trouet, A., Tulkens, P., and Van Hoof, F. (1974) Lysosomotropic Agents. *Biochem. Pharmacol. 23*, 2495–2531.

(45) Fu, D., and Arias, I. M. (2012) Intracellular trafficking of P-glycoprotein. *Int. J. Biochem. Cell Biol. 44*, 461–464.

(46) Sarver, J. G., Klis, W. a., Byers, J. P., and Erhardt, P. W. (2002) Microplate Screening of the Differential Effects of Test Agents on Hoechst 33342, Rhodamine 123, and Rhodamine 6G Accumulation in Breast Cancer Cells that Overexpress P-Glycoprotein. *J. Biomol. Screen. 7*, 29–34.

CHAPTER 3

A SIMPLE AND SENSITIVE METHOD TO QUANTIFY BIODEGRADABLE NANOPARTICLE BIODISTRIBUTION USING EUROPIUM CHELATES

(Contributors: Jaclyn Higgins)

3.1 Introduction

Biodegradable nanoparticles (NPs), such as those derived from diblock copolymers of polylactic acid and polyethylene glycol (PLA-PEG), are valuable in the field of targeted drug delivery. The hydrophobic PLA core can entrap hydrophobic compounds to serve as a carrier for medicines that can be difficult to deliver intravenously.[1,2]

An important step in the development of PLA-PEG NP drug delivery systems is their detection following injection in the blood stream. Common methods to detect the biodistribution of NPs include radiolabels and fluorescent markers. Fluorescence is a safer alternative to radiolabeling; however, the autofluorescence of biological tissues makes it challenging.[3,4] Specifically, amino acids in biological tissues contribute to autofluorescent signals by absorbing and emitting light at frequencies that overlap with those of common fluorescent markers.[5] Therefore, the level of detection and the signal to noise ratios of common fluorescent markers is compromised leading to decreased sensitivity.[6–8] Another approach to the detection of NPs in tissues is to use markers that absorb and emit light in the longer wavelength near-infrared spectrum to minimize autofluorescence; however, these compounds are prone to degradation and photobleaching.[9]

As an alternative strategy to overcome autofluorescence in the detection of structures in biological tissues, time resolved fluorescence (TRF) has been explored. Elements in the lanthanide III series exhibit TRF. Their large Stokes shifts and long decay lifetimes allow them to be detected distinct from competing autofluorescence signals.[10] They are also less susceptible to photobleaching than traditional organic dyes.[11–13] Earlier reports have described the utility of lanthanide chelates for the detection of non-

degradable NPs both *in vivo* and *ex vivo*, but degradable NPs, like those based on PLA-PEG, have unreported characteristics that makes their detection unique and should be considered to accurately quantify their concentration in tissues.[14–16]

This chapter outlines a simple approach to the detection and quantitation of PLA-PEG NPs in tissues following intravenous injection. A hydrophobic europium chelate was encapsulated within the PLA-PEG core. The TRF of the europium-doped NPs is significantly above tissue autofluorescence, and the particles are detectable in harvested organs *ex vivo* with minimal post-processing of the tissues.

Two important characteristics of the encapsulated europium were identified when quantifying NPs in tissues. First, the TRF of europium diminishes as a second-order function upon exposure to water. Europium chelate located toward the outer surface of the particle is susceptible to water penetration along the same time scale as the biodistribution studies; therefore, the rate of signal decrease upon water exposure is an important parameter in the biodistribution calculations. Second, the TRF of europium is compromised by iron ions; therefore, the signal must be corrected for each tissue using doped tissue blanks. The described method was used to assess the biodistribution of the widely used PLA-PEG-based NP drug delivery system.

3.2 Materials and Methods

3.2.1 Materials. Monomethoxy polyethylene glycol (PEG, M_n 5000), anhydrous toluene, stannous octoate, europium chloride hexahydrate, 4,4,4-trifluoro-1-(2-naphthyl-1,3-butanedione) (NTA), acetone, dichloromethane (DCM), magnesium sulfate, poloxamer 188 solution and RIPA buffer were purchased from Sigma Aldrich (Saint Louis, MO). D,L-Lactide was purchased from TCI America (Portland, OR). Phosphate buffered saline (PBS) was purchased from Corning (Corning, NY). Ammonium hydroxide was purchased from Alpha Aesar (Ward Hill, MA). Diethyl ether was purchased from Fisher Chemicals (Waltham, MA). Methanol was purchased from Macron Fine Chemicals (Avantor Performance Materials,

Center Valley, PA). Horse plasma was graciously donated by the Cornell College of Veterinary Medicine.

3.2.2 PEG azeotropic distillation. Monomethoxy PEG (50 g, M_n 5000) was dissolved in 200 mL of anhydrous toluene with slight heating. Distillation was carried out under reflux at 128 °C for 2 hours using a Dean Stark trap. The remaining toluene was removed by rotoevaporation and the PEG product dried under high vacuum.

3.2.3 PLA-PEG diblock copolymer synthesis and characterization. Lactide was recrystallized once from methanol and dried under high vacuum prior to the reaction. PEG (400 mg, 0.08 mmol) and lactide (1843 mg, 12.8 mmol) were dissolved in anhydrous toluene (6 mL) under argon in a 25 mL Schlenk flask. The reaction vessel was placed in a 111 °C mineral oil bath. Upon the initiation of toluene reflux (111 °C), toluene (2 mL) containing stannous octoate (0.14 mmol) was added all at once with stirring. The reaction was allowed to reflux with stirring over 24 hours, after which excess toluene was removed by rotoevaporation until an oily liquid remained and the product collected by precipitation into excess diethyl ether with stirring. The product was collected by filtration, dried overnight under high vacuum and stored at room temperature in a vacuum dessicator until characterization and nanoparticle production. The molecular weight of the diblock copolymer was determined using both GPC (polystyrene standards) and ^{1}H NMR. ^{1}H NMR was used to confirm PLA-PEG structure ppm: 5.20 (m, CH PLA), 3.51 (s,CH_2CH_2 PEG), 3.24 (s, CH_3 PEG), 1.45 (m, CH_3 PLA).

3.2.4 Europium(III)tris(4,4,4-trifluoro-1-(2-naphthyl-1,3-butanedione)) chelate synthesis. The europium(III)tris(4,4,4-trifluoro-1-(2-naphthyl-1,3-butanedione)) ($Eu(NTA)_3$) chelate was synthesized as previously reported.[17] In brief, NTA (800 mg) was dissolved in 75 mL of ethanol (75 mL) and ammonium hydroxide (20.4 mL of 28%) with stirring. On complete dissolution, a solution of 366 mg of europium chloride hexahydrate (366 mg) in DI water (10 mL) was added dropwise to the NTA solution. The

chelate was allowed to form overnight by ethanol evaporation with stirring at room temperature. The resulting solution was then extracted with DCM, the organic layer was then isolated and washed with DI water three times. The DCM solution was dried over magnesium sulfate, removed by rotoevaporation, and the resulting solid was dried under high vacuum.

3.2.5 Nanoparticle fabrication and characterization. PLA-PEG (200 mg) was dissolved in DCM (2 mL) then vortexed with a DCM solution of $Eu(NTA)_3$ (1 mg/mL, 2 mL total). The solution was then diluted with acetone (16 mL), vortexed and added dropwise into milliQ water (20 mL) with stirring. The organic solvents were removed by rotoevaporation and the nanoparticles collected by ultracentrifugation using a Bruker LE-80 ultracentrifuge at 20,000 rpm for 30 minutes. The nanoparticles in the pellet were washed twice with milliQ water and resuspended in a final volume of 1 mL of milliQ water. Poloxamer 188 (40 μL of 10% solution) was added prior to lyophilization overnight.

For nanoparticle characterization, a particle suspension (1 mg/mL) in PBS was sonicated in a VWR B1500A-MTH (Radnor, PA) bath sonicator for 30 minutes and flowed through a 0.45 μm filter before analysis. Size and polydispersity were measured with a Malvern NanoZS (United Kingdom). Excitation and emission spectra for the nanoparticles were taken on a SpectraMax GeminiEM fluorescent plate reader (Molecular Devices, Sunnyvale, CA) under time resolved conditions (start time 250 μs, end time 1450 μs) using a white 96 well plate and compared to excitation and emission spectra of 0.1 mg/mL solution of the chelate alone in acetone.

The decrease in TRF of the nanoparticles was determined in horse plasma. A nanoparticle stock suspension (1 mg/mL in PBS) was sonicated for 30 min. (to parallel the biodistribution studies), flowed through a 0.45 μm filter, then diluted to 0.1 mg/mL with fresh horse plasma that was obtained from heparinized horse blood. The particles in plasma were incubated at 37 °C and TRF was measured at 0.5, 1, 2, 3, 6 and 9 hours in triplicate. The data was transformed into a plot of inverse fluorescence decrease

vs. time which was fit with a straight line. The straight line fit was then used to calculate the decrease in fluorescent signal for any time.

Release of europium chelate from the particles was also determined. A 1 mg/mL solution of nanoparticles in PBS was sonicated for 30 minutes. 10,000 MWCO Slide-A-Lyzer™ devices were soaked in 1.25 mL PBS in 1.75 mL Eppendorf tubes. Once the nanoparticles were sonicated, they were filtered through a 0.45 µm membrane and 200 µL of particle suspension was added to each dialysis chamber. The capped chambers were shaken at 37 °C and at 0, 0.5, 3, 6 and 9 hours the time resolved fluorescence was measured in the bottom solution to determine amount of chelate released. Each time point was done in triplicate.

3.2.6 Nanoparticle sensitivity. The sensitivity of detection above tissue autofluorescence of the europium chelate doped NPs were tested against rhodamine B doped NPs produced by the same procedure. A solution (1 mg/mL) of NPs was suspended in PBS and sonicated for 30 minutes, flowed through a 0.45 µm filter and diluted to 0.1, 0.05, 0.01, 0.001, 0.0001 mg/mL with mouse liver homogenate. Liver homogenate was used as a representative tissue since it has the highest autofluorescence and greatest interference. The europium chelate doped NP dilutions were read under the time resolved conditions mentioned previously. Rhodamine B doped NP dilutions were read at excitation and emission wavelengths of 540 and 625 nm, respectively. The fluorescent values were plotted on a logarithmic scale along with a dotted line representing sensitivity of detection. Sensitivity of detection was defined as the average value of autofluorescence plus 3 standard deviations. Experiments were performed in triplicate. To compare the sensitivity as it relates to encapsulated fluorophore, encapsulation efficiency was calculated for both europium chelate doped NPs and RhoB doped NPs. The fluorescence of a 1 mg/mL solution of fluorophore containing NPs in acetone was compared to the fluorescence of a 0.01 mg/mL solution of free fluorophore in acetone. The encapsulation efficiency was then used to calculated the corresponding fluorophore concentration used in the sensitivity analysis. Statistical significance was determined using a Student's t-test at a significance level of $p < 0.01$.

3.2.7 In vivo biodistribution. Seven week old ND4 Swiss Webster mice were purchased from Harlan Sprague Dawley. A suspension of nanoparticles (1 mg/mL) in sterile PBS was sonicated for 30 minutes and then flowed through a 0.45 μm filter. A 200 μL aliquot of the nanoparticle suspension was injected intravenously through the tail vein. At 0.5, 3, 6 and 9 hours, five mice were euthanized by CO_2 inhalation under an approved IACUC protocol (Cornell University, protocol number 2012-0034). Blood was drawn via cardiac puncture and their liver, kidney, heart, lung, spleen and brain removed. Each organ was weighed, homogenized in 2 mL of RIPA buffer and the resulting mixtures were centrifuged at 800 x g for 10 minutes. Time-resolved fluorescence was measured in three separate samples of the homogenate supernatant for each of the five mice per organ. Percent injected dose was determined by subtracting previously recorded blank readings for each organ type. This value was then divided by the TRF of injected nanoparticles along with the interference factor. The interference factor was determined by doping 20 μL of nanoparticle suspension in PBS into 180 μL of various untreated tissue homogenates. The solutions were read under time resolved conditions and the tissue value was adjusted according to Equation 2. The sensitivity limit (autofluorescent value + 3 standard deviations) was subtracted from the raw data. This value was then divided by the control of nanoparticles in PBS alone and the interference factor. The final adjustment was made by multiplying the time factor obtained from the second order equation. The variables in the equation are: RD= raw data, SL= sensitivity limit, ID= injected dose, IF= interference factor, g tissue = gram of tissue and TF= time factor. Time factor was calculated by plugging in the appropriate time value into the straight line fit of the inverse fluorescent decrease vs. time graph (Equation 1). Area under the curve from 30 minutes to 9 hours was calculated by the trapezoid rule.

$$TF = 1.5043 * t + 1.3909 \quad \text{(Eq. 1)}$$

$$\left[\frac{(RD-SL)}{ID*IF*g\ tissue} * TF\right] * 100 = \frac{\%\ injected\ dose}{g\ tissue} \quad \text{(Eq. 2)}$$

3.3 Results

3.3.1 Nanoparticle fabrication and characterization. Polylactic acid–mono methoxy polyethylene glycol (PLA-PEG) diblock copolymers were synthesized by ring opening polymerization. M_n was consistent between both GPC and ^{1}H NMR (21,000 and 20,600, respectively). Nanoparticle fabrication yielded particles 106 ± 6.5 nm in diameter and -1.45 ± 0.25 mV surface charge with a polydispersity of 0.079 ± 0.03. Excitation and emission spectra for the particles and chelate (Figure 3.1), show maximum excitation at 340 nm and a maximum emission at 610 nm. Both the unencapsulated chelate and the chelate-containing nanoparticles show a large Stokes shift, which is a hallmark characteristic of europium chelates. Release studies of europium chelate from PLA-PEG nanoparticles (Figure 3.2) show no detectable chelate is released over nine hours.

3.3.2 Sensitivity Analysis. The sensitivity limit of the $Eu(NTA)_3$ doped PLA-PEG NPs was determined and compared to RhoB loaded PLA-PEG NPs (Figure 3.3). Encapsulation efficiencies were determined to be 87.0 ± 14 % and 7.82 ± 1.7 % for europium chelate and RhoB doped nanoparticles, respectively. Using the encapsulation efficiency, the europium doped NPs were detectable at as little as 8.7×10^{-6} mg/mL of europium chelate above the sensitivity limit compared to 3.9×10^{-5} mg/mL of RhoB for RhoB doped particles. This is an almost 5x increase in sensitivity using europium chelate doped nanoparticles over RhoB.

3.3.3 Europium signal degradation kinetics. The TRF signal of europium chelates is diminished on exposure to water.[18] To account for signal changes in the context of quantifying biodistribution, the TRF of europium-doped NPs was measured in plasma (Figure 3.4). The signal decay was transformed into a linear form that signified a second-order process. A straight line fit provided an equation to assess signal degradation at any time.

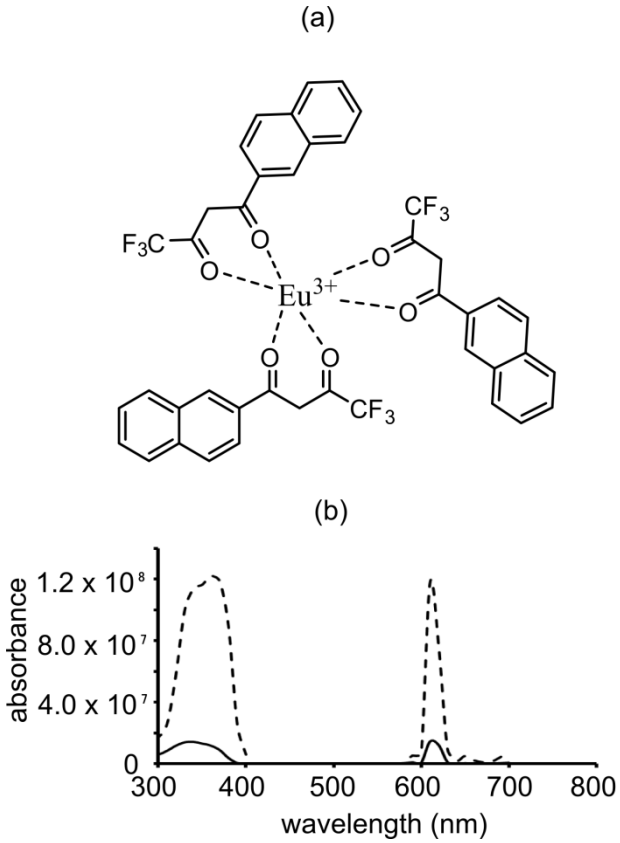

Figure 3.1 Characteristics of PLA-PEG nanoparticles doped with europium chelate. (a) Representative structure of $Eu(NTA)_3$ chelate. (b) Excitation and emission spectra for 1 mg/mL nanoparticle suspension in PBS (solid lines) and 0.1 mg/mL chelate solution in acetone (dotted lines) under time resolved conditions.

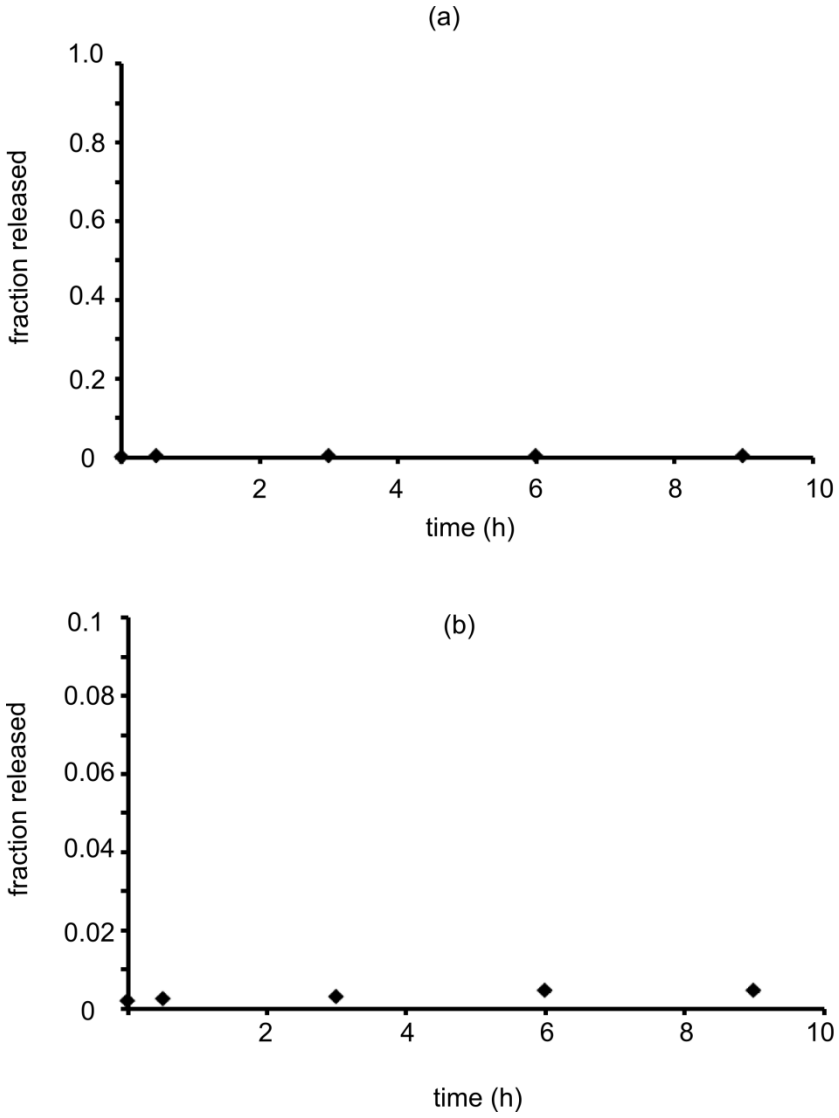

Figure 3.2. Release data for $Eu(NTA)_3$ doped PLA-PEG nanoparticles. (a) Release data on a 100% scale. (b) Release data on a 10% scale. Neither scale shows any detectable chelate released.

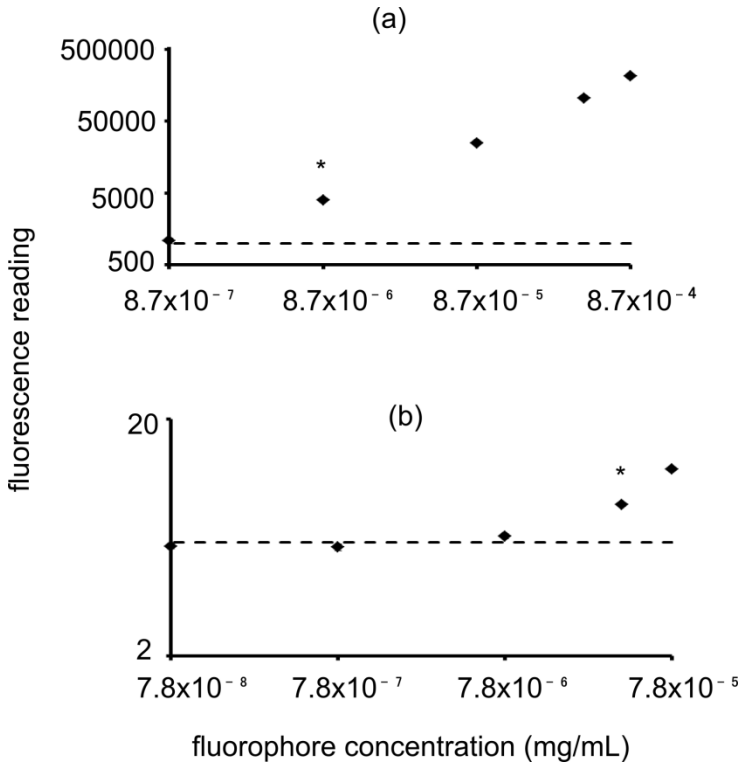

Figure 3.3. Sensitivity analysis of (a) $Eu(NTA)_3$ doped nanoparticles and (b) rhodamine B doped nanoparticles. Dotted lines correspond to the sensitivity limit. $Eu(NTA)_3$ doped nanoparticles are more sensitive than rhodamine B doped nanoparticles. * Lowest concentration that is statistically different from sensitivity limit at $p<0.01$.

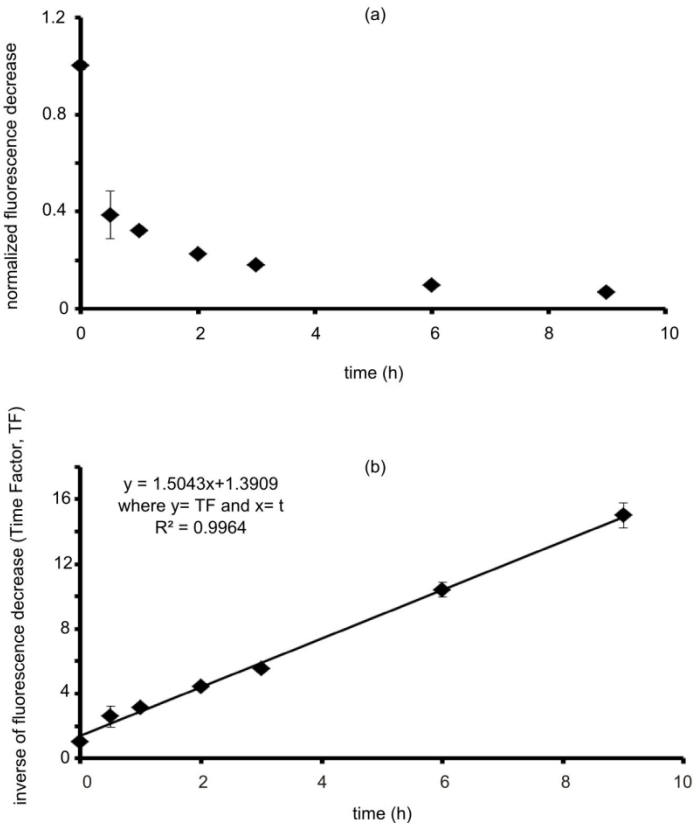

Figure 3.4. Fluorescent decrease of $Eu(NTA)_3$ doped nanoparticles in plasma vs. time. (a) Second order decrease in fluorescence. (b) Manipulated inverse of second order decrease. Particles lose fluorescence due to the introduction of water into the chelate.

3.3.4 The influence of tissue on europium TRF signal. The signal of europium chelate-doped PLA-PEG particles in tissue homogenates was far above background time-resolved autofluorescence (Table 3.1). However, when nanoparticles were titrated into tissue homogenates, signal interference was detected and attributed to the presence of iron, although other unknown influences could not be ruled out.[19] Therefore, to account for the influence of tissue composition on the TRF signal, an interference factor was created for each tissue and used in the calculation of the final biodistribution data (Table 3.1). The greatest interference is seen in the liver and kidneys with a factor of 0.11 ± 0.008 and 0.11 ± 0.005, respectively. The lowest interference is in the brain with a factor of 0.37 ± 0.02.

3.3.5 Nanoparticle biodistribution. Using the second order degradation TFR curve and tissue interference factor to calculate the percent of injected NP in each tissue, biodistribution curves were produced for each tissue type. Particles were detectable above background in all tissues (Figure 3.5). From the area under the curves (Table 3.2), the highest tissue accumulation for these PLA-PEG nanoparticles was in the spleen, followed by the liver and kidney. Particles were also present in the heart, lung and brain.

3.4 Discussion

PLA is a biodegradable polyester with degradation kinetics that can be engineered to control the rate of encapsulated drug release.[20,21] PEG is often used in concert with PLA NPs to enhance NP circulation time by altering the NP's interaction with macrophages and blood proteins, acting as an inert shield against the biological milieu.[22,23]

PLA-PEG NPs have begun to enter clinical trials in the United States for their ability to alter the biodistribution of low molecular weight drugs and to help facilitate their transport to target therapeutic sites and reduce their side effect profiles.[21] For example, Genexol-PM is a passively targeted PEG-PLA micelle formulation of paclitaxel in Phase II clinical trials for the treatment of metastatic breast cancer. It

Table 3.1. Time resolved fluorescence signal and associated tissue interference (arbitrary units). The interference ratio of individual tissue homogenates compared to nanoparticle (NPs) suspension was determined by dividing the time resolved fluorescence of NPs doped into various tissue homogenates with NPs in PBS.

Organ	Auto Fluorescent Reading	Doped Fluorescent Reading	Interference Ratio
NP	---	$2.77 \times 10^6 \pm 3.2 \times 10^4$	1.0 ± 0.02
Liver	587 ± 43	$3.07 \times 10^5 \pm 2.3 \times 10^4$	0.11 ± 0.008
Kidney	514 ± 51	$2.98 \times 10^5 \pm 1.4 \times 10^4$	0.11 ± 0.005
Heart	476 ± 40	$7.64 \times 10^5 \pm 7.8 \times 10^5$	0.28 ± 0.03
Lung	522 ± 28	$4.23 \times 10^5 \pm 4.3 \times 10^3$	0.15 ± 0.002
Spleen	540 ± 68	$5.64 \times 10^5 \pm 1.1 \times 10^5$	0.20 ± 0.04
Brain	530 ± 39	$1.03 \times 10^6 \pm 5.9 \times 10^4$	0.37 ± 0.02
Blood	505 ± 51	$5.04 \times 10^5 \pm 2.3 \times 10^5$	0.18 ± 0.08

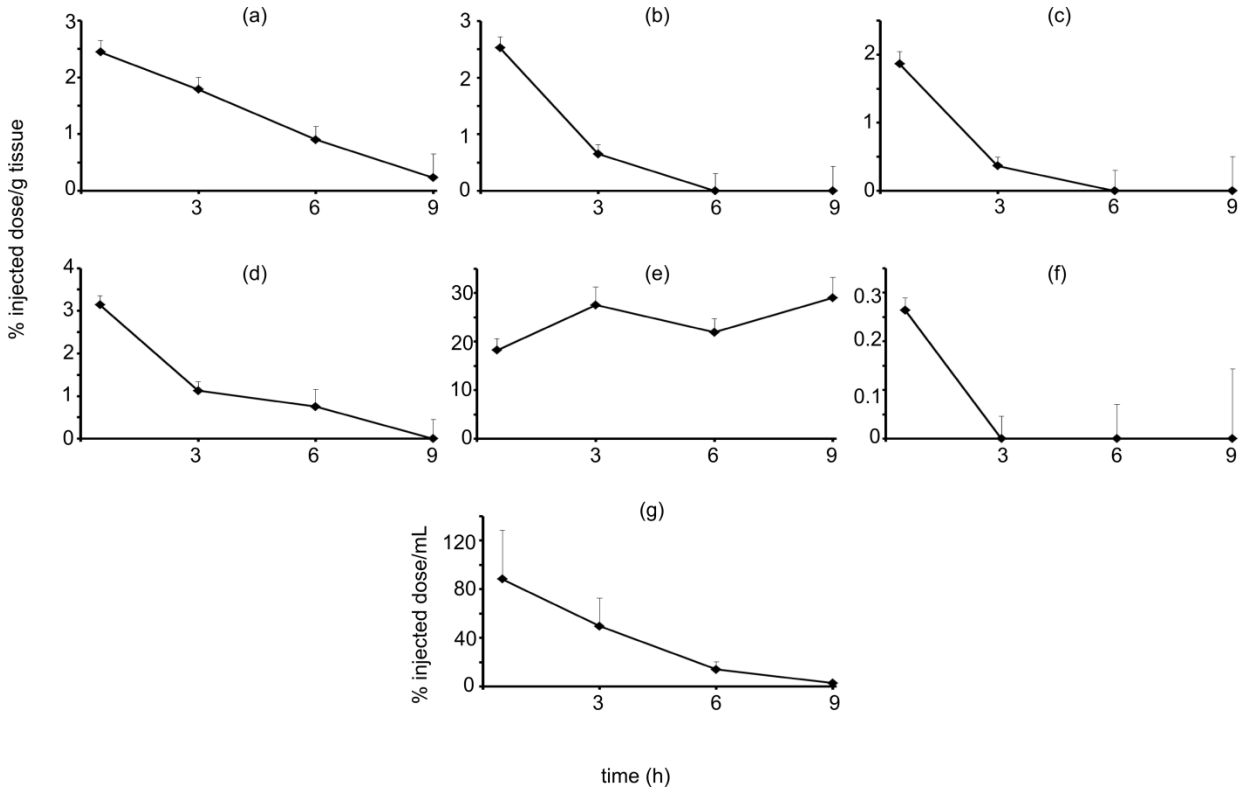

Figure 3.5. Biodistribution of $Eu(NTA)_3$ doped PLA-PEG nanoparticles in (a) liver, (b) kidney, (c) heart, (d) lung, (e) spleen, (f) brain, and (g) blood.

Table 3.2. Area under the curve from 30 minutes to 9 hours calculated with the trapezoid rule. *blood values represented as % ID/mL.

Organ	AUC (%ID h/g)
Liver	11.0 ± 1.6
Kidney	4.96 ± 1.6
Heart	3.33 ± 1.6
Lung	9.28 ± 2.0
Spleen	208 ± 20
Brain	0.33 ± 0.4
Blood*	293 ± 103

has demonstrated an extremely promising response rate of close to 60% and is progressing through further trials.[24] PLA-PEG NPs have also shown promise as an actively targeted drug delivery system via conjugation with various targeting ligands.[21] For example, Hrkach et. al. reported pre-clinical development of a prostate-specific membrane antigen-targeted PLA-PEG docetaxel NP for the treatment of prostate cancer which has demonstrated high success rates.[25] Additional studies show NP-specific receptor binding mediated through targeting ligands and monoclonal antibodies with several other types of cancer including ovarian, lymphoma[26], and glioma cells[2]. There is also ongoing work with PLA-PEG NPs for drug transport across the blood brain barrier[27] and for the treatment of spinal cord injuries[28] – both areas where it is particular difficult to achieve high concentrations of drug.

This report outlines an easy and sensitive method to quantify biodegradable NPs following intravenous administration. The goal was to define a method to eliminate the challenges caused by signal overlap with tissue autofluorescence. The NPs reported in this study are consistent in shape and size with previous studies using the same NP fabrication methods.[7,29,30] Europium chelate encapsulation was confirmed with excitation and emission maxima appropriate for the chelate used under TRF.[31] [31] Release experiments show no detectable europium chelate being released from the NPs implying that all measurements *in vivo* are representative of intact particles and not free chelate. Sensitivity analysis compared europium chelate doped nanoparticles to RhoB doped nanoparticles. RhoB was chosen as a model dye for comparison as it is just outside the fluorescent range that exhibits the highest autofluorescence and has been used in literature.[32–34] The encapsulation efficiency was low for RhoB since it is more hydrophilic than the europium chelate; however, when sensitivity is compared to fluorophore concentration, europium chelate nanoparticles were almost 5 times more detectable than RhoB nanoparticles.

Further *in vitro* testing showed a loss in NP fluorescence that followed a second-order process in the presence of plasma, likely from water penetration into the NP resulting in fluorescence quenching.[18] Studies with similar europium chelates have tried to prevent water-induced TRF quenching; however, those chelates contained an extra molecule (trioctylphosphine oxide) which occupied the remaining

coordination sites of europium in hopes of preventing water quenching. Attempts in this work were made to formulate PLA-PEG NPs doped with this identical chelate, however significant aggregation occurred when this chelate was introduced.[16,35,36] Further protection from europium chelate quenching can be provided by encapsulation into a non-biodgradeable nanoparticle, such as polystyrene. Polystyrene nanoparticles encapsulating europium chelates have proven utility *in vitro*[16,17], however biodegradable NPs provide advantages as drug carriers in drug delivery applications. Biodegradable nanoparticles can be naturally metabolized, leading to decreasing accumulation in the liver and spleen compared to non-biodegradable nanoparticles. This leads to less toxicity and is therefore a better option for nanoparticle drug delivery.[37] PLA-PEG, as discussed above, represents a widely studied class of biodegradable polymeric nanoparticles and thus, detection methods such as the one presented in this work are invaluable. This study aimed to use TRF to assess the biodistribution of unadulterated PLA-PEG NPs by correcting for both water quenching and tissue interference.

Detection of the particles was well above background autofluorescence in all tissues, largely due to europium's large Stokes shift and time resolved characteristics. One challenge this method of detection does face, in context to NP biodistribution, is the interference of iron ions in various tissues. Iron has been previously reported to quench europium chelate fluorescence.[19] Therefore, to correct for the diverse concentration of iron in individual tissues, tissue-specific interference factors were obtained by doping NPs with individual organ tissue homogenates and used to accurately calculate NP biodistribution *in vivo*. To address iron variation among individuals, analysis was performed using tissues from 3 different mice. However, variation among species was not explored and should be considered in future applications.

The biodistribution studies showed that this TRF approach is able to detect PLA-PEG NPs in all harvested tissues including the liver, kidney, heart, lung, spleen, brain and blood. The data correlate well with other PLA-PEG NP biodistribution reports.[38,39] There is high uptake in the spleen signaling uptake by the RES.

3.5 Conclusion

While the reported method of TRF detection of NPs using a hydrophobic europium chelate requires correction for both water and iron interactions, the method is sensitive, simple and robust. Alternative detection methods can require laborious post processing steps (e.g., HPLC) or specialized handling of material and tissue (e.g. radiolabel), where this TRF approach requires only the use of a fluorescent plate reader. The utility of a simple detection method for PLA-PEG NPs extends beyond this initial work to future use in investigation of targeting moieties to alter the biodistribution of NPs.

REFERENCES

(1) Xiao, R. Z., Zeng, Z. W., Zhou, G. L., Wang, J. J., Li, F. Z., and Wang, A. M. (2010) Recent advances in PEG-PLA block copolymer nanoparticles. *Int. J. Nanomedicine 5*, 1057–1065.

(2) Pulkkinen, M., Pikkarainen, J., Wirth, T., Tarvainen, T., Haapa-aho, V., Korhonen, H., Seppälä, J., and Järvinen, K. (2008) Three-step tumor targeting of paclitaxel using biotinylated PLA-PEG nanoparticles and avidin-biotin technology: Formulation development and in vitro anticancer activity. *Eur. J. Pharm. Biopharm. 70*, 66–74.

(3) Andersson-Engels, S., Klinteberg, C., Svanberg, K., and Svanberg, S. (1997) In vivo fluorescence imaging for tissue diagnostics. *Phys. Med. Biol. 42*, 815–824.

(4) Andersson-Engels, S., and Wilson, B. (1992) In vivo fluorescence in clinical oncology: fundamental and practical issues. *J. Cell Pharmacol. 3*, 66–79.

(5) Monici, M. (2005) Cell and tissue autofluorescence research and diagnostic applications. *Biotechnol. Annu. Rev. 11*, 227–256.

(6) Frangioni, J. (2003) In vivo near-infrared fluorescence imaging. *Curr. Opin. Chem. Biol. 7*, 626–634.

(7) Vila, A., Gill, H., McCallion, O., and Alonso, M. J. (2004) Transport of PLA-PEG particles across the nasal mucosa: effect of particle size and PEG coating density. *J. Control. Release 98*, 231–244.

(8) Farokhzad, O. C., Jon, S., Khademhosseini, A., Tran, T.-N. T., Lavan, D. a, and Langer, R. (2004) Nanoparticle-aptamer bioconjugates: a new approach for targeting prostate cancer cells. *Cancer Res. 64*, 7668–7672.

(9) Resch-Genger, U., Grabolle, M., Cavaliere-Jaricot, S., Nitschke, R., and Nann, T. (2008) Quantum dots versus organic dyes as fluorescent labels. *Nat. Methods 5*, 763–775.

(10) Hemmilä, I., and Laitala, V. (2005) Progress in lanthanides as luminescent probes. *J. Fluoresc. 15*, 529–542.

(11) Zhang, Y., Wei, W., Das, G. K., and Yang Tan, T. T. (2014) Engineering lanthanide-based materials for nanomedicine. *J. Photochem. Photobiol. C Photochem. Rev. 20*, 71–96.

(12) Ye, Z., Tan, M., Wang, G., and Yuan, J. (2004) Novel fluorescent europium chelate-doped silica nanoparticles: preparation, characterization and time-resolved fluorometric application. *J. Mater. Chem. 14*, 851.

(13) Vuojola, J., and Soukka, T. (2014) Luminescent lanthanide reporters: new concepts for use in bioanalytical applications. *Methods Appl. Fluoresc. 2*, 012001.

(14) Maldiney, T., Richard, C., Seguin, J., Wattier, N., Bessodes, M., and Scherman, D. (2011) Effect of core diameter, surface coating, and PEG chain length on the biodistribution of persistent luminescence nanoparticles in mice. *ACS Nano 5*, 854–862.

(15) Mignet, N., Chermont, Q. L. M. De, Randrianarivelo, T., Seguin, J., Richard, C., Bessodes, M., and Scherman, D. (2006) Liposome biodistribution by time resolved fluorimetry of lipophilic europium complexes. *Eur. Biophys. J. 35*, 155–161.

(16) Huhtinen, P., Kivelä, M., Soukka, T., Tenhu, H., Lövgren, T., and Härmä, H. (2008) Preparation, characterisation and application of europium(III) chelate-dyed polystyrene-acrylic acid nanoparticle labels. *Anal. Chim. Acta 630*, 211–216.

(17) Ornatsky, O., Baranov, V., Shen, L., Abdelrahman, A., and Winnik, M. A. (2007) Lanthanide-containing polymer nanoparticles for biological tagging applications : nonspecific endocytosis and cell adhesion. *J. Am. Chem. Soc. 129*, 13653–13660.

(18) Brennetot, R., Georges, J., and Bernard, C. (2000) Investigation of chelate formation , intramolecular energy transfer and luminescence efficiency and lifetimes in the Eu – thenoyltrifluoroacetone – trioctylphosphine oxide – Triton X-100 system using absorbance , fluorescence and photothermal measurements. *Spectrochim. Acta Part A 56*, 703–715.

(19) Chen, Z., Sun, Y., Zhang, L., Sun, D., Liu, F., Meng, Q., Wang, R., and Sun, D. (2013) A tubular europium-organic framework exhibiting selective sensing of Fe3+ and Al3+ over mixed metal ions. *Chem. Commun. 49*, 11557–11559.

(20) Anderson, J. M., and Shive, M. S. (2012) Biodegradation and biocompatibility of PLA and PLGA microspheres. *Adv. Drug Deliv. Rev. 64*, 72–82.

(21) Kamaly, N., Xiao, Z., Valencia, P. M., Radovic-Moreno, A. F., and Farokhzad, O. C. (2012) Targeted polymeric therapeutic nanoparticles: design, development and clinical translation. *Chem. Soc. Rev. 41*, 2971–3010.

(22) Gref, R., Minamitake, Y., Peracchia, M. T., Torchilin, V., Langer, R., and Bernard, C. (1994) Long-Circulating Biodegradable Nanospheres Polymeric. *Scienc. 263*, 1600–1603.

(23) Gref, R., Lu, M., Sud, P., and Pharmaceutiques, E. (2000) " Stealth " corona-core nanoparticles surface modified by polyethylene glycol (PEG): influences of the corona (PEG chain length and surface density) and of the core composition on phagocytic uptake and plasma protein adsorption. *Colloids Surfaces B Biointerfaces 18*, 301–313.

(24) Lee, K. S., Chung, H. C., Im, S. A., Park, Y. H., Kim, C. S., Kim, S.-B., Rha, S. Y., Lee, M. Y., and Ro, J. (2008) Multicenter phase II trial of Genexol-PM, a Cremophor-free, polymeric micelle formulation of paclitaxel, in patients with metastatic breast cancer. *Breast Cancer Res. Treat. 108*, 241–50.

(25) Hrkach, J., Von Hoff, D., Mukkaram Ali, M., Andrianova, E., Auer, J., Campbell, T., De Witt, D., Figa, M., Figueiredo, M., Horhota, A., Low, S., McDonnell, K., Peeke, E., Retnarajan, B., Sabnis, A., Schnipper, E., Song, J. J., Song, Y. H., Summa, J., Tompsett, D., Troiano, G., Van Geen Hoven, T., Wright, J., LoRusso, P., Kantoff, P. W., Bander, N. H., Sweeney, C., Farokhzad, O. C., Langer, R., and Zale, S. (2012) Preclinical development and clinical translation of a PSMA-targeted docetaxel nanoparticle with a differentiated pharmacological profile. *Sci. Transl. Med. 4*, 1–11.

(26) Nobs, L., Buchegger, F., Gurny, R., and Alle, E. (2006) Biodegradable nanoparticles for direct or two-step tumor immunotargeting. *Bioconjug. Chem. 17*, 139–145.

(27) Olivier, J. (2005) Drug transport to brain with targeted nanoparticles. *NeuroRx 2*, 108–119.

(28) Piantino, J., Burdick, J. a, Goldberg, D., Langer, R., and Benowitz, L. I. (2006) An injectable, biodegradable hydrogel for trophic factor delivery enhances axonal rewiring and improves performance after spinal cord injury. *Exp. Neurol. 201*, 359–367.

(29) Govender, T., Riley, T., Ehtezazi, T., Garnett, M. C., Stolnik, S., Illum, L., and Davis, S. S. (2000) Defining the drug incorporation properties of PLA-PEG nanoparticles. *Int. J. Pharm. 199*, 95–110.

(30) Ren, W., Chang, J., Yan, C., Qian, X., Long, L., He, B., Yuan, X., Kang, C., Betbeder, D., Sheng, J., and Pu, P. (2010) Development of transferrin functionalized poly(ethylene glycol)/poly(lactic acid) amphiphilic block copolymeric micelles as a potential delivery system targeting brain glioma. *J. Mater. Sci. Mater. Med. 21*, 2673–2681.

(31) Carlos, L. D., De Mello Donegá, C., Albuquerque, R. Q., Alves, S., Menezes, J. F. S., and Malta, O. L. (2003) Highly luminescent europium(III) complexes with naphtoiltrifluoroacetone and dimethyl sulphoxide. *Mol. Phys. 101*, 1037–1045.

(32) Farokhzad, O. C., Jon, S., Khademhosseini, A., Tran, T. T., Lavan, D. a, and Langer, R. (2004) Nanoparticle-aptamer Bioconjugates : a new approach for targeting prostate cancer cells. *Cancer R 64*, 7668–7672.

(33) Essa, S., Rabanel, J. M., and Hildgen, P. (2011) Characterization of rhodamine loaded PEG-g-PLA nanoparticles (NPs): Effect of poly(ethylene glycol) grafting density. *Int. J. Pharm. 411*, 178–187.

(34) Ma, P., Liu, S., Huang, Y., Chen, X., Zhang, L., and Jing, X. (2010) Lactose mediated liver-targeting effect observed by ex vivo imaging technology. *Biomaterials 31*, 2646–2654.

(35) Härmä, H., Graf, C., and Hänninen, P. (2008) Synthesis and characterization of core-shell europium(III)-silica nanoparticles. *J. Nanoparticle Res. 10*, 1221–1224.

(36) Yin, D., Liu, B., Zhang, L., and Wu, M. (2011) Synthesis of Eu(III): naphtoyltrifluoroacetone:trioctylphosphineoxide complex-doped silica fluorescent nanoparticles through a new approach. *J. Nanoparticle Res. 13*, 7271–7276.

(37) Owens, D. E., and Peppas, N. A. (2006) Opsonization, biodistribution, and pharmacokinetics of polymeric nanoparticles. *Int. J. Pharm. 307*, 93–102.

(38) Ueki, K., Onishi, H., Sasatsu, M., and Machida, Y. (2009) Preparation of carboxy-PEG-PLA nanoparticles loaded with camptothecin and their body distribution in solid tumor-bearing mice. *Drug Dev. Res. 70*, 512–519.

(39) Xia, H., Gao, X., Gu, G., Liu, Z., Hu, Q., Tu, Y., Song, Q., Yao, L., Pang, Z., Jiang, X., Chen, J., and Chen, H. (2012) Penetratin-functionalized PEG–PLA nanoparticles for brain drug delivery. *Int. J. Pharm. 436*, 840–850.

CHAPTER 4

EXPLOITATION OF P-GLYCOPROTEIN USING RHODAMINE THETHERED NANOPARTICLES LEADS TO TARGETED NANOPARTICLE DELIVERY TO THE BRAIN

(Contributors: Hannah Watkins, Elizabeth Wayne)

4.1 Introduction

Neurologically-derived diseases present consistent challenges in the field of drug delivery, partially due to the limited success in pharmaceutical development of therapies selective for the central nervous system (CNS). CNS drug development ranks among the lowest in percentage to reach clinical approval when compared to systemic diseases [1]. The main limitations in CNS drug development stem from challenges in drug delivery. The blood-brain barrier (BBB), which serves as a protective function with its tight junctions and membrane transport proteins (such as P-glycoprotein), also limits transport of potential therapeutics into the brain, creating a challenge for drug delivery [2].

In recent years, strategies explored to target drug delivery to CNS include focused ultrasound [3], intranasal delivery [4], and receptor mediated (RM) targeting. RM brain drug targeting has been explored as a method to enhance the therapeutic effects in the CNS [5] and has been used to deliver small molecules, antibodies, peptides, proteins, and other agents [6]. Both transferrin [7–10] and insulin[11] have been investigated as targeting agents owing to their ability to initiate receptor mediated endocytosis in the endothelium of the BBB; however, the endogenous presence of both transferrin and insulin competes for binding with the targeted systems[12]. Targeting receptors with antibodies has been another popular technique to target drugs to the brain, but this technique has been associated with potential safety risks, including hemolytic anemia. Antibody fusion proteins have been an attractive solution to overcome the associated safety risks with antibody targeting, but safety concerns have not been fully realized[13] . Collectively, these literature results suggest that the investigation into new alternative approaches to target drugs to the brain are warranted.

In this work, we hypothesize that P-glycoprotein (P-gp) could be exploited as a novel target for drug delivery to the brain. P-gp is a 170 kDa transmembrane protein that belongs to a large family of endogenous transport systems located in the brain capillary endothelial cells. It is responsible for the active transport of a wide variety of substances from the CNS into the capillaries (i.e., out of the brain) and presents a significant challenge for drug delivery to treat neurologically-derived disesase. Previous studies have explored targeting P-gp in cancer models using antibodies as targeting moieties [14]; however the technology has not been extended to delivery to the CNS. The work presented herein explores the utility of P-gp substrates (i.e., small molecules that are actively transported by P-gp out of the CNS) to act as anchor molecules to enhance the local concentration of drug-loaded nanoparticles in the brain. The premise was that a P-gp substrate tethered to the surface of a nanoparticle through a water soluble polymer linker would bind to P-gp. Unable to efflux the entire nanoparticle, P-gp binding would thereby retain the nanoparticle within the capillary through a "fish-hook" like architecture (Figure 4.1). Our findings show that when rhodamine dyes with well-characterized P-gp specificity were tethered to the surface of nanoparticles formulated from polylactic acid-polyethylene glycol diblock copolymers, the nanoparticle accumulation in the brain (as measured by the area under the curves) was greater than 2-fold than untargeted nanoparticles as well as in mdr1a (-/-) knockout mice.

4.2 Materials and Methods

4.2.1 Materials.O-(2-Aminoethyl) polyethylene glycol (PEG-NH_2, M_p 5000), rhodamine 123 (Rho123), rhodamine 6G (Rho6G), triethylamine, dimethyl formaldehyde (DMF), monomethoxy polyethylene glycol (mPEG, M_n 5000), anhydrous toluene, stannous octoate, europium chloride hexahydrate, 4,4,4-trifluoro-1-(2-naphthyl-1,3-butanedione) (NTA), acetone, dichloromethane (DCM), magnesium sulfate, poloxamer 188 solution and RIPA buffer were purchased from Sigma Aldrich (Saint Louis, MO). D,L-Lactide was purchased from TCI America (Portland, OR). Phosphate buffered saline (PBS) was purchased from Corning (Corning, NY). Ammonium hydroxide was purchased from Alpha Aesar (Ward

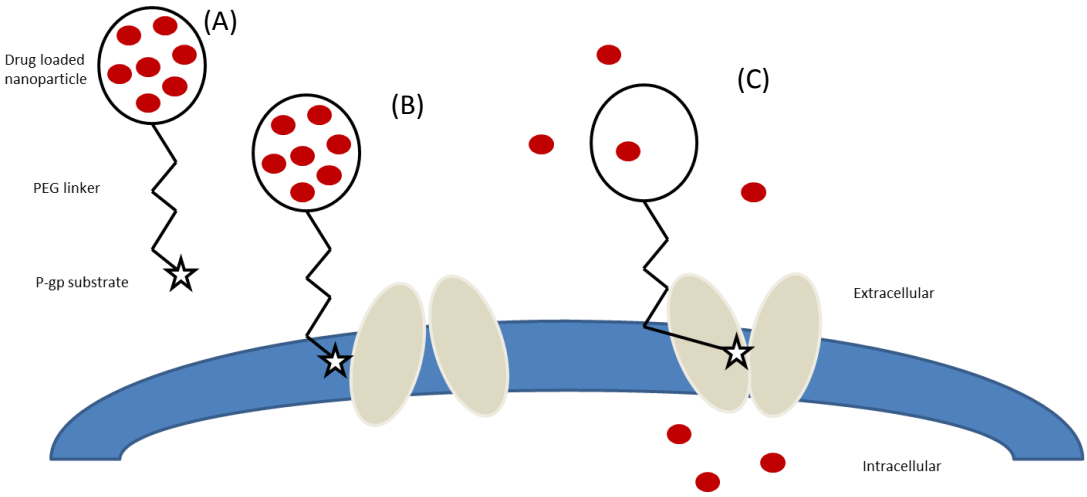

Figure 4.1. Tethering of drug delivery carriers to cells through interaction with P-gp. (A) Drug carrier/PEG linker/P-gp substrate (B) PEG linker spans membrane as P-gp substrate diffuses into cell membrane. (C) Export of P-gp substrate by P-gp tethers drug carrier to cell and drug is released locally.

Hill, MA). Diethyl ether was purchased from Fisher Chemicals (Waltham, MA). Methanol was purchased from Macron Fine Chemicals (Avantor Performance Materials, Center Valley, PA).

4.2.2 PEG azeotropic distillation. Monomethoxy PEG (50 g, M_n 5000) was dissolved in 200 mL of anhydrous toluene with slight heating. Distillation was carried out under reflux at 128 °C for 2 hours using a Dean Stark trap. The remaining toluene was removed by rotoevaporation and the PEG product dried under high vacuum.

4.2.3 Conjugation of PEG-Rho123 and PEG-Rho6G. Conjugates of PEG with Rho123 or Rho6G were synthesized with minor variation of methods previously published by our group [15]. For the synthesis of PEG-Rho6G, the PEG-NH_2 (M_n 5000, 241.6 mg, $4.8x10^{-5}$ mol) was dissolved in anhydrous DMF (2 mL) with excess TEA at room temperature. Excess TEA was added to Rho6G powder (77.2 mg, $1.6x10^{-4}$ mol) which was then dissolved in anhydrous DMF (12 mL) with slight heating. For production of PEG-Rho123, PEG-NH_2 (M_n 5000, 438.3 mg, $8.7x10^{-5}$ mol) was dissolved in anhydrous DMF (2 mL) with excess TEA at room temperature. Excess TEA was added to Rho123 powder (100 mg, $2.6x10^{-4}$ mol) which was then dissolved in anhydrous DMF (2 mL) at room temperature. For both PEG-Rho6G and PEG-Rho123 production, the two DMF solutions were combined and stirred at 30 °C for 1 week while protected from light with an aluminum foil cover. The respective solutions were then diluted with Milli-Q water (38 mL) and dialyzed (MWCO 2000g/mol) in the dark against deionized water with 14 water exchanges over 1 week at room temperature. Following dialysis the solution was dried to a light pink powder by lyophilization in the dark for 3 days. Product yields for PEG-Rho6G and PEG-Rho123 were 58 % and 79.4 %, respectively. ^{1}H NMR was conducted on an Inova 600 MHz spectrometer at 25 °C. PEG-Rho6G conjugate ^{1}H NMR (600 MHz, DMSO-d_6) δ(ppm): 4.55 (t, 1H, **H**O PEG), 3.5 (s, 4H, C**H**$_2$C**H**$_2$O PEG), 6.06 (s, 2H, ArH Rho6G), 6.26 (s, 2H, ArH Rho6G), 6.97 (d, 1H, ArH Rho6G), 7.50 (m, 2H, Ar**H** Rho6G), 7.77 (d, 1H, Ar**H** Rho6G), 1.86 (s, 6H, ArC**H**$_3$), 1.21 (t, 6H,NCH$_2$C**H**$_3$). PEG-

Rho123 conjugate ^{1}H NMR (600 MHz, DMSO-d_6) δ (ppm): 4.55 (t, 1H, **H**O PEG), 3.44 (s, 4H, C**H**$_2$C**H**$_2$O PEG), 6.16 (s, 1H, Ar**H** Rho123), 6.17 (s, 1H, Ar**H** Rho123), 6.23 (d, 1H, Ar**H** Rho123), 6.32 (d, 1H, Ar**H** Rho123), 7.00 (d, 1H, Ar**H** Rho123), 7.50 (m, 4H, Ar**H** Rho123), 7.74 (d, 1H, Ar**H** Rho123)

4.2.4 PLA-PEG diblock copolymer synthesis and characterization. Lactide was recrystallized once from methanol and dried under high vacuum prior to the reaction. PEG (400 mg, 0.08 mmol) and lactide (1843 mg, 12.8 mmol) were dissolved in anhydrous toluene (6 mL) under argon in a 25 mL Schlenk flask. Rho6G-PEG (54.3 mg, 0.01 mmol) and lactide (250.2 mg, 1.7 mmol) were dissolved in anhydrous toluene (1 mL) under argon in a 10 mL Schlenk flask. Rho123-PEG (100 mg, 0.02 mmol) and lactide (428.25 mg, 3.0 mmol) were dissolved in anhydrous toluene (1 mL) under argon in a 10 mL Schlenk flask. For all reactions the reaction vessels were placed in a 111 °C silicon oil bath. Upon the initiation of toluene reflux (111 °C), toluene (2 mL for mPEG-PLA, 1 mL for Rho6G-PEG-PLA and Rho123-PEG-PLA) containing stannous octoate (1.1 mol% lactide) was added all at once with stirring. The reaction was allowed to reflux with stirring over 24 hours, after which excess toluene was removed by rotoevaporation until an oily liquid remained and the product collected by precipitation into excess diethyl ether with stirring. The product was collected by filtration, dried overnight under high vacuum and stored at room temperature in a vacuum desiccator until characterization and nanoparticle formulation. The molecular weight of each diblock copolymer was determined by THF GPC (Waters, Milford, MA) using polystyrene standards. The diblock copolymers were characterized by ^{1}H NMR. ^{1}H NMR for mPEG-PLA (600 MHz, DMSO-d_6) ppm: 5.20 (m, C**H** PLA), 3.51 (s,C**H**$_2$C**H**$_2$ PEG), 3.24 (s, C**H**$_3$ PEG), 1.45 (m, C**H**$_3$ PLA). ^{1}H NMR for Rho6G-PEG-PLA (600 MHz, DMSO-d_6) ppm: 5.20 (m, C**H** PLA), 3.24 (s, C**H**$_3$ PEG), 1.45 (m, C**H**$_3$ PLA), 1.83 (s, 6H, ArC**H**$_3$), 6.03 (s, 2H, ArH Rho6G), 6.22 (s, 2H, ArH Rho6G), 6.93 (d, 1H, ArH Rho6G), 7.46 (m, 2H, Ar**H** Rho6G), 7.74 (d, 1H, Ar**H** Rho6G). ^{1}H NMR for Rho123-PEG-PLA (600 MHz, DMSO-d_6) ppm: 5.20 (m, C**H** PLA), 3.24 (s, C**H**$_3$ PEG), 1.45 (m, C**H**$_3$ PLA), 6.60 (d, 1H, Ar**H** Rho123), 7.53 (d, 1H, Ar**H** Rho123), 7.74 (m, 4H, Ar**H** Rho123), 7.82 (d, 1H, Ar**H** Rho123)

4.2.5 Europium(III)tris(4,4,4-trifluoro-1-(2-naphthyl-1,3-butanedione)) chelate synthesis. The europium(III)tris(4,4,4-trifluoro-1-(2-naphthyl-1,3-butanedione)) ($Eu(NTA)_3$) chelate was made as previously reported [16]. In brief, NTA (800 mg) was dissolved in 75 mL of ethanol (75 mL) and ammonium hydroxide (20.4 mL of 28%) with stirring. On complete dissolution, a solution of europium chloride hexahydrate (366 mg) in DI water (10 mL) was added dropwise to the NTA solution. The chelate was allowed to form overnight by ethanol evaporation with stirring at room temperature. The resulting solution was then extracted once with and equal volume of DCM, the organic layer isolated and washed with DI water three times. The DCM solution was dried over magnesium sulfate, DCM removed by rotoevaporation, and the resulting solid dried under high vacuum.

4.2.6 Nanoparticle fabrication and characterization. mPEG-PLA (100 mg) was dissolved in DCM (1 mL) then mixed with a DCM solution of $Eu(NTA)_3$ (1 mg/mL, 1 mL total). The solution was then diluted with acetone (8 mL), vortexed and added dropwise into MilliQ water (10 mL) with stirring. The organic solvents were removed by rotoevaporation and the nanoparticles collected by ultracentrifugation using a Bruker LE-80 ultracentrifuge at 20,000 rpm for 30 minutes. The nanoparticles in the pellet were washed with MilliQ water and ultracentrifuged again at 20,000 rpm for 30 minutes. This process was repeated once more and the final pellet was resuspended in a final volume of 1 mL of MilliQ water. Poloxamer 188 (20 µL of 10% solution) was added to prevent aggregation prior to lyophilization overnight. For 10% Rho6G-PEG-PLA and 10% Rho123-PEG-PLA nanoparticles the same procedure was followed but with 90 mg of mPEG-PLA and 10 mg of Rho6G-PEG-PLA or Rho123-PEG-PLA, respectively.

A 1 mg/mL solution of the nanoparticle solutions were made with MilliQ water and sonicated for 10 minutes. After sonication the solutions were filtered through a 0.45 µm filter and diluted 1:2 into a final solution of 1mM HEPES buffer. Size, polydispersity, and zeta potential were measured using a Malvern NanoZS (United Kingdom). The morphology of the particles was evaluated by TEM. The 1

mg/mL nanoparticle suspension was negatively stained with 2% uranyl acetate on titanium grids and imaged using a FEI T12 spirit TEM. To visualize the incorporation of $Eu(NTA)_3$ into the particles, solutions of unloaded and $Eu(NTA)_3$ loaded nanoparticles were imaged under natural and UV light.

4.2.7 In vivo biodistribution. Seven week old ND4 Swiss Webster mice (WT mice) were purchased from Harlan Sprague Dawley. P-glycoprotein knockout mice (mdr1 (-/-)) were purchased from Charles River Laboratories. A suspension of nanoparticles (1 mg/mL) in sterile PBS was sonicated for 10 - 30 minutes until the solution was clear and then flowed through a 0.45 µm filter. A 200 µL aliquot of the nanoparticle suspension was injected intravenously through the tail vein. For WT mice, at 0.5, 3, 6 and 9 hours, five mice were euthanized by CO_2 inhalation under an approved IACUC protocol (Cornell University, protocol number 2012-0034). For mdr1 (-/-) mice at 3 hours, five mice were also euthanized. Blood was drawn via cardiac puncture and the liver, kidneys, heart, lungs, spleen and brain removed. Each organ was weighed, homogenized in 2 mL of RIPA buffer and the resulting mixtures were centrifuged at 800 x g for 10 minutes. Time-resolved fluorescence was measured at an excitation and emission of 340 and 610 nm, respectively, for three separate samples of the homogenate supernatant for each of the five mice per organ. Percent injected dose was determined according to our previous studies. In brief, percent injected dose was calculated using Equation 1, where RD= raw data, SL= sensitivity limit, ID= injected dose, IF= interference factor, g tissue= gram of tissue and TF= time factor. The sensitivity limit is defined as average background + 3 standard deviations, the interference factor is the measure of signal attenuation caused by individual tissues and time factor represents the signal decay kinetics at 37 °C for each time point.

$$\left[\frac{(RD-SL)}{ID*IF*g\ tissue} * TF\right] * 100 = \frac{\%\ injected\ dose}{g\ tissue} \quad \text{(Eq. 1)}$$

Fluorescent images of brain tissue slices were also obtained for 10% Rho6G-PEG-PLA and mPEG-PLA nanoparticles. To obtain the fluorescent images, mice were anesthetized and perfused with formaldehyde 3 hours after injection. The brain was cryosectioned and imaged on a Zeiss Axio Examiner fluorescent microscope under a DAPI and FITC filter. The FITC filter showed background autofluorescence derived from the tissue and the DAPI filter was used to visualize nanoparticles containing the europium chelate.

4.2.8 Pharmacokinetic modeling of biodistribution data. Pharmacokinetic parameters were determined for the biodistribution data using the Simbiology toolbox in Matlab R2015a (Mathworks, Natick MA). To calculate the half-life from plasma, a two compartment model (Figure 4.2a) with blood as the central component and all tissues as the peripheral component was used. To calculate the transfer between each tissue and blood, a three compartment model (Figure 4.2b) was analyzed. The blood was the central compartment, the tissue of interest was the first peripheral compartment and all other organs made up the second peripheral compartment. To obtain a distribution for plasma half-life and tissue rate constants, undersampling was used by elimination of various time points and recalculating of the parameters. The 0.5h time point was never excluded as appropriate fits were not obtained in its absence.

4.3 Results

4.3.1 Nanoparticle formulation. Copolymers of mPEG-PLA, Rho6G-PEG-PLA and Rho123-PEG-PLA were successfully made with an overall M_n of 13,700, 12,400 and 14,400 respectively and PDI values of 1.6, 1.4 and 1.4, respectively. Particles were made from pure mPEG-PLA, 10% Rho6G-PEG-PLA and 10% Rho123-PEG-PLA with and without $Eu(NTA)_3$. Particle characteristics are summarized in Table 4.1. All particles are ~100 nm in diameter and not statistically different from one another as determined by Student's t-test. Zeta potential values are also equivalent and are approximately -27 mV. When unloaded particles were excited at 526 nm and emittance measured at 555 nm the presence of Rho6G and

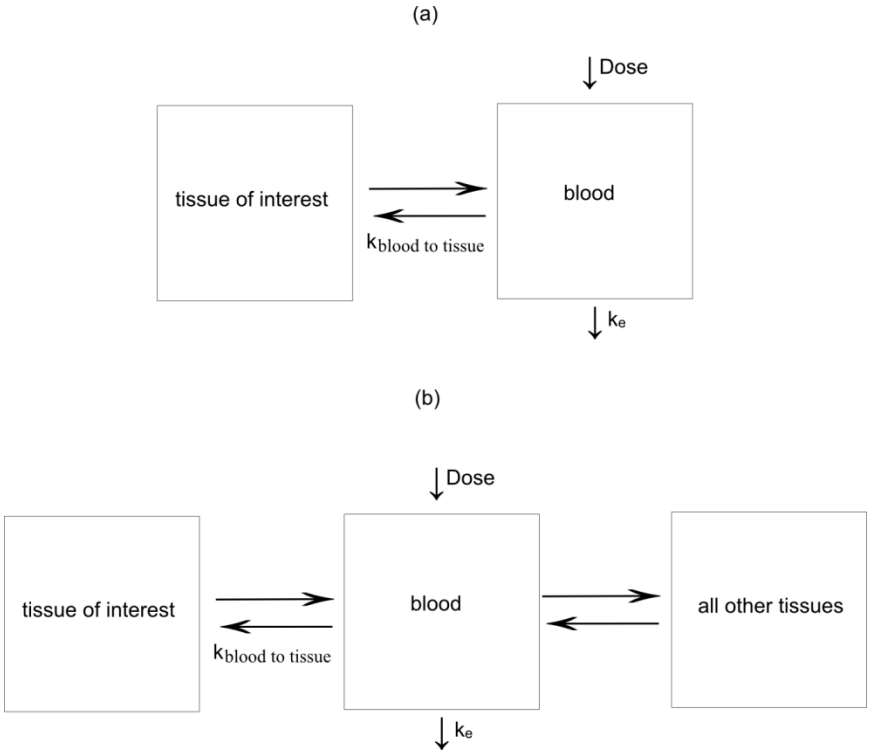

Figure 4.2. Representations of two compartment and three compartment models used to calculate pharmacokinetic parameters.

Rho123 on the particles is detectable. From TEM images (Figure 4.3a) all particle formulations are spherical in shape. The incorporation of $Eu(NTA)_3$ into the particles is evident by the red fluorescent glow of the particles in the loaded sample under UV light and absence of the red fluorescent glow in unloaded particles (Figure 4.3b).

4.3.2 In vivo biodistribution. Biodistribution of Rho6G, Rho123 and methoxy terminated PEG-PLA nanoparticles were evaluated at 0.5, 3, 6 and 9 hours (Figure 4.4). Rho6G-terminated particles showed overall greater accumulation in liver, kidneys, heart, lungs and brain than Rho123 or methoxy- terminated particles. There was significant accumulation of Rho6G-terminated particles in the brain at 3 hours post injection, 0.16 ± 0.02 % ID/g, compared to no accumulation in methoxy or Rho123-terminated particles. These results suggest the particles are targeted to P-gp by Rho6G. Pharmacokinetic parameters were also calculated (Table 4.2). Area under the curve (AUC) values show greater accumulation in liver, kidneys, heart, lung and brain for Rho6G terminated nanoparticles compared to Rho123 and mPEG terminated. The accumulation in the brain was 2.3 times greater for Rho6G terminated nanoparticles than mPEG terminated nanoparticles suggesting that Rho6G nanoparticles can target P-gp in the brain. The half-life ($t_{1/2}$) and transfer rate ($k_{blood\ to\ tissue}$) of Rho6G terminated nanoparticles was also higher than Rho123 and mPEG nanoparticles. Representative brain tissue slices (Figure 4.5) show nanoparticle accumulation in the brain with Rho6G-PEG-PLA nanoparticles (Figure 4.5a) relative to mPEG-PLA nanoparticle accumulation (Figure 4.5b).

Table 4.1. Size, PDI and zeta potential of nanoparticle formulations in HEPES (1 mM) buffer. All sizes are ~100 nm in diameter (not statistically different from each other as determined by Student's t-test at $p < 0.01$) with similar zeta potentials. Greater fluorescence at excitation/emission of 526/555 nm from rhodamine particle formulations show rhodamine attachment to particle.

	loading	size (nm)	PDI	zeta potential (mV)	Fluorescence (526/555 nm)
mPEG	---	121.5 ± 9.0	0.109 ± 0.004	-28.4 ± 0.29	13.2 ± 0.85
10% 123	---	93.9 ± 4.3	0.121 ± 0.02	-26.7 ± 0.47	38.7 ± 2.0
10% 6G	---	106.3 ± 5.0	0.111 ± 0.01	-26.9 ± 0.36	794 ± 50
mPEG	$Eu(NTA)_3$	120.3 ± 9.6	0.069 ± 0.03	-27.5 ± 0.50	---
10% 123	$Eu(NTA)_3$	108.2 ± 4.0	0.073 ± 0.02	-26.8 ± 0.72	---
10% 6G	$Eu(NTA)_3$	99.6 ± 1.1	0.103 ± 0.01	-26.3 ± 0.40	---

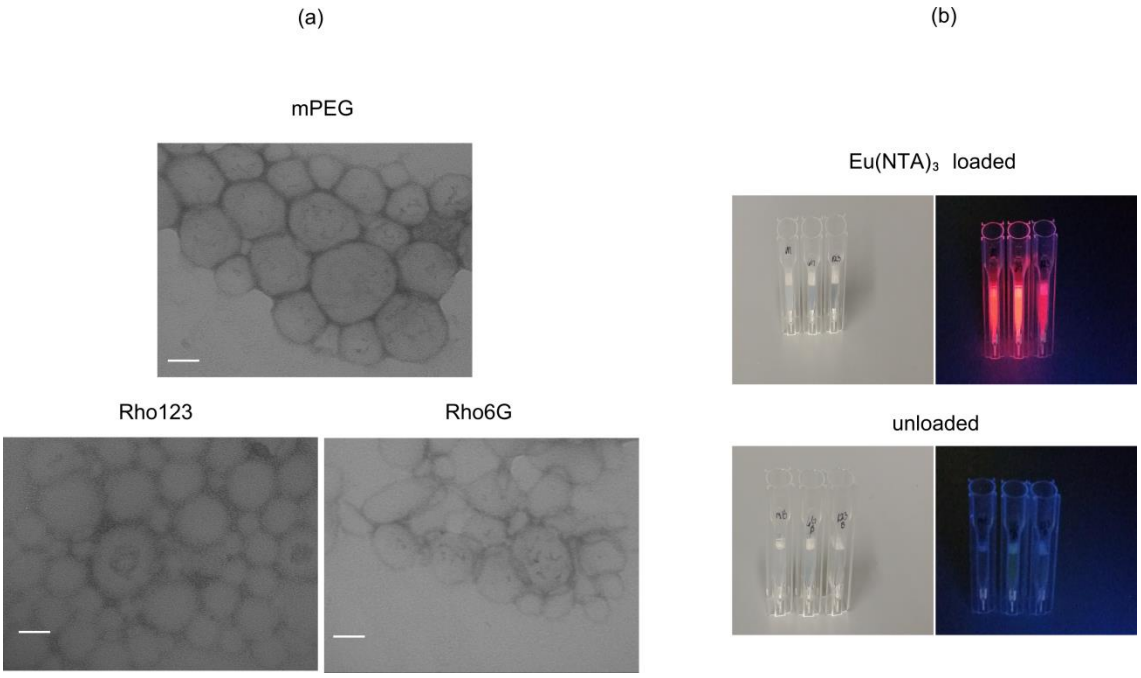

Figure 4.3. (a) TEM images of mPEG-PLA, 10% Rho123-PEG-PLA and 10% Rho6G-PEG-PLA nanoparticles. Scale bar represents 50 nm. All particles types show polydispersity between 50-100 nm in diameter. (b) Fluorescent glow after exposure to UV light of $Eu(NTA)_3$ loaded nanoparticles compared to unloaded particles. From left to right in each panel: mPEG-PLA, 10% Rho6G-PEG-PLA, 10% Rho123-PEG-PLA.

To clarify if the enhanced accumulation of Rho6G-targeted nanoparticles in the brain could be attributed to interactions with P-gp, brain accumulation was measured at 3h in a P-glycoprotein knockout mouse model, mdr1a (-/-), and directly compared to the WT mouse model. Brain accumulation of Rho6G, Rho123 and methoxy-terminated nanoparticles were compared in WT mice vs. mdr1a (-/-) at 3h (Figure 4.6). There is a significant decrease in Rho6G- terminated particles from 0.16 ± 0.02 % in WT mice to 0.08 ± 0.02% in mdr1a (-/-) mice, whereas there are no significant differences in brain accumulation between WT and mdr1a (-/-) mice for either Rho123 or methoxy-terminated particles. Comparison of Rho6G-terminated nanoparticle accumulation in liver, kidneys, heart, lungs, spleen and blood between WT and mdr1a (-/-) mice (Figure 4.7) show that the only other significant difference, in the spleen, is an increase. This finding, that the Rho6G-terminated nanoparticles selectively accumulated in the brain of the mice that express P-gp relative to the mdr1a(-/-) knockout (and relative to the other insignificant changes with Rho123-terminated and untargeted nanoparticles, Figures 4.8 and 4.9, respectively) confirm the potential utility of P-gp as a targeting focus using P-gp substrates.

4.4 Discussion

The most common approach to increase the uptake of low molecular weight therapeutics into the brain is to optimize the partition coefficient, which allows the passive diffusion across the capillary endothelia that form the BBB. The shortcoming of this approach is that the compound passively diffuses across all cell membranes, which leads to a high volume of distribution and a subsequent increase in adverse side effects. Alteration of the biodistribution of these compounds to increase their local

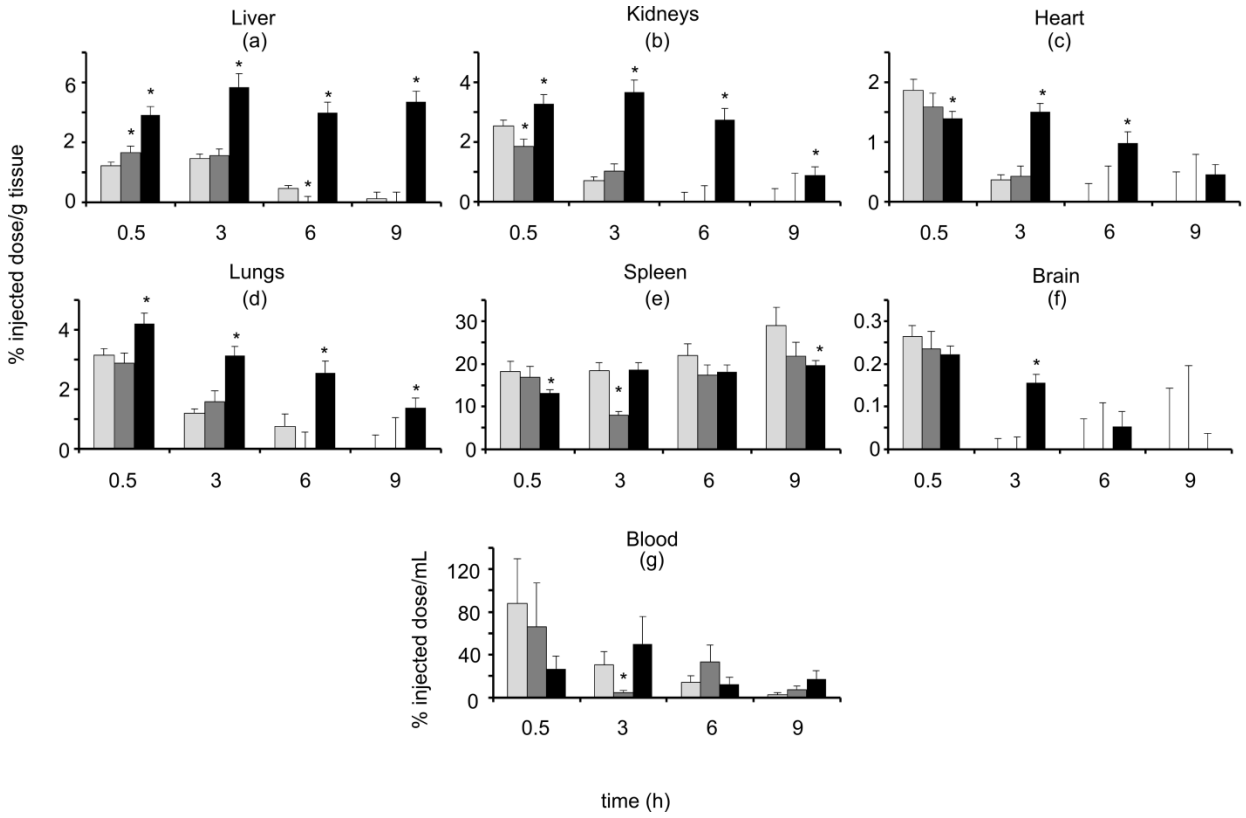

Figure 4.4. Biodistribution of mPEG-PLA (light gray), 10% Rho123-PEG-PLA(dark gray), and 10% Rho6G-PEG-PLA (black) particles in (a) liver, (b) kidneys, (c) heart, (d) lungs, (e) spleen, (f) brain and (g) blood. Rho6G-terminated particles present higher in the brain at 3h compared to mPEG and Rho123 terminated particles. * statistical significance compared to mPEG-PLA nanoparticles at $p < 0.01$

Table 4.2. Pharmacokinetic parameters for biodistribution data. Rho6G terminated nanoparticles have a longer half-life in plasma and higher accumulations and transfer rates in other organs.*blood AUC values represented as % ID-h/mL.

mPEG						
organ	$AUC_{0-\infty}$ (%ID-h/g)	AUC_{0-9} (%ID-h/g)	C_{max} (% ID/g)	t_{max} (h)	$t_{1/2}$ (h)	$k_{blood-tissue}$ (h^{-1})
Blood*	292.1	286.9	100.0	0	2.39 ± 0.11	-
Liver	15.2	14.7	2.9	3	-	0.085 ± 0.005
Kidneys	5.7	5.7	2.5	0.5	-	0.081 ± 0.004
Heart	3.8	3.8	1.9	0.5	-	0.081 ± 0.004
Lungs	10.2	10.2	3.1	0.5	-	0.082 ± 0.004
Spleen	187.2	187.2	29.0	9	-	0.19 ± 0.006
Brain	0.40	0.40	0.26	0.5	-	0.083 ± 0.004
10% Rho123						
organ	$AUC_{0-\infty}$ (%ID-h/g)	AUC_{0-9} (%ID-h/g)	C_{max} (% ID/g)	t_{max} (h)	$t_{1/2}$ (h)	$k_{blood-tissue}$ (h^{-1})
Blood*	259.7	245.8	100.0	0	2.21 ± 0.34	-
Liver	13.5	13.5	3.3	0.5	-	0.17 ± 0.03
Kidneys	5.6	5.6	1.9	0.5	-	0.15 ± 0.02
Heart	3.5	3.5	1.6	0.5	-	0.15 ± 0.02
Lungs	8.7	8.7	2.9	0.5	-	0.15 ± 0.02
Spleen	132.2	132.2	21.8	9	-	0.47 ± 0.06
Brain	0.35	0.35	0.24	0.5	-	0.14 ± 0.02
10% Rho6G						
organ	$AUC_{0-\infty}$ (%ID-h/g)	AUC_{0-9} (%ID-h/g)	C_{max} (% ID/g)	t_{max} (h)	$t_{1/2}$ (h)	$k_{blood-tissue}$ (h^{-1})
Blood*	267.4	267.4	100.0	0	5.88 ± 0.47	-
Liver	57.7	57.7	7.7	3	-	0.47 ± 0.2
Kidneys	26.9	24.5	3.7	3	-	0.31 ± 0.2
Heart	11.6	9.8	1.5	3	-	0.24 ± 0.2
Lung	31.4	24.6	4.2	0.5	-	0.32 ± 0.2
Spleen	154.8	154.8	19.6	9	-	1.6 ± 0.1
Brain	0.92	0.92	0.22	0.5	-	0.20 ± 0.1

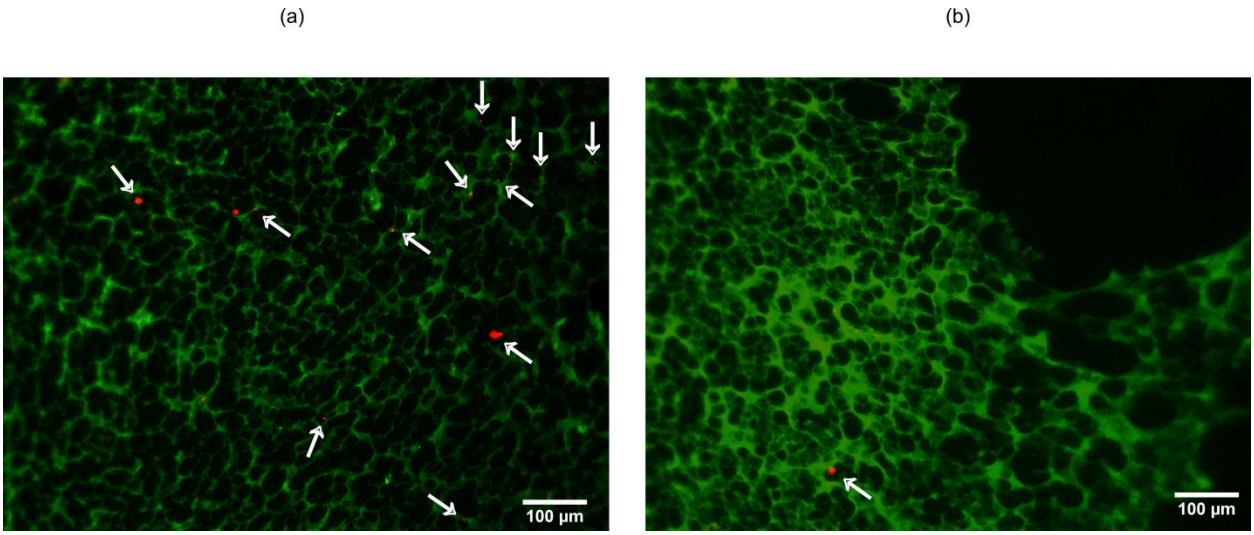

Figure 4.5. Representative brain tissue sections from mice injected with (a) Rho6G-PEG-PLA nanoparticles and (b) mPEG-PLA nanoparticles. Tissue autofluorescence is shown in green and the nanoparticles are in red. There are visibly particles in the brain after 3h in the Rho6G-PEG-PLA sample but only one aggregate visible in the mPEG-PLA sample. Arrows are pointing to nanoparticles in images.

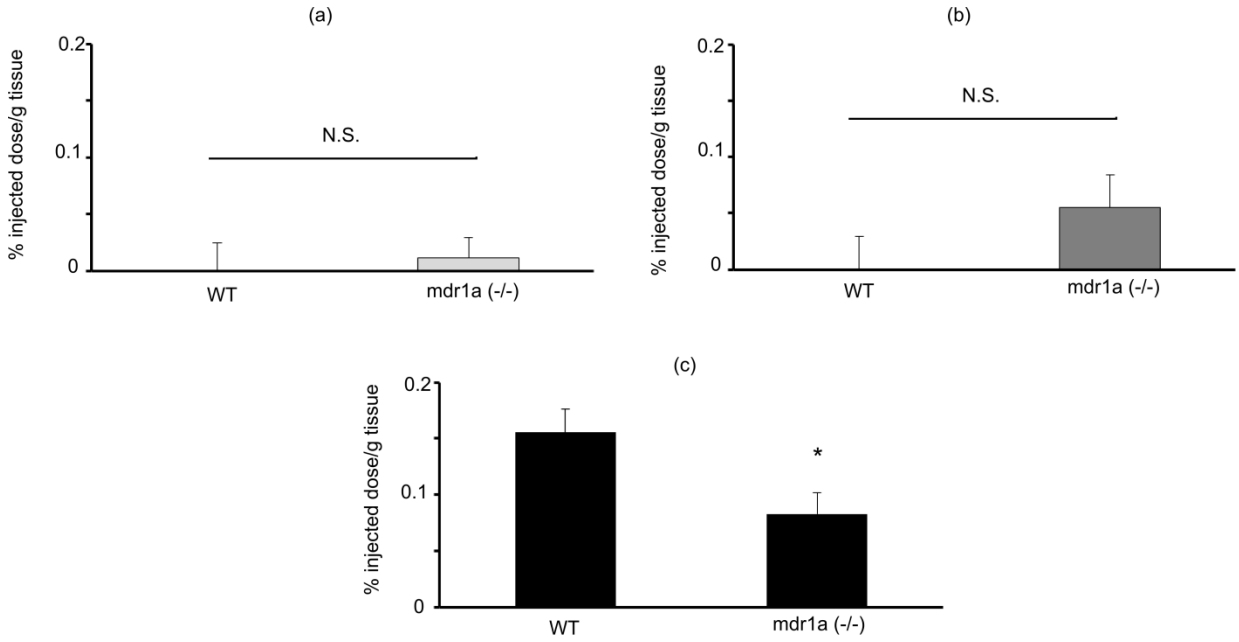

Figure 4.6. Brain accumulation of (a) mPEG-PLA nanoparticles, (b) Rho123-PEG-PLA nanoparticles and (c) Rho6G-PEG-PLA nanoparticles in WT mice compared to a P-gp knockout mouse, mdr1 (-/-), at 3h. There is a significant decrease seen in with the Rho6G-PEG-PLA particle accumulation in the P-gp knockout model. * represents statistical significance from the WT model at $p < 0.001$.

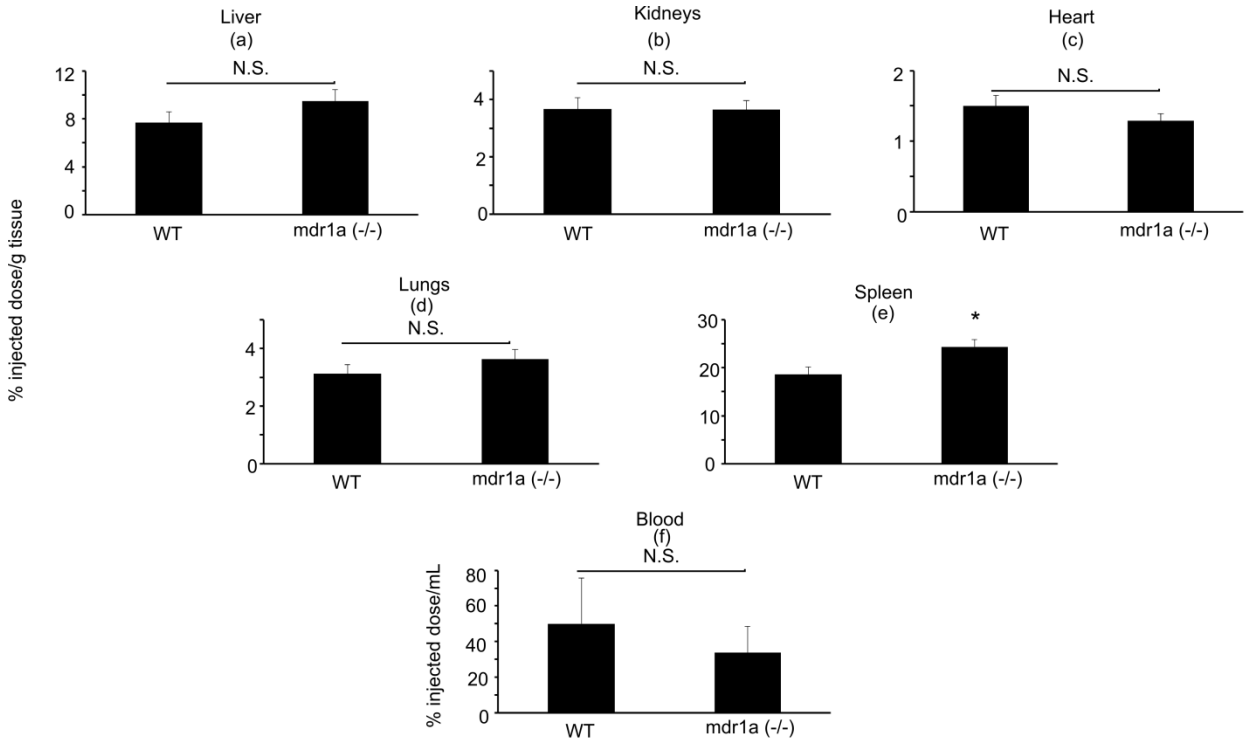

Figure 4.7. Comparision between WT mice to P-gp knockout mice of 6G-PEG-PLA accumulation at 3h in (a) liver, (b) kidneys, (c) heart, (d) lungs, (e) spleen and (f) blood. Only the spleen shows a significant difference between the two mouse models. * statistical significance from WT model at $p < 0.01$.

concentration in the brain could serve to rescue some compounds that have failed in the clinic due to poor side effect profiles. This is the focus of the work reported herein.

One of the traditional focuses for targeted drug delivery to the BBB has been to utilize endogenous transport systems in the BBB and exploit them for therapeutic purposes. Among the many receptor-ligand pairs, transferrin continues to be the most widely studied. The transferrin receptor was one of the first receptors utilized to shuttle therapeutic agents into the brain and has shown significant improvements in BBB targeting *in vivo* [17]. Recent reports have shown about 2 fold increase in rodent brain 4 and 2 hours after administration, respectively, with a transferrin conjugated nanoparticles [18,19]. Although transferrin-targeted systems have shown promise, there are challenges that are difficult to overcome. High transferrin concentrations exist naturally in the blood stream and compete with drug-loaded transferrin conjugates for the receptor [8]. Recent reports also suggest that in biologically relevant media, a protein corona can form around the targeting moiety and inhibit its receptor binding constant [9]. Therefore, targeted drug delivery systems have been developed using antibodies toward transferrin, however acute toxicity has occurred. Transferrin antibody fusion proteins reduce toxicity and are an attractive alternative "Trojan Horse" method of delivering therapeutic proteins [13], however targeted delivery of small molecule lipophilic drugs requires further development with this technology. Additionally, targeting insulin receptor has shown an increase in brain accumulation almost 10 fold compared to untargeted nanoparticles [20], however the effect on blood glucose levels was not discussed. Therefore, this study aimed to explore a new approach to increase the local concentration of therapeutics in the brain.

This study aimed to investigate whether the drug efflux transporter, P-gp, which is highly expressed in the endothelial cells that comprise the BBB, could be exploited to enhance the accumulation of nanoparticles in the brain. P-gp is an under-explored drug delivery target that is endogenous to the BBB endothelia, and actively transports small molecules from the CNS into the blood. The conceptual design of the targeting strategy is shown in Figure 4.1. Targeting was achieved by first creating a nanoparticle surface coated with P-gp substrates (Rho6G and Rho123-terminated nanoparticle

formulations), since previous findings determined that rhodamine-PEG conjugates still remained P-gp substrates [15]. Rhodamine presence on the nanoparticle surface was verified by fluorescence. Rho6G particles are more fluorescent than Rho123 terminated particles due to the greater quantum efficiency of Rho6G [21]; however, both are more fluorescent than methoxy terminated particles allowing characterization of their attachment on the nanoparticles. Because the degree of P-gp binding that would lead to effective nanoparticle accumulation in the brain was unknown, both Rho6G and Rho123 were used as targeting moieties, as they possess different affinities for P-gp. Rho6G is known historically to be the stronger P-gp substrate [22] and Rho6G-PEG-PLA nanoparticles showed the greatest brain accumulation in this study. Accumulation of Rho6G terminated particles was still high in the brain at 3 hours relative to controls and there was a loss of accumulation at the same time point in P-gp deficient knockout mice. These findings suggest that the Rho6G-terminated particles are able to effectively target P-gp, leading to an enhanced accumulation in the brain. Images of cryosectioned brain slices visually confirm the enhanced accumulation of the Rho6G-PEG-PLA nanoparticles in the brain relative to untargeted control nanoparticles. The favored sites of brain accumulation by these particles is an ongoing investigation and is the focus of a subsequent report. There are also higher accumulations of Rho6G terminated nanoparticles in the liver, kidneys, heart and lungs which can be attributed to the longer half-life of these particles as determined with pharmacokinetic modeling. It is unlikely that the higher accumulation in the brain of Rho6G terminated nanoparticles is also due to the greater half-life since there was a significant decrease in the P-gp knockout model.

There are also potential opportunities to modulate the nanoparticle locale at the cellular level. In the recent literature, the binding and internalization of nanoparticles containing agonists or antagonists of G protein coupled receptors was explored. Their results found that agonists bind and trigger cellular internalization, where antagonists bind and remain externally located at the cell surface [23]. These authors introduced the idea of a multi-ligand particle, which could also be an attractive approach for targeting P-gp. As Rho6G is not known to be an antagonist of P-gp, the literature suggests it would be internalized. P-gp has multiple binding pockets, only one of which involves rhodamine binding [24]. If a particle were

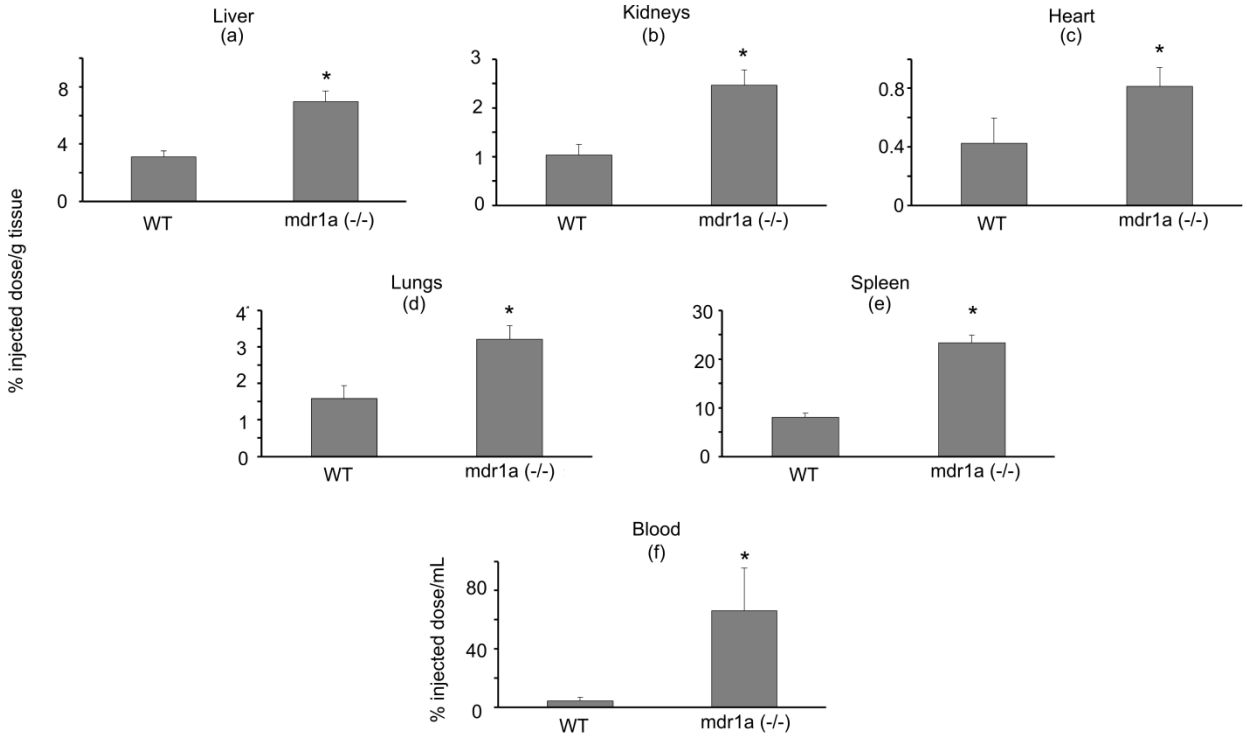

Figure 4.8. Comparison between WT mice to P-gp knockout mice of 123-PEG-PLA accumulation at 3h in (a) liver, (b) kidneys, (c) heart, (d) lungs, (e) spleen and (f) blood. All organs show a significant difference between the two mouse models. *statistical significance from WT model at $p < 0.01$.

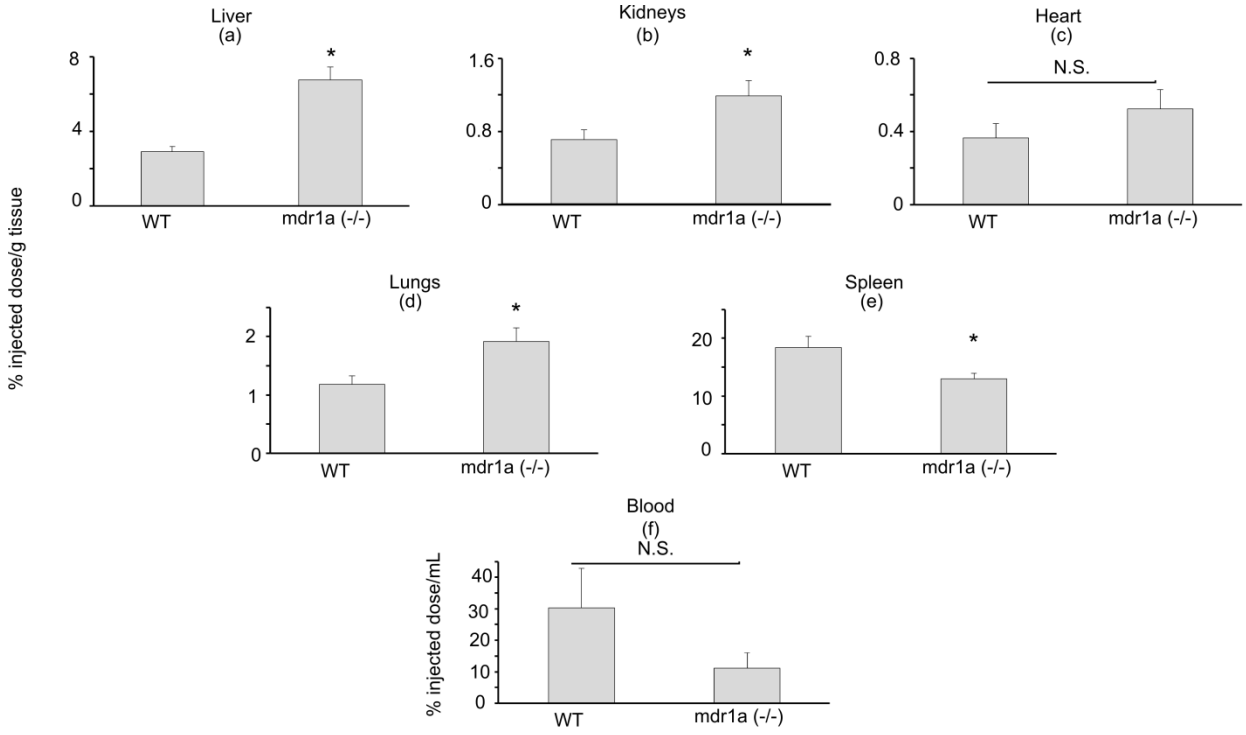

Figure 4.9. Comparison between WT mice to P-gp knockout mice of mPEG-PLA accumulation at 3h in (a) liver, (b) kidneys, (c) heart, (d) lungs, (e) spleen and (f) blood. Liver, kidneys, lungs and spleen show a significant difference between the two mouse models. * statistical significance from WT model at $p < 0.01$.

created that contained both agonist and an antagonist toward the opposite binding site, perhaps an increase in particle retention and an extension of therapeutic exposure time could be achieved.

4.5 Conclusion

Our findings define a unique approach toward enhancing the local concentration of drug-loaded nanoparticles in the brain. For the first time, substrates that are actively transported out of the brain were used as targeting agents to capture nanoparticles in the capillaries of the brain. Specifically, PEG-PLA nanoparticles containing Rho6G on the surface effectively targeted P-gp at the BBB and enhanced retention greater than 2-fold over untargeted controls. These results set the groundwork for a potentially new way to target the BBB by exploiting endogenously expressed proteins and expanding the types of targeting sites available at the BBB.

REFERENCES

(1) Pangalos, M. N., Schechter, L. E., and Hurko, O. (2007) Drug development for CNS disorders: strategies for balancing risk and reducing attrition. *Nat. Rev. Drug Discov. 6*, 521–532.

(2) Pardridge, W. M. (2007) Blood-brain barrier delivery. *Drug Discov. Today 12*, 54–61.

(3) Aryal, M., Arvanitis, C. D., Alexander, P. M., and McDannold, N. (2014) Ultrasound-mediated blood-brain barrier disruption for targeted drug delivery in the central nervous system. *Adv. Drug Deliv. Rev. 72*, 94–109.

(4) Lochhead, J. J., and Thorne, R. G. (2012) Intranasal delivery of biologics to the central nervous system. *Adv. Drug Deliv. Rev. 64*, 614–628.

(5) Pardridge, W. M. (2003) Blood-brain barrier drug targeting: the future of brain drug development. *Mol. Interv. 3*, 90–105, 51.

(6) Lu, C. T., Zhao, Y. Z., Wong, H. L., Cai, J., Peng, L., and Tian, X. Q. (2014) Current approaches to enhance CNS delivery of drugs across the brain barriers. *Int. J. Nanomedicine 9*, 2241–2257.

(7) Ulbrich, K., Hekmatara, T., Herbert, E., and Kreuter, J. (2009) Transferrin- and transferrin-receptor-antibody-modified nanoparticles enable drug delivery across the blood-brain barrier (BBB). *Eur. J. Pharm. Biopharm. 71*, 251–256.

(8) Qian, Z. M., Li, H., Sun, H., and Ho, K. (2002) Targeted drug delivery via the transferrin receptor-mediated endocytosis pathway. *Pharmacol. Rev. 54*, 561–587.

(9) Salvati, A., Pitek, A. S., Monopoli, M. P., Prapainop, K., Bombelli, F. B., Hristov, D. R., Kelly, P. M., Åberg, C., Mahon, E., and Dawson, K. a. (2013) Transferrin-functionalized nanoparticles lose their targeting capabilities when a biomolecule corona adsorbs on the surface. *Nat. Nanotechnol. 8*, 137–143.

(10) Gupta, Y., Jain, A., and Jain, S. K. (2007) Transferrin-conjugated solid lipid nanoparticles for enhanced delivery of quinine dihydrochloride to the brain. *J. Pharm. Pharmacol. 59*, 935–940.

(11) Ulbrich, K., Knobloch, T., and Kreuter, J. (2011) Targeting the insulin receptor: nanoparticles for drug delivery across the blood-brain barrier (BBB). *J. Drug Target. 19*, 125–132.

(12) Loureiro, J. a, Gomes, B., Coelho, M. a N., do Carmo Pereira, M., and Rocha, S. (2014) Targeting nanoparticles across the blood-brain barrier with monoclonal antibodies. *Nanomedicine (Lond). 9*, 709–722.

(13) Pardridge, W. M. (2015) Blood–brain barrier drug delivery of IgG fusion proteins with a transferrin receptor monoclonal antibody. *Expert Opin. Drug Deliv. 12*, 207–222.

(14) Iwahashi, T., Okochi, E., Ariyoshi, K., Watabe, H., and Aã-na, E. (1993) Specific Targeting and Killing Activities of Anti-P-Glycoprotein Monoclonal Antibody MRK16 Directed against Intrinsically Multidrug-resistant Human Colorectal Carcinoma Cell Lines in the Nude Mouse Model Specific Targeting and Killing Activities of Anti-P. *Cancer Res. 53*, 5475–5482.

(15) Crawford, L., and Putnam, D. (2014) Synthesis and Characterization of Macromolecular Rhodamine Tethers and Their Interactions with P-Glycoprotein. *Bioconjug. Chem. 25*, 1462–1469.

(16) Ornatsky, O., Baranov, V., Shen, L., Abdelrahman, A., and Winnik, M. A. (2007) Lanthanide-containing polymer nanoparticles for biological tagging applications : nonspecific endocytosis and cell adhesion. *J. Am. Chem. Soc. 129*, 13653–13660.

(17) Lajoie, J. M., and Shusta, E. V. (2015) Targeting Receptor-Mediated Transport for Delivery of Biologics Across the Blood-Brain Barrier. *Annu. Rev. Pharmacol. Toxicol. 55*, 613–631.

(18) Gan, C. W., and Feng, S. S. (2010) Transferrin-conjugated nanoparticles of Poly(lactide)-d- aplha-Tocopheryl polyethylene glycol succinate diblock copolymer for targeted drug delivery across the blood-brain barrier. *Biomaterials 31*, 7748–7757.

(19) Huang, R.-Q., Qu, Y.-H., Ke, W.-L., Zhu, J.-H., Pei, Y.-Y., and Jiang, C. (2007) Efficient gene delivery targeted to the brain using a transferrin-conjugated polyethyleneglycol-modified polyamidoamine dendrimer. *FASEB J. 21*, 1117–1125.

(20) Shilo, M., Motiei, M., Hana, P., and Popovtzer, R. (2014) Transport of nanoparticles through the blood-brain barrier for imaging and therapeutic applications. *Nanoscale 6*, 2146–2152.

(21) Kubin, R. F., and Fletcher, A. N. (1982) Fluorescence quantum yields of some rhodamine dyes. *J. Lumin. 27*, 455–462.

(22) Eytan, G. D., Regev, R., Oren, G., Hurwitz, C. D., and Assaraf, Y. (1997) Efficiency of P-glycoprotein-mediated exclusion of rhodamine dyes from multidrug-resistant cells is determined by their passive transmembrane movement rate. *Eur. J. Biochem. 248*, 104–112.

(23) Hild, W., Pollinger, K., Caporale, A., Cabrele, C., Keller, M., Pluym, N., Buschauer, A., Rachel, R., Tessmar, J., Breunig, M., and Goepferich, A. (2010) G protein-coupled receptors function as logic gates for nanoparticle binding and cell uptake. *Proc. Natl. Acad. Sci. U. S. A. 107*, 10667–10672.

(24) Loo, T. W., Bartlett, M. C., and Clarke, D. M. (2003) Methanethiosulfonate derivatives of rhodamine and verapamil activate human P-glycoprotein at different sites. *J. Biol. Chem. 278*, 50136–41.

CHAPTER 5

CONCLUSIONS AND FUTURE RECOMMENDATIONS

Drug delivery to the CNS continues to be one of the greatest hurdles in drug development for neurological diseases. The challenge can be attributed to the exclusive passage of molecules across the blood brain barrier (BBB). Receptor mediated targeting is a well-studied strategy to facilitate macromolecular transport across the BBB; however it has shown little translation from *in vivo* animal models to human clinical trials. Unfortunately, the leading receptor mediated systems in existence suffer from low efficiency and systemic safety concerns. Therefore, there is a need for the development of new ways to target drug delivery system to the CNS. This study aimed to accomplish targeted nanoparticle delivery using a novel receptor target, P-glycoprotein (P-gp).

A targeted drug delivery system to exploit P-gp at the BBB was designed, synthesized and tested for efficiency. PEG-rhodamine conjugates were made, and their ability to interact with P-gp was evaluated *in vitro*. FACS analysis showed decreased accumulation in a P-gp expressing cell line for all rhodamines tested, suggesting the PEG-rhodamine conjuagtes remained P-gp substrates. Using three different rhodamine variants, an affinity relationship was also established with rhodamine-PEG conjugates and P-gp. A mechanistic analysis using increasing concentrations of verapamil, a P-gp inhibitor, was conducted and showed the accumulation of rhodamine-PEG conjugates in P-gp expressing cells increased as verapamil concentration increased. These results collectively led to the conclusion that rhodamines conjugated to PEG still remained P-gp substrates. Rhodamine 6G (Rho6G)-PEG had the greatest P-gp affinity, followed by rhodamine 123 (Rho123)-PEG and rhodamine B (RhoB)-PEG. This is the same trend for the native dyes.

To evaluate the efficiency of the drug delivery system, a method for detection of PLA-PEG nanoparticles *in vivo* was needed. *In vivo* detection can be challenging due to the high background caused by the intrinsic autofluorescence of tissues. Traditional methods to overcome the autofluorescent background are either unsafe (e.g., radiolabels) or unstable (e.g., near-IR probes). This study utilized

lanthanide chelates, particularly a europium chelate ($Eu(NTA)_3$), for its large Stokes shift and time resolved fluorescence properties. Using mPEG-PLA nanoparticles encapsulating $Eu(NTA)_3$, detection above background with high sensitivity was possible. Although there were quenching effects of the europium chelate that decreased the signal over time, the signal decay followed a second order degradation and corrections for this decay could be made by linearization of the curve. The iron (Fe^{+3}) in various tissues can also displace the Eu^{+3} in the chelate and quench signal as well, but the extent of quenching from each tissue of interest is quantifiable and was therefore considered in calculating the % injected dose. Ultimately, a sensitive and useful method for the detection of PLA-PEG nanoparticles was developed and applied *in vivo*.

The method of detecting PLA-PEG nanoparticles using $Eu(NTA)_3$ was then applied to quantify the targeting efficiency of Rho6G-PEG-PLA, Rho123-PEG-PLA, and mPEG-PLA nanoparticles. Rho6G-PEG-PLA nanoparticles showed the greatest accumulation in the brain compared to the other particle types. The most significant difference in Rho6G-PEG-PLA particle accumulation was seen at 3h post injection. The role of P-gp in increased brain concentration of Rho6G-PEG-PLA was elucidated by testing particle accumulation at 3h in a P-gp deficient mouse. There was a significant decrease in accumulation of Rho6G-PEG-PLA nanoparticles in P-gp deficient mice, providing evidence that Rho6G-PEG-PLA nanoparticles can collect in the brain due to interactions with P-gp.

While this work presented the initial finding that Rho6G-PEG-PLA nanoparticles can target P-gp at the BBB, future work should focus on expanding the mechanistic understanding and potential clinical utility of the present technology. A few major shortcomings of the presented work are the limit in particle detection up to 9 hours, lack of distribution within the brain, and the systemic accumulation of these particles. Due to the degradation of the fluorescent signal of the europium chelate doped nanoparticles used in this study, detection beyond 9 hours was not a possibility. A chelate that contains different antennas to better protect from water quenching could provide information of particle accumulation beyond 9 hours, which could have future impact when choosing the appropriate drug for a desired efficacy model.

Although Rho6G-PEG-PLA nanoparticles were able to target P-gp at the BBB, more detailed accumulation profiles within different parts of the brain could provide useful information to further the technology to a disease efficacy model. The BBB does not exist uniformly throughout all parts of the brain and thus, there may be particular disease models better suited for the Rho6G-PEG-PLA targeted drug delivery system. A very preliminary look into tissue distribution was performed in this work with imaging of brain tissue slices, however, this was not done for particular portions of the brain. Applying this same analysis to multiple mice within known brain structures could provide evidence into portions that are more widely targeted and tissue penetration within those compartments. Once compartmental accumulation is understood, efficacy tests can determine the potential clinical utility of the system.

Given the greater systemic distribution of the Rho6G terminated particles, safety in vital organs should also be a consideration moving forward. As previously discussed, conjugation of targeting moieties often changes the biodistribution of the system and can lead to negative targeting. This has been a major challenge associated with the translation of previously developed receptor mediated approaches into clinical success and should be addressed to further the current technology. Exploring the underlying cause of increased accumulation in vital organs could lead to a prevention method which would further enhance not only the targeted drug delivery strategy of this work, but also previously reported systems.

As tissue penetration was only initially explored in this study, there could be even greater benefits of targeting P-gp if this system is used in conjunction with other targeting strategies. Although P-gp is found in intracellular compartments, there is no evidence that it can translocate Rho6G-PEG-PLA nanoparticles across cells. Therefore, the use of a cell penetrating peptide combined with this technology may further enhance the targeting effects by allowing penetration into the tissue from the BBB.

Alternative to CNS drug delivery, Rho6G-PEG-PLA nanoparticles could also be applied to targeted drug delivery to P-gp expressing cancers. Initial tumor xenograft models with MDA-435/LCC6 MDR and WT cells were established earlier in this work (Appendix I). The biodistribution of rhodamine-terminated nanoparticles can be determined using methods similar to this work. Initial studies to determine any inhibitory effects of rhodamine-terminated PLA-PEG nanoparticles have been done *in*

vitro (Appendix I), and show only minor inhibition of P-gp when delivering doxorubicin. Therefore, chemotherapy choice in a cancer model will be important and should be screened *in vitro*.

Lastly, other substrates of P-gp could also be considered for targeted drug delivery. Rhodamine was used here as a model substrate, but with the large numbers of known P-gp substrates, there are many possibilities. A system could also be developed to include an inhibitor instead of a substrate. This could enable potential delivery of therapeutics that are P-gp substrates. Previous attempts in the literature to co-deliver therapeutics with P-gp inhibitors have proven systemically toxic due to the drug/inhibitor combination. By tethering the inhibitor to a nanoparticle it could reduce cytotoxic effects. Appendix II includes information about an mPEG-quinidine conjugate that could be adapted into a similar nanoparticle system and used to deliver P-gp substrates to the BBB as quinidine is a well-known P-gp inhibitor. Once further developed into a particle platform, quinidine-PEG-PLA nanoparticles can be tested first *in vitro* for their ability to deliver cytotoxic P-gp substrates and then *in vivo*. The ability to not only target P-gp but also inhibit it in a potentially safer manner is an attractive approach to drug delivery of P-gp substrates.

To summarize, this work presented an initial finding that Rho6G-PEG-PLA nanoparticles could target P-gp at the BBB. Further investigation into the downfalls of this particular system can enhance the positive targeting of this system, while decreasing any negative targeting. Extension to cancer models are possible and increase the clinical importance of Rho6G-PEG-PLA nanoparticles. This model system can also be used to further develop P-gp inhibitor containing nanoparticles that enable delivery of P-gp substrates.

APPENDIX I

INITIAL CANCER MODEL RESULTS

AI.1 Introduction

Cancer is the second most common cause of death in the United States and according to the American Cancer Society there will be over 1 million new cases of cancer in 2013.[1] A common issue in the treatment of cancerous tumors is the development of drug resistance. There are many causes of drug resistance, but the current study focuses on the energy dependent efflux of therapeutics.[2] Efflux of such drugs is caused by membrane transport proteins of the ATP-binding cassette (ABC) family. The general process of drug efflux caused by these proteins can be described in three steps: 1) first, the drug crosses into the cell membrane, 2) second, once in the membrane, the drug (substrate) is recognized by the membrane transport protein and 3) third, after recognition, the drug is expelled from the cell by the protein. The ABC family of proteins has an affinity to a wide variety of substances, leading to expulsion of various classes of drugs and thus resistance to a multitude of substrates. This phenomenon is termed multi drug resistance (MDR)[3] and is the cause of the difficulty associated with treating cancerous tumors. One member of the ABC family found in human cell lines is P-glycoprotein (P-gp) and its overexpression has been linked to MDR in various cancers.[4] One possible solution to combat P-gp overexpression in cancerous tumors is to exploit expression of the protein by creating a targeted drug delivery vehicle toward the protein. Therefore, the current technology of this work can be extended to P-gp expressing tumors. The ability for the designed nanoparticles to deliver a common chemotherapeutic and P-gp substrate, doxorubicin, has been explored *in vitro*. Also, initial tumor xenograft models with MDA-435/LCC6 WT and MDR cell lines have been developed.

AI.2 Materials and Methods

AI.2.1 Doxorubicin loaded nanoparticles. mPEG-PLA, Rho123-PEG-PLA, and Rho6G-PEG-PLA copolymers were synthesized using the same methods reported in section 4.2.4. Doxorubicin (dox) was dissolved in methanol at 1 mg/mL. 100 mg of mPEG-PLA was dissolved in 2 mL dichloromethane (DCM) and 500 µL of dox solution was added and the solution was vortexed. 8 mL of acetone was then added, the solution vortexed, and added dropwise into stirring milliQ water. The organic solvents were removed by rotary evaporation and the nanoparticles collected by ultracentrifugation using a Bruker LE-80 ultracentrifuge at 20,000 rpm for 30 minutes. The nanoparticles in the pellet were washed twice with milliQ water and resuspended in a final volume of 1 mL of milliQ water. Poloxamer 188 (20 µL of 10% solution) was added prior to lyophilization overnight. For 10% Rho6G-PEG-PLA and 10% Rho123-PEG-PLA nanoparticles the same procedure was followed but with 90 mg of mPEG-PLA and 10 mg of Rho6G-PEG-PLA or Rho123-PEG-PLA, respectively. Unloaded nanoparticles were made with the same protocols without addition of doxorubicin (see Chapter 4 for details).

A 1 mg/mL solution of the nanoparticle solutions were made with milliQ water and sonicated for 10 minutes. After sonication the solutions were filtered through a 0.45 µm filter and size and polydispersity were measured using a Malvern NanoZS (United Kingdom). Encapsulation efficiency was calculated by comparison of the fluorescence of 1 mg/mL nanoparticle solution in acetone to 0.005 mg/mL solution of doxorubicin in acetone at an excitation of 480 nm and emission of 580 nm. Fluorescence of unloaded nanoparticles under the same excitation and emission were subtracted from the obtained signal.

AI.2.2 Cytotoxicity of MDA-435/LCC6 cells after administration of dox. MDA-435/LCC6 MDR and MDA-435/LCC6 WT cells were maintained at 37 °C with 5% CO_2 in Richter's modified MEM (IMEM) containing L-glutamine, phenol red, 10% fetal bovine serum and 1% penicillin/streptomycin in 25 cm^2 canted T-flasks. Each well of a 96 well plate were seeded with 7500 cells and grown for 48 hours.

After 48 hours, cells were washed and doxorubicin, nanoparticles encapsulating doxorubicin (mPEG-PLA, Rho123-PEG-PLA and Rho6G-PEG-PLA), or unloaded nanoparticles were added at various concentrations in IMEM in a total volume of 100 µL for each well. Cells were incubated with dox solutions for 24 hours. After incubation, dox and nanoparticle containing media was removed, cells were washed, and 10 µL of MTT (1 mg/mL) in 100 µL of PBS was added. After 4 hours of incubation, 200 µL of DMSO was added to dissolve the formazan crystals. The adsorption of each well was read on a UV-vis plate reader at 570 nm.

AI.2.3 Cell and xenograft model growth curves. Cell growth curves were made by seeding 100,000 cells in each well of a 6 well plate. Cells were removed after 1, 2, 3, 5, or 7 days of growth and counted using a hemocytometer. Each timepoint was performed in triplicate.

Xenografts with both MDA-435/LCC6 MDR and MDA-435/LCC6 WT cells were developed in 6 week old immunodeficient Nu/Nu mice. 1-2 million cells were injected subcutaneously into the back haunches of 36 mice for each cell type. Tumor measurements were taken with vernier calipers. The volume was calculated using a modified ellipsoidal equation[5–7] (Equation 1).

$$V = 0.5 * l * w^2 \qquad \text{(Eq. 1)}$$

AI.3 Results and Discussion

AI.3.1 Doxorubicin loaded nanoparticles. Doxorubicin nanoparticles were successfully made. There was no free doxorubicin visible in all the washes during ultracentrifugation (not shown). Particle size, PDI, and encapsulation efficiency (EE) are shown in Table AI.1. All particles are about the same size and relatively mono-disperse. Less doxorubicin was encapsulated in mPEG terminated nanoparticles than Rho123 and Rho6G terminated nanoparticles.

Table AI.1. Characteristics of doxorubicin loaded mPEG-PLA, Rho123-PEG-PLA and Rho6G-PEG-PLA nanoparticles

Particle type	**Size (nm)**	**PDI**	**EE (%)**
mPEG-PLA	132.8 ± 5.2	0.078 ± 0.01	41.5 ± 3.2
10% Rho123-PEG-PLA	155.3 ± 16	0.087 ± 0.01	72.8 ± 4.4
10% Rho6G-PEG-PLA	138.1 ± 4.6	0.076 ± 0.01	88.5 ± 5.9

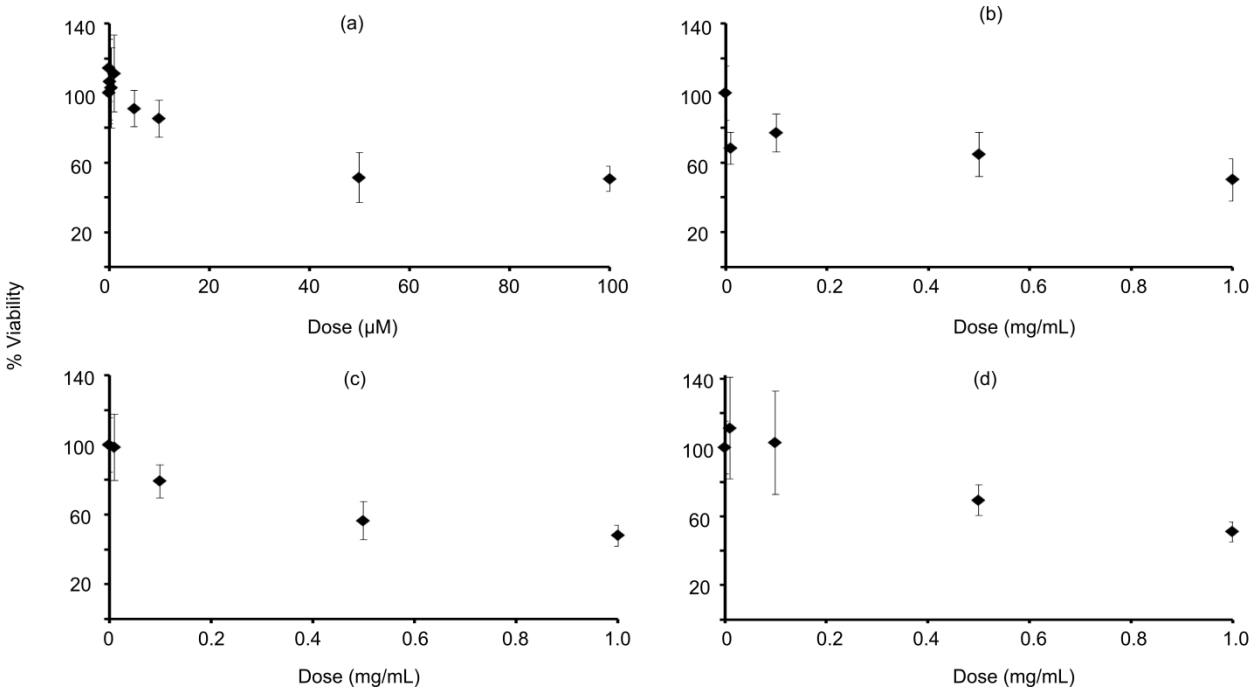

Figure AI.1. Cytotoxicity of MDA-435/LCC6 WT cells with either (a) doxorubicin alone or doxorubicin loaded into (b) mPEG-PLA, (c) Rho123-PEG-PLA or (d) Rho6G-PEG-PLA nanoparticles

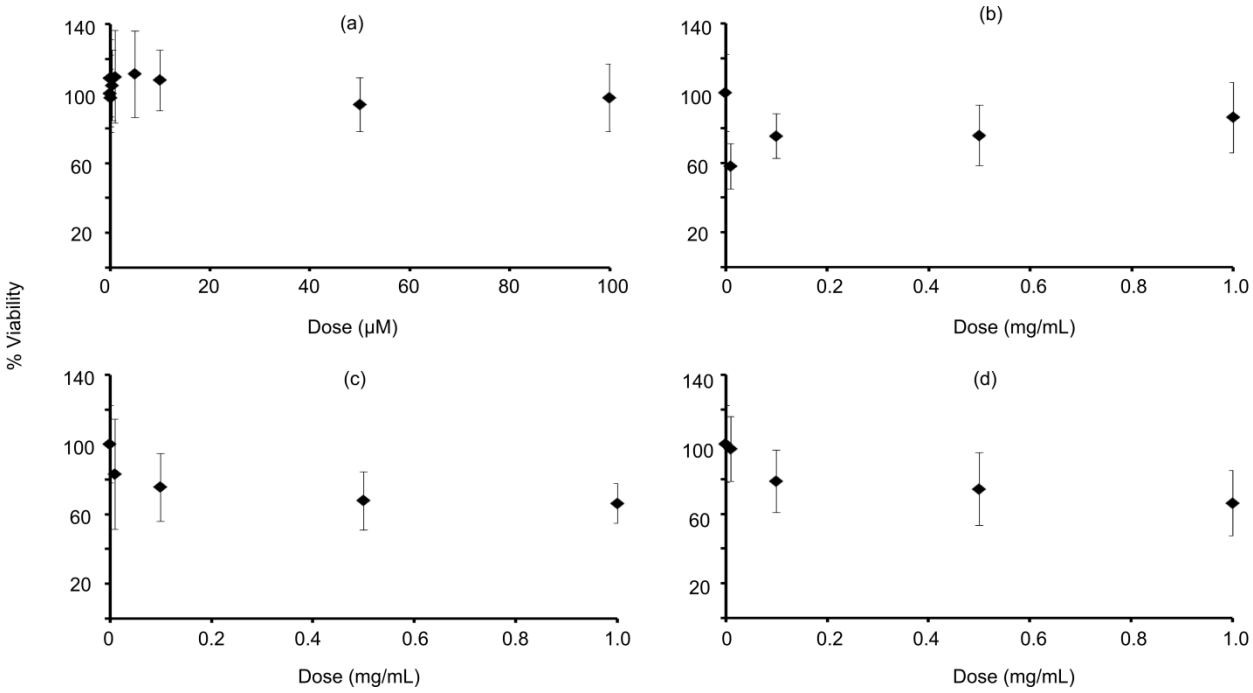

Figure AI.2. Cytotoxicity of MDA-435/LCC6 MDR cells with either (a) doxorubicin alone or doxorubicin loaded into (b) mPEG-PLA, (c) Rho123-PEG-PLA or (d) Rho6G-PEG-PLA nanoparticles

Table AI2. Conversion of mg/mL of particles to concentration of doxorubicin

	µM dox		
mg/ml particle	**mPEG**	**123**	**6G**
1	3.81	6.70	8.14
0.5	1.91	3.35	4.07
0.1	0.38	0.67	0.81
0.01	0.038	0.067	0.081
0	0.00	0.00	0.00

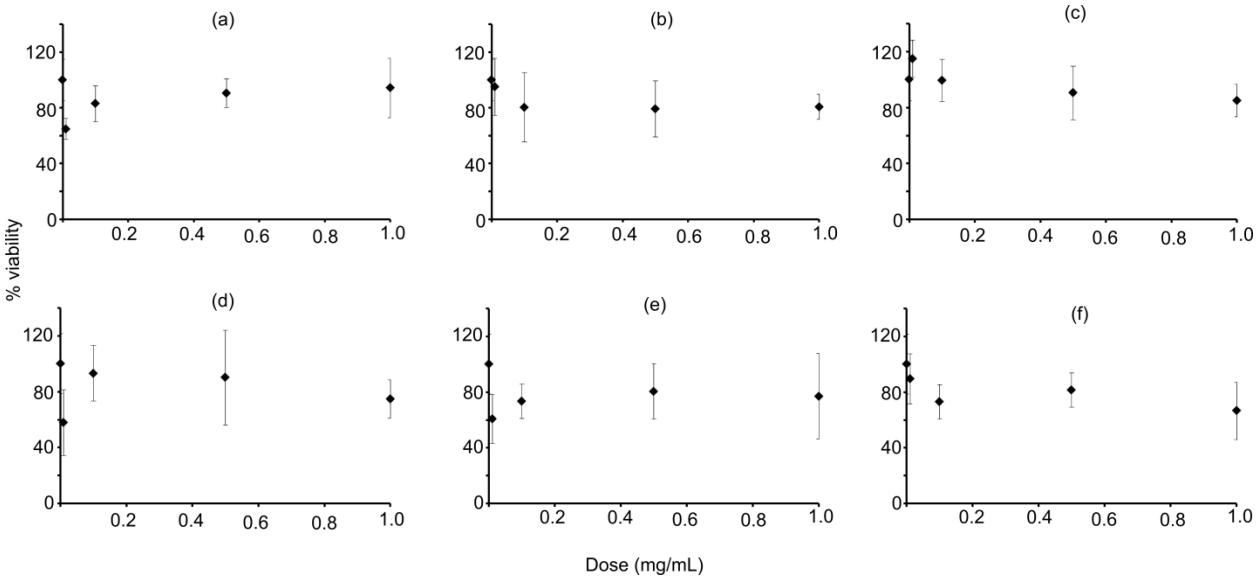

Figure AI.3. Cytotoxicity on MDA-435/LCC6 WT (a,b,c) or MDA-435/LCC6 MDR (d,e,f) cells with either (a and d) unloaded mPEG-PLA, (b and e) unloaded Rho123-PEG-PLA or (c and f) Rho6G-PEG-PLA nanoparticles

AI.3.2 Cytotoxicity of MDA-435/LCC6 cells after administration of dox. Cytotoxicity curves of dox alone and doxorubicin encapsulated in either mPEG, Rho123 or Rho6G terminated nanoparticles for WT cells are shown in Figure AI.1 and for MDR cells are shown in Figure AI.2. To compare nanoparticle concentration to doxorubicin dose, table AI.2 shows the conversion from particle concentration (mg/mL) to doxorubicin dose (μM) using the encapsulation efficiency. All solutions show similar cell death in WT cells, which is expected. There is greater cell death in MDR cells with the nanoparticle platforms. Both Rho123 and Rho6G terminated nanoparticles show slightly greater cell death than mPEG terminated nanoparticles at higher concentrations, but there is not a drastic difference. This could be due to the roughly 2 times increase in doxorubicin concentration in Rho terminated particles compared to mPEG terminated. There could be a very slight inhibitory effect on P-gp from the Rho terminated nanoparticles but not significant enough to deliver P-gp substrate chemotherapeutics. The effect of unloaded nanoparticles on both WT and MDR cells were also explored and the results are shown in Figure AI.3. The particles alone are not cytotoxic to the WT cells and the patterns in the MDR cells are similar to the doxorubicin loaded results. Rho123 and Rho6G terminated nanoparticles have a slightly higher cytotoxicity on MDR cells than mPEG terminated nanoparticles. However, the doxorubicin loaded nanoparticles do show slightly more cell death than unloaded nanoparticles for MDR cells.

AI.3.3 Cell and xenograft model growth curves. Growth curves for both *in vitro* cell culture and xenograft model of MDA-435/LCC6 WT and MDR cells are shown in Figure AI.3. It appears there is slightly slower growth of MDR cells *in vitro*, however, this is not significant. In the xenograft model the WT cell line appears to have a higher measurement at 7 days post injection and reaches the critical volume for this study sooner than MDR cells. However once both cell lines reach a volume between 50 and 100 mm^3 growth becomes more rapid. The WT cell line was injected at $2x10^6$ cells per mouse while the MDR cell line was injected at $1x10^6$ cells per mouse. This could be the cause of the WT cell line showing larger volumes at 7 days post injection.

AI.4 Conclusions

The designed Rho-PEG-PLA nanoparticle system is not sufficient for delivering P-gp substrate drugs. However, this does not mean that it won't be effective at targeting P-gp expressing cancers with chemotherapeutics that are non-P-gp substrates. A xenograft model is possible with these cells, but injection of the same initial cell count is necessary to have consistent growth rates. These findings can set up future work to assess targeting efficiency and efficacy for P-gp expressing cancers in the future.

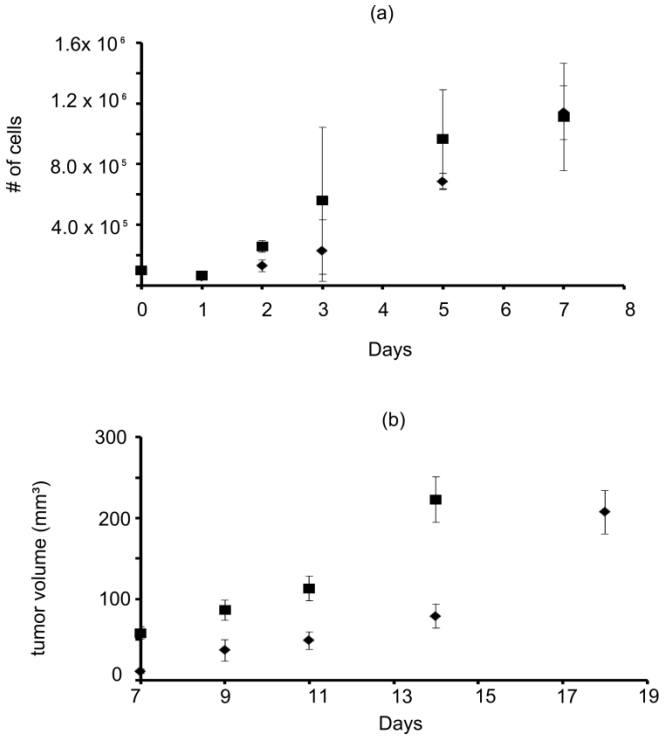

Figure AI.3. Growth curves of MDA-435/LCC6 (a) cells and (b) tumors xenografts in a nude mouse model. (■) WT cells and (◆) MDR cells.

REFERENCES

(1) American Cancer Society. *Cancer Facts Fig. 2013*.

(2) Szakács, G., Paterson, J. K., Ludwig, J. a, Booth-Genthe, C., and Gottesman, M. M. (2006) Targeting multidrug resistance in cancer. *Nat. Rev. 5*, 219–234.

(3) Eckford, P. D. W., and Sharom, F. J. (2009) ABC efflux pump-based resistance to chemotherapy drugs. *Chem. Rev. 109*, 2989–3011.

(4) Sharom, F. J., Yu, X., Chu, J. W., and Doige, C. a. (1995) Characterization of the ATPase activity of P-glycoprotein from multidrug-resistant Chinese hamster ovary cells. *Biochem. J. 308*, 381–90.

(5) Euhus, D. M., Hudd, C., LaRegina, M. C., and Johnson, F. E. (1986) Tumor measurement in the nude mouse. *J. Surg. Oncol. 31*, 229–34.

(6) Tomayko, M. M., and Reynolds, C. P. (1989) Determination of subcutaneous tumor size in athymic (nude) mice *. *Cancer Chemother. Pharmacol. 24*, 148–154.

(7) Jensen, M. M., Jørgensen, J. T., Binderup, T., and Kjaer, A. (2008) Tumor volume in subcutaneous mouse xenografts measured by microCT is more accurate and reproducible than determined by 18F-FDG-microPET or external caliper. *BMC Med. Imaging 8*, 16.

APPENDIX II

INITIAL SYNTHESIS AND CHARACTERIZATION OF MPEG-QUINIDINE

AII.1 Introduction

P-gp expression at the BBB and in MDR cancers has caused difficulty in drug delivery due to the large number of therapeutics that are also P-gp substrates. Therefore, a significant effort has been made to identify substances that have inhibitory functions on P-gp [1]. Discoveries have been made with both P-gp substrates[2] and antibodies[3,4]. Although many combinations of inhibitor/chemotherapeutics have gone into phase III clinical trials, the majority have failed to demonstrate significant clinical utility [5–7]. Conjugation of an inhibitor directly to a nanoparticle may be a solution to delivering P-gp substrates and reducing systemic side effects. One proposed method is to utilize a known P-gp inhibitor, quinidine, conjugated to a PEG-PLA nanoparticle. Preliminary methods have been developed and characterized to synthesize an mPEG-quinidine conjugate that can be tested in future *in vitro* inhibition studies. Previous literature has developed mPEG-quinidine conjugation through a glycine linker [8,9]. Both direct conjugation (no linker) and conjugation with a linker were attempted.

AII.2 Materials and Methods

AII.2.1 Direct conjugation of mPEG-quinidine. In 7 mL of dichloromethane (DCM), 0.05 mmol mPEG, 5 mmol N,N'-Dicyclohexylcarbodiimide (DCC), and 0.21 mmol 4-Dimethylaminopyridine (DMAP) were added and stirred for 20 minutes. Quinidine (0.15 mmol) was dissolved in 3 mL DCM and added after 20 minutes. The reaction was left to stir overnight. After the reaction was complete any solids that had formed were filtered and the product was crashed out in diethyl ether. The reaction scheme can be found in Figure AII.1. ^{1}H NMR spectra were taken for reactants and products (Figure AII.2). Diffusion ordered NMR was done for the product. A Stejskal-Tanner plot was made to interpret the results (Figure AII.3).

AII.2.2 Conjugation of mPEG-quindine with a glycine linker. First, boc-glycine-OH was reacted with quinidine. 9.1 mmol of boc-glycine-OH was dissolved in 10 mL DCM and mixed with 9.2 mmol DCC in 10 mL of DCM. The two solutions stirred for 1 h on ice under argon. After 1 h a 100 mL DCM solution containing 4.6 mmol quinidine and 0.5 mmol DMAP was added dropwise. The reaction was brought back to room temperature and allowed to react for 24 hours. Once the reaction was complete, the solution was filtered and 0.5 mL acetic acid was added. The solution was filtered again and the solvent was evaporated. The remaining substance was taken up in 30 mL acetone, filtered, and solvent was evaporated again. The residual was dissolved in 20 mL DCM and placed in a separatory funnel where it was washed with 2 mL of saturated sodium bicarbonate 4 times, dried over magnesium sulfate and then dried under vacuum.

Deprotection of boc-glycine-quinidine was accomplished by dissolving 1 g in 10 mL DCM and adding 10 mL trifluoroacetic acid (TFA) and allowing the solutions to mix for 30 minutes. The solution was then rotary evaporated to an oily residue. This residue was taken up in 20 mL DCM and washed with 2 mL of saturated sodium bicarbonate 3 times in a separatory funnel. It was then dried over magnesium sulfate, rotary evaporated, and vacuum dried.

Reaction of mPEG-COOH and glycine-quinidine was then performed. Glycine-quinidine (0.07 mmol) and mPEG-COOH (0.034 mmol) were dissolved in DCM (~ 10 mL). These two solutions stirred for 10 minutes, then a saturated DMSO solution of 0.07 mmol 4-(4,6-dimethoxy-1,3,5-triazin-2-yl)-4-methylmorpholinium chloride (DMTMM) and 0.07 mmol 4-methyl morpholine (NMM) were added dropwise. The reaction was left stirring for two days under argon. Once the reaction was complete, the product was crashed out in diethyl ether. The overall reaction scheme can be found in Figure AII.4. ^{1}H NMR was taken for all reactants, intermediates and products (Figures AII.5 and AII.6).

AII.3 Results and Discussion

AII.3.1. Direct conjugation of mPEG-quinidine. ^{1}H NMR of mPEG-quinidine (Figure AII.2) shows the PEG associated peaks around 3.17 and 3.5 ppm and quinidine peaks in the aromatic region. However, when integrated, there appeared to be more quinidine than PEG, suggesting a more effective purification protocol is needed. The diffusion ordered NMR shows that some quinidine was conjugated to PEG, but at some gradient strengths quinidine does not behave like the polymer. When percent conjugation was performed at a higher gradient strength (no signal for small molecules), it appeared that ~ 70% quinidine was attached to the PEG. Therefore, this reaction may be successful with an alternative purification protocol.

AII.3.2. Conjugation of mPEG-quinidine with a glycine linker. It has been suggested that the glycine linker can reduce steric hindrance of quinidine and allow for more efficient conjugation [9]. To accomplish this conjugation, first boc-glycine-OH had to be reacted with quinidine to form boc-glycine-quinidine (Figure AII.4A). ^{1}H NMR (Figure AII.5) shows the aromatic peaks associated with quinidine along with a peak around 1ppm from the boc group. Upon deprotection (Figure AII.4B), the peak around 1ppm (boc group) disappears on ^{1}H NMR, indicating that deprotection was successful. The deprotected product was then reacted with mPEG-COOH to produce an mPEG-glycine-quinidine product (Figure AII.4C). Although ^{1}H NMR shows corresponding quindine and mPEG peaks for the final product (Figure AII.6), there is again the issue of unconjugated glycine-quinidine in the sample. Therefore, this protocol also requires a better purification method. Dialysis may be an effective purification method for both protocols, however, it has to be done carefully since there are ester bonds that may hydrolyze.

AII. 4 Conclusions

Incorporation of quinidine as a moiety on a drug deliverying nanoparticle could be an effective method for P-gp substrate delivery. The first step in developing a drug delivery system with conjugated

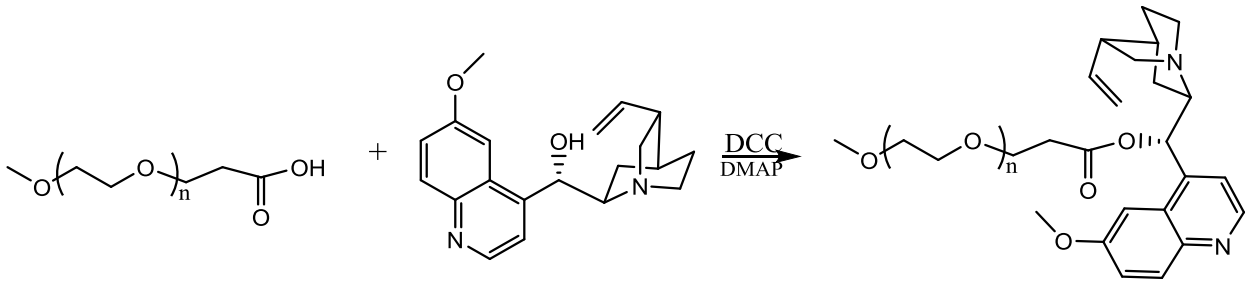

Figure AII.1 Reaction scheme for mPEG-quinidine conjugation. mPEG-COOH is reacted with quinidine at the secondary alcohol to produce an mPEG-quinidine conjugate.

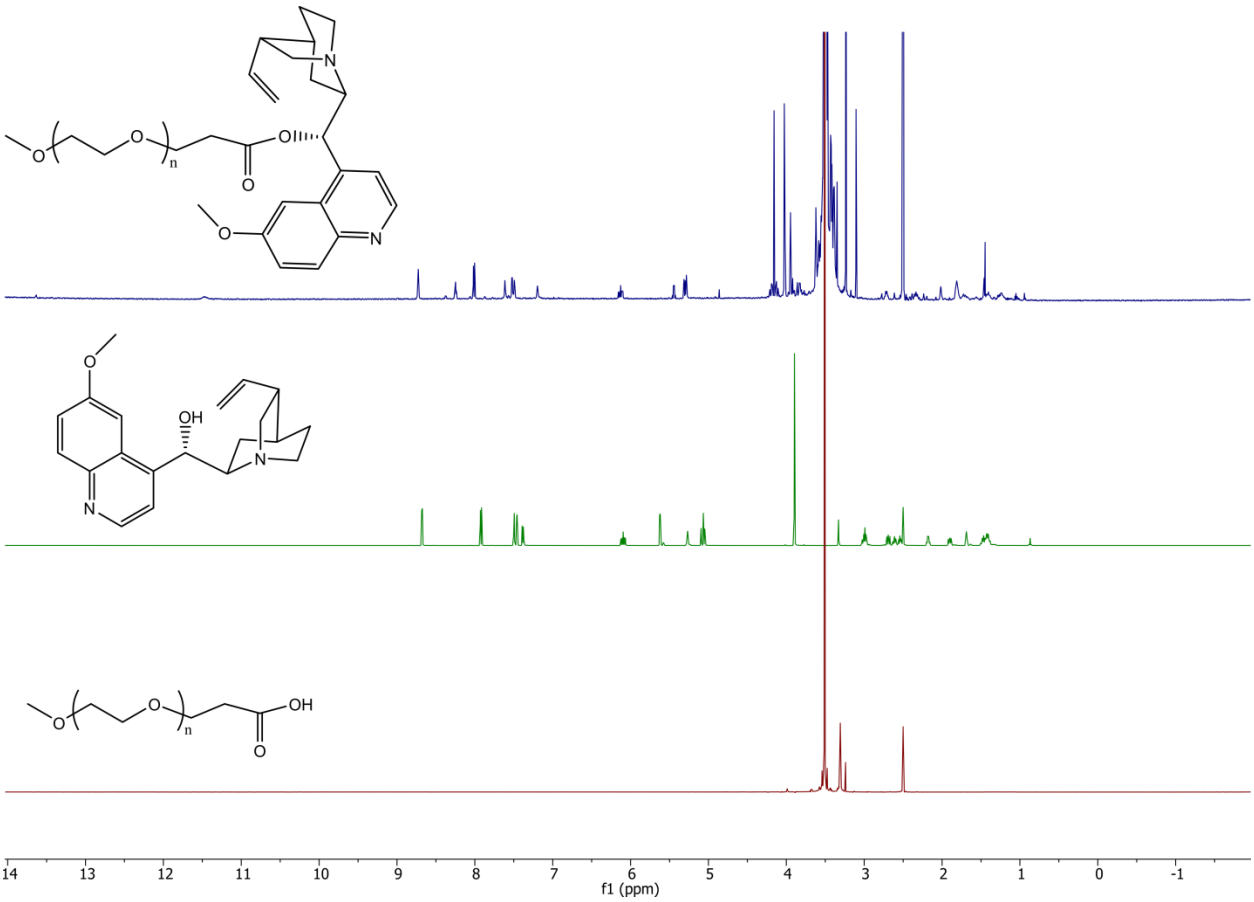

Figure AII.2. ^{1}H NMR of (bottom to top) mPEG-COOH, quinidine, and mPEG-quinidine.

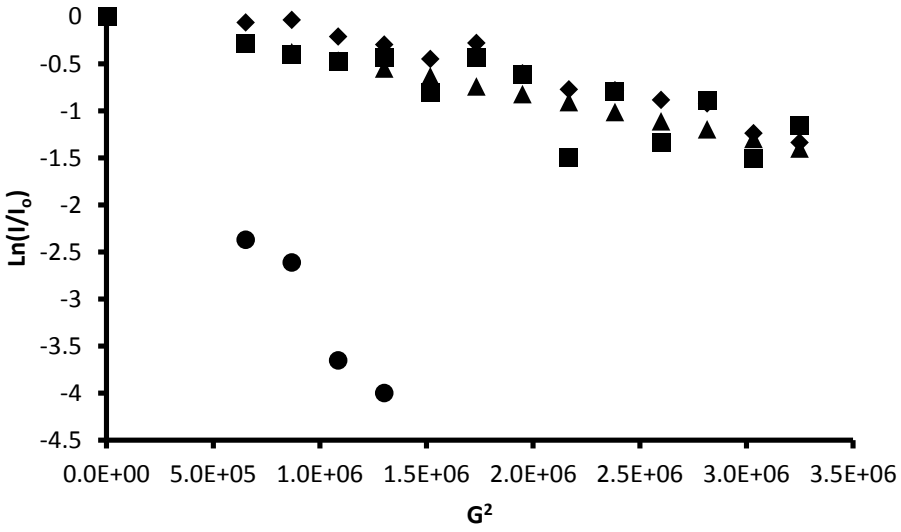

Figure AII.3. DOSY of mPEG-quinidine. DMSO (●), methoxy (mPEG) (◆), PEG (▲), quinidine aromatic region (■).

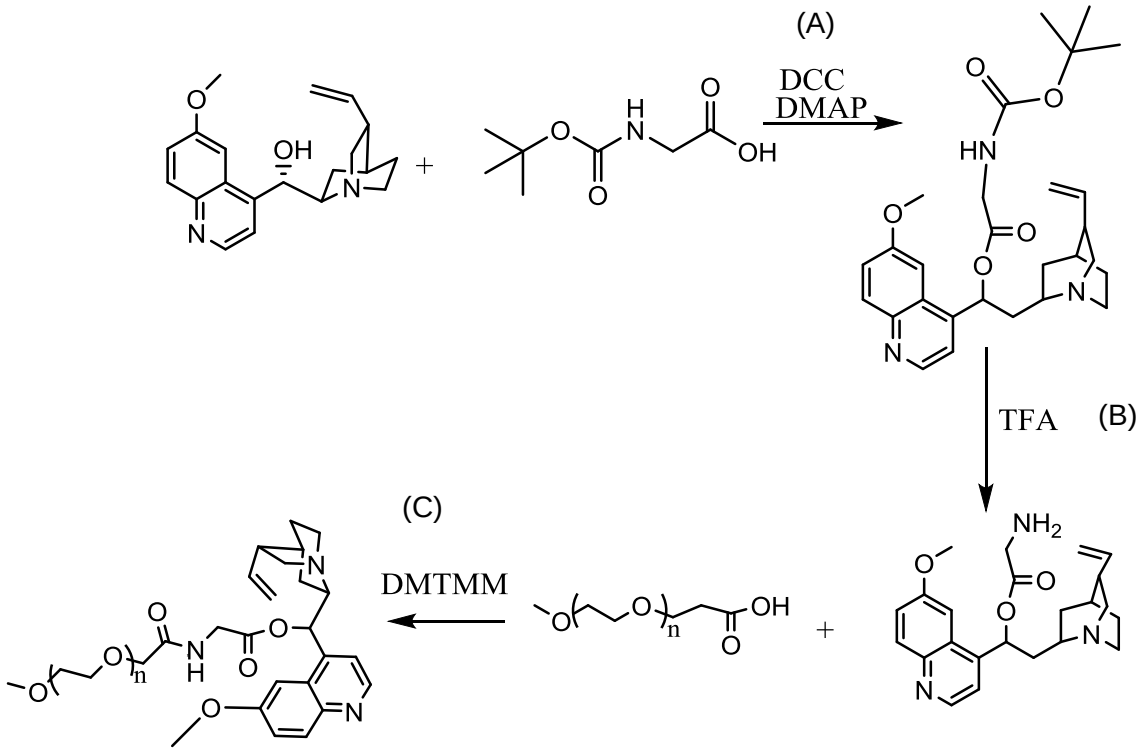

Figure AII. 4. Reaction scheme for glycine-quindine reaction. (A) formation of boc-glycine-quinidine from boc-glycine-OH and quinidine. (B) formation of glycine-quindine from deprotection of boc-glycine-quindine. (C) mPEG-glycine-quindine conjugation.

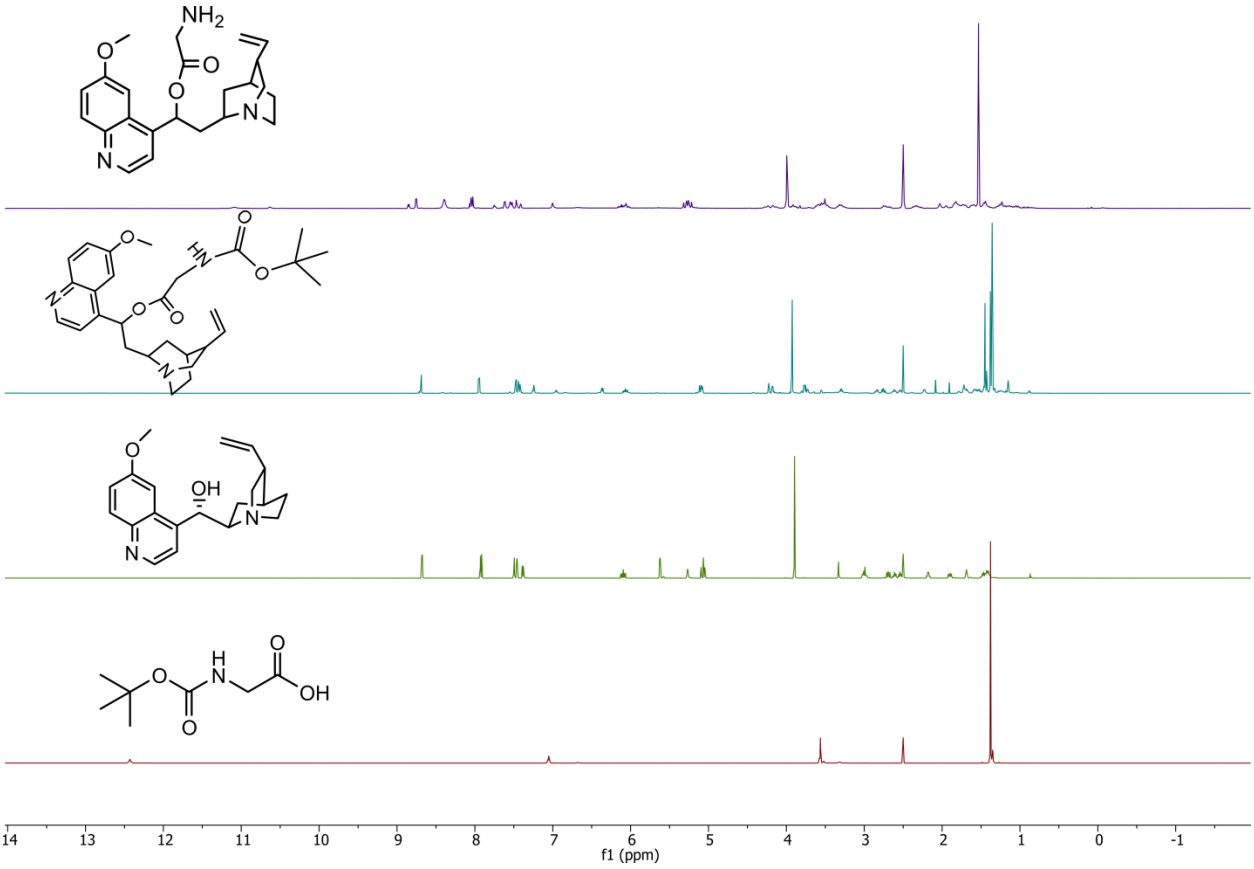

Figure AII.5. ^{1}H NMR of (bottom to top) boc-glycine-OH, quinidine, boc-glycine-quinidine, deprotected glycine-quinidine.

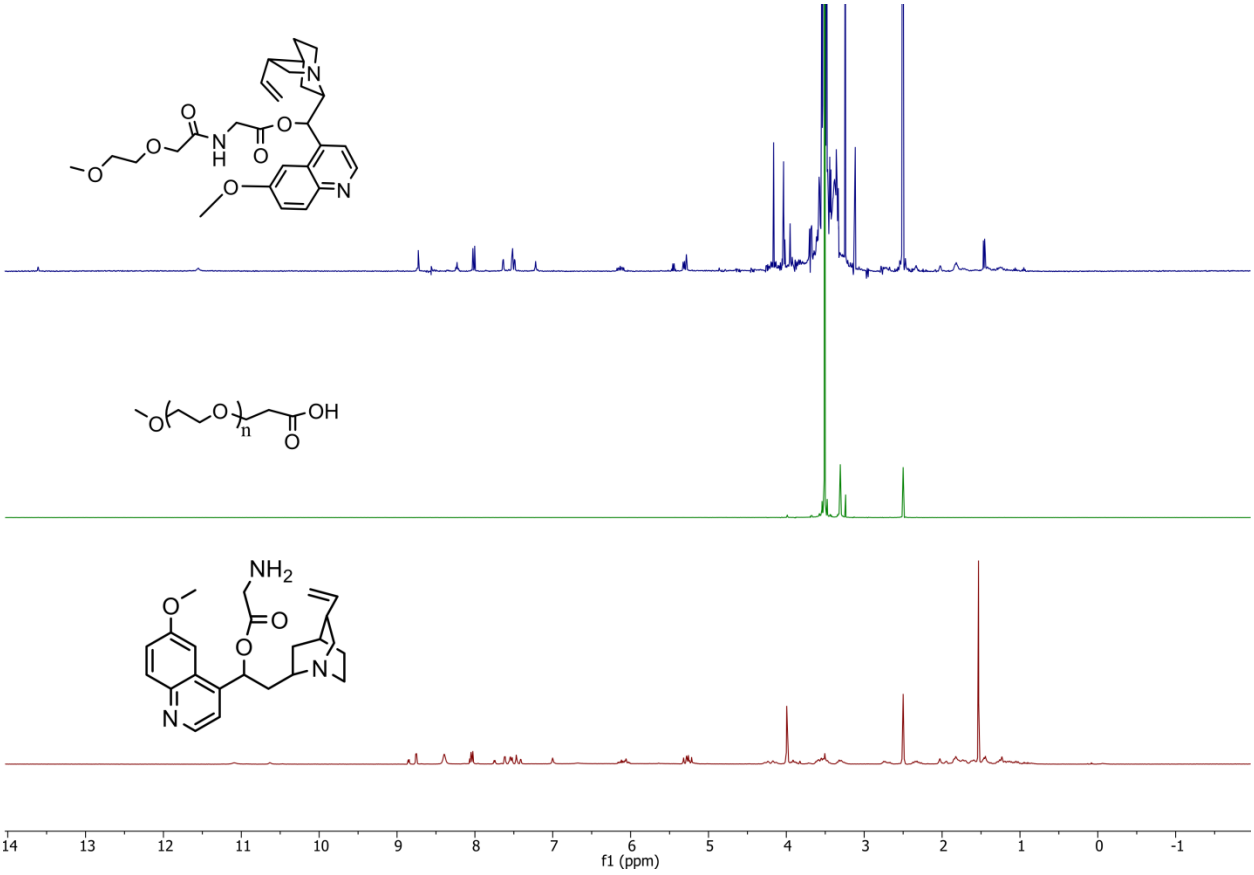

Figure AII.6. ^{1}H NMR of (bottom to top) glycine-quinidine, mPEG-COOH, mPEG-glycine-quinidine.

quinidine is to develop an mPEG-quinidine conjugate and assess its P-gp inhibition capabilities *in vitro*. The initial synthesis and characterization of such conjugates was described here. Both protocols seem to provide efficient conjugation, however better purification protocols are necessary. Once purified and re-characterized, these conjugates can then move forward toward *in vitro* screening and adaptation to a particle platform.

REFERENCES

(1) Ford, J. M. (1996) Experimental reversal of P-glycoprotein-mediated multidrug resistance by pharmacological chemosensitisers. *Eur. J. Cancer 32A*, 991–1001.

(2) Thomas, H., and Coley, H. M. (2003) Overcoming multidrug resistance in cancer: an update on the clinical strategy of inhibiting p-glycoprotein. *Cancer Control 10*, 159–165.

(3) Ghetie, M.-A., Marches, R., Kufert, S., and Vitetta, E. S. (2004) An anti-CD19 antibody inhibits the interaction between P-glycoprotein (P-gp) and CD19, causes P-gp to translocate out of lipid rafts, and chemosensitizes a multidrug-resistant (MDR) lymphoma cell line. *Blood 104*, 178–183.

(4) Tsuji, A., Tamai, I., Sakata, A., Tenda, Y., and Terasaki, T. (1993) Restricted transport of cyclosporin A across the blood-brain barrier by a multidrug transporter, P-glycoprotein. *Biochem. Pharmacol. 46*, 1096–1099.

(5) Efferth, T., and Volm, M. (1992) Antibody-Directed Therapy of Multidrug-resistant Tumor Cells. *Med. Oncol. Tumor Pharacotherapy 9*, 11–19.

(6) Murren, J. R., Durivage, H. J., Buzaid, a C., Reiss, M., Flynn, S. D., Carter, D., and Hait, W. N. (1996) Trifluoperazine as a modulator of multidrug resistance in refractory breast cancer. *Cancer Chemother. Pharmacol. 38*, 65–70.

(7) Szakács, G., Paterson, J. K., Ludwig, J. a, Booth-Genthe, C., and Gottesman, M. M. (2006) Targeting multidrug resistance in cancer. *Nat. Rev. 5*, 219–234.

(8) Yang, H., and Lopina, S. T. (2007) Stealth dendrimers for antiarrhythmic quinidine delivery. *J. Mater. Sci. Mater. Med. 18*, 2061–5.

(9) Zalipsky, S., Gilon, C., and Zilkha, a. (1983) Attachment of drugs to polyethylene glycols. *Eur. Polym. J. 19*, 1177–1183.